Structural Incorporation of Selenium into Pyrite and Mackinawite

Zur Erlangung des akademischen Grades eines

Doktors der Naturwissenschaften

von der Fakultät für

Bauingenieur-, Geo- und Umweltwissenschaften

des Karlsruher Instituts für Technologie (KIT)

genehmigte Dissertation

von

Alexander Diener

Hauptreferent: Prof. Dr. Thomas Neumann
Korreferent: PD. Dr. Thorsten Stumpf
Tag der mündlichen Prüfung: 06.06.2012

Erklärung über die Erstellung der Dissertation

Hiermit erkläre ich, dass ich die vorliegende Dissertation selbstständig verfasst, keine anderen als die angegebenen Quellen und Hilfsmittel benutzt, alle wörtlichen und sinngemäßen Entlehnungen deutlich als solche gekennzeichnet und die Grundsätze des Karlsruher Instituts für Technologie (ehemals Universität Karlsruhe TH) zur Sicherung guter wissenschaftlicher Praxis in ihrer aktuell gültigen Fassung beachtet habe.

Karlsruhe im April 2012

Für Ina

Abstract

Since many decades, selenium is of high environmental concern due to several reasons. It is an essential trace element for all vertebrates, but continuously under- and overdosage leads to diseases. Another topic is related to the disposal of high-level nuclear waste into deep geological formations. The radionuclide ^{79}Se could enter the biosphere, if such a disposal site comes into contact with groundwater and ^{79}Se starts to migrate upwards. These repositories consist of three different barriers: steel containers inclosing the vitrified radioactive material, the backfill material for closing the pits and the host rock itself. The safety of these disposal sites should function for a certain geologic lifetime of one million years. Therefore, it is necessary to assess the migration behavior of long lived radionuclides under consideration of the interaction between the dissolved contaminants and the host rocks for defined hydrochemical conditions. According to performance assessment reports for high-level radioactive waste repositories, ^{79}Se could be a threat if it is released from such a waste disposal site into the biosphere. Selenium is often associated with sulfides such as pyrite (FeS_2), the quantitatively most important iron sulfide mineral of the Earth´s crust, known for its capability to incorporate trace elements in a comparatively high amount. Pyrite is constituent of host rocks and bentonite backfills considered for radioactive waste disposal. Between 0.4 and 1.9 wt.% of pyrite are contained in Callovo-Oxfordian clay (CO; France), 1.1 ± 0.5 wt.% in Opalinus clay (OPA; Switzerland), 1 – 5 wt.% in Boom clay (BC; Belgium). Mackinawite (FeS) is usually the first precipitating iron sulfide under anoxic and low

temperature aqueous conditions due to kinetic reasons. Therefore, knowledge of the geochemical behavior of selenium during its transport in aqueous solutions while interacting with precipitating iron sulfides is a fundamental part to assess the safety of repository sites.

This study aimed at investigating the incorporation of Se^{2-} and Se^{4+} into pyrite and mackinawite, to determine the relevance of iron sulfides for the selenium retention, the homogeneity of selenium incorporation and the type of structural bonding. Feasible types of bonding are the formation of a FeS_xSe_y compound as solid solution phase, or as elemental selenium, achavalite (FeSe) or ferroselite ($FeSe_2$). The syntheses of pyrite and mackinawite occurred under standard conditions via direct precipitation in batch experiments and also as produced coatings on grounded natural pyrite simulating pyrite crystal growth in mixed-flow reactor experiments (MFR) under anoxic conditions at aqueous Se concentrations of 10^{-3} – 10^{-6} mol/L, a range of pH from 3.5 – 7 and an Eh from -200 – 100 mV. For the high temperature synthesis between 600° and 700° C, the incorporation of Se into single crystal pyrite was examined, using solid $AlBr_3$, Fe^0, S^0 and Se^0 by means of the chemical vapor transport (CVT) reaction in a 2-zone furnace.

Results from X-ray diffraction (XRD) and scanning electron microscopy (SEM) analyses reveal the formation of pure synthesized mackinawite or pyrite, the latter with a Se to S-ratio of 1:4 in batch experiments. The average Se^{2-} uptake into pyrite in batch experiments amounts to 98.6%. In MFR syntheses, it reaches 99.5%, suggesting a high potential for selenium retention. The focused ion beam coupled with energy dispersive X-ray analysis shows an inhomogeneous Se distribution with a higher accumulation in the center of the pyrite grains, probably due to the progressive depletion of Se from solution with regard to S. The high-temperature synthesis by chemical vapor transport enabled the homogenous incorporation of 1.1 wt.% Se in pyrite for single-crystals with a size up to 0.5 cm in diameter.

X-ray absorption fine-structure spectroscopy (XAFS) results indicate a substitution of sulfur by selenide only during instantaneous precipitation in highly supersaturated solutions accompanied with instantaneous precipitation. In Se doted mackinawite with Se^{2-} initially present in the solution, S^{2-} was substituted by Se^{2-}, resulting in a mackinawite-type

compound. S^- is substituted by Se^- in Se doted pyrite using initially dissolved Se^{2-}, yielding a FeS_xSe_y compound, comparable to a slightly distorted pyrite structure. Under less supersaturated conditions which have been performed in crystal growth experiments, XAFS results show a coprecipitation of initial Se^{2-} or Se^{4+} predominantly as Se^0 by changing the valence state. XAFS investigations of Se doped pyrite samples via condensation from gaseous phase with CVT reveal the incorporation mainly as Se^0 into the pyrite structure without further lattice bonding. Created Pourbaix diagrams show that the hydrochemical conditions of pyrite formation interfere with Se^0 as thermodynamically most stable selenium phase under these conditions.

This study demonstrates that pyrite and its most important precursor phase mackinawite, are efficient in removing selenium from aqueous solution, and therefore may contribute to reduce the mobility of ^{79}Se released from radioactive waste. The results imply that a lattice substitution of sulfide by selenide in iron sulfides probable only occurs in highly supersaturated solutions with an instantaneous precipitation under acidic and anoxic conditions. Under near-equilibrium hydrochemical conditions, Se^0 is expected to be the most stable species. Though the results suggest that the formation of a FeS_xSe_y compound, accompanied with a substitution of sulfur by selenium, plays a minor role in the retention of Se, the results are promising because elemental selenium is highly insoluble and therefore less bioavailable.

Zusammenfassung

Selen ist seit etwa einem halben Jahrhundert Gegenstand intensiver wissenschaftlicher Untersuchungen, da es aus mehreren Gründen eine hohe ökotoxikologische Bedeutung hat: Zum einen ist Selen für den Menschen, aber auch für alle übrigen Wirbeltiere, ein essentielles Spurenelement mit einer geringen Spannbreite von notwendiger täglicher Aufnahme und gesundheitsschädigender Dosis. Sowohl die kontinuierliche Unter- als auch Überversorgung von Selen verursacht physiologische Schäden, die zum Tod führen können. Weiterhin ist Selen auch aufgrund seines radioaktiven Isotops ^{79}Se hinsichtlich der Verklappung von hochradioaktiv strahlenden Abfällen in tiefen geologischen Formationen von hoher Relevanz.

Ein Endlager besteht aus drei verschiedenen Barrieren, die eine Migration der Schadstoffe in die Biosphäre über einen Zeitraum von einer Million Jahre verhindern sollen, falls es in diesem Zeitraum in Kontakt mit Grundwasser kommen sollte. Für diesen Fall muss vorab das Migrationsverhalten von Radionukliden über eine derart lange geologische Zeitdauer bewertet werden. Hierfür müssen die Wechselwirkungen zwischen gelöster, toxischer Phase und dem jeweiligen Barrierematerial untersucht werden, angefangen vom Nahfeld des Endlagers bis hin zu den Mineralen des Wirtsgesteins. Berechnungen zur Bewertung der Langzeitsicherheit von einigen potentiellen Endlagern für radioaktive Abfälle zeigen für ^{79}Se, dass es die gesamte Exposition von Radionukliden aus Endlagern in die Biosphäre für einen Zeitraum von 10^4 bis 10^6 Jahren nach der Einlagerung der Abfälle dominiert.

Selen weist generell ein komplexes hydrochemisches Verhalten auf. Unter stark reduzierenden Bedingungen ist Selenid (Se^{2-}) dominierend, von mäßig reduzierten bis zu redoxneutralen Bedingungen wiederum metallisches Selen (Se^{0}). Diese beiden Speziationen sind als mineralische Phasen schwer löslich. Unter oxidierenden Bedingungen bis ~200 mV dominieren die leichter löslichen Valenzen Selenit (Se^{4+}) und Selenat (Se^{6+}), wobei das letztere unter stark oxidierenden Bedingungen vorherrscht.

Hohe Konzentrationen von Selen in Mineralen konnten bisher unter anderem für verschiedene Sulfide festgestellt werden. Das Eisensulfid mit der höchsten Verbreitung in der Erdkruste ist Pyrit (FeS_2). Pyrit ist das thermodynamisch stabile Endprodukt der Eisensulfide unter den anoxischen, hydrochemischen Verhältnissen in marinen Sedimenten und hydrothermalen Prozessen. Weiterhin ist auch bekannt, dass Pyrit viele Spurenelemente bis zu Konzentrationen von einigen Mol-% in seine Struktur einbaut. Ebenso ist Pyrit mit einigen Gew.% Bestandteil in mehreren geologischen Formationen, die für die HLW-Endlagerung in Betracht gezogen werden: 0,4 – 1,9 Gew.% in Callovo-Oxfordian (Frankreich), 1,1 ± 0,5 Gew.% in Opalinus (Schweiz), 1 – 5 Gew.% in der Boom Clay Formation (Belgien). Der metastabile Mackinawit (FeS) ist hinsichtlich des Se-Einbaus von Relevanz, da es unter anoxischen Bedingungen bei Temperaturen unter 100°C aus kinetischen Gründen in der Regel als erstes Eisensulfid ausfällt. Die bis dato veröffentlichten Untersuchungen über die Sorption von Selen an Pyrit zeigten eindrucksvoll, dass Pyrit für die Se-Fixierung (>95% Sorption von Se^{2-} und Se^{4+} unter sauren pH Bedingungen) eine wichtige Mineralphase darstellt. Der strukturelle Einbau von Selen in Pyrit wurde bisher in wenigen natürlichen Mineralproben untersucht. Die Ergebnisse sind nicht eindeutig, da zum einen Pyrit-Dzharkenit Mischmineralphasen (Dzharkenit ist ein seltener $FeSe_2$ Polymorph mit kubischer Kristallstruktur) mittels Röntgenabsorptionsanalyse (XAFS) detektiert wurden, andererseits aber sequentielle Extraktionen zeigten, dass nur ein sehr geringer Anteil von in Pyrit fixiertem Selen strukturell gebunden ist. Laborversuche zur synthetischen Herstellung von Selen dotierten Pyriten erfolgten bisher nicht.

Die hier dargestellten Untersuchungen beschäftigen sich mit der Fixierung von Selen in Pyrit und Mackinawit. Als relevante Valenzen wurden Se^{2-} und Se^{4+} ausgewählt, da diese neben dem beinahe unlöslichen Se^0 als einzige im Stabilitätsfeld von präzipitiertem Pyrit liegen. Der Fokus in dieser Studie liegt zum einen auf der Betrachtung der quantitativen Menge des Seleneinbaus als Feststoff-Lösungsphase und auf der Homogenität der Verteilung des eingebauten Selens in den Eisensulfidphasen. Weiterhin ist von Interesse, ob Selen in die Mackinawit- oder Pyritstruktur als FeS_xSe_y-Mischmineral mitsamt Substitution von S durch Se eingebaut wird oder ohne strukturelle Bindung, bsp. als Achavalit (FeSe), Ferroselit ($FeSe_2$) oder als elementares Selen. Durch die definierten, primär anoxischen hydrochemischen Bedingungen sollten die Verhältnisse in einem Endlager für radioaktive Abfälle nachempfunden werden.

Für die Herstellung von Selen dotierten Eisensulfiden wurden drei unterschiedliche Verfahren ausgewählt. Zum einen wurden in einer Handschuhbox unter Argon-Atmosphäre Selen dotierte Pyrite und Mackinawite in Batchverfahren innerhalb von 5 Tagen synthetisiert. Diese Eisensulfide wurden bei konstanten Bedingungen aus Lösungen mit Se-Konzentrationen zwischen $10^{-3} – 10^{-6}$ Mol/l bei pH-Bedingungen zwischen 3,5 – 7 und Eh-Bedingungen von -200 – 100 mV gefällt. Weiterhin wurde in einem Durchflussreaktor (MFR) der Grundwasserfluss für einen Zeitraum von jeweils 5 Tagen simuliert. Hierbei wurden die in drei separierten Behältern befindlichen Eisen-, Schwefel- und Selenlösungen bei gleich bleibender Geschwindigkeit in den MFR gepumpt. Im Reaktor lagen bereits gemahlene, natürliche Pyrite mit sehr geringen Se-Konzentrationen vor, die als Nuklei für weiteres Pyritwachstum auf deren Oberflächen eingesetzt wurden. Über einen mittig installierten Magnetschwimmer im MFR wurden sowohl Lösung als auch Nuklei miteinander kontinuierlich vermischt. Als letztes Syntheseverfahren wurde mittels chemischen Dampftransports in einem 2-Zonenofen unter Anwendung eines Temperaturgradienten von 700° – 600° C, Selen dotierter Pyrit erzeugt. Die I ngredienzen $AlBr_3$ (als Trägersubstanz für Eisen), Fe^0, S^0 und Se^0 gehen dabei in die Dampfphase über und kondensieren auf der kühleren Seite wieder als Selen dotierter Pyrit. Mittels Röntgendiffraktometrie (XRD) und

Rasterelektronenmikroskopie (SEM) wurden die präzipitierten Mineralphasen und Kornformen untersucht. Der Se-Gehalt aus der abgefilterten Lösung wurde mit ICP-MS bestimmt, der Se-Gehalt innerhalb des eingebauten Pyrits wurde mittels energiedispersiver Röntgenfluoreszenz (ED-XRF) gemessen, dessen Verteilung innerhalb des Pyrits über die energiedispersive Röntgenanalytik (EDX) des fokussierten Ionenstrahls (FIB) bestimmt. Die Se-Bindungsformen wurden mittels Röntgen-Photoelektronenspektroskopie (XPS), der Röntgen-Nahkanten-Absorptionsspektroskopie (XANES) und der Röntgenabsorptions-Feinstrukturanalyse (EXAFS) ermittelt.

Die Ergebnisse der XRD und SEM-Analyse ergaben, dass in den Batchexperimenten eine Synthese von reinem Se-dotiertem Mackinawit sowie Se-dotiertem Pyrit mit spheroidaler Morphologie erfolgte. Bei letzterem konnten reine Se-dotierte Pyritphasen erst nach der Verringerung des gelösten Eisens von einem Fe/S-Verhältnis von 1:2 zu 1:4 erzielt werden. Der Korndurchmesser des ausgefällten Pyrits betrug 1-2 µm, bei Se-Gehalten bis zu 2 Gew.%. Die EDX-Analyse des FIB zeigte, dass das Selen im Zentrum des Pyrits stärker konzentriert war und die Gehalte zum Rand hin zunehmend abnahmen. Der Grund dafür liegt wahrscheinlich in der zunehmenden Verarmung des Selens im Verhältnis zum Schwefel innerhalb der Lösung während der Pyritsynthese, da sich bei der Mischung der Se-, S-, Fe-Lösungen direkt S^0 bildet, der sich mit zunehmender Zeitdauer des Experiments partiell auflöst und somit gelösten Schwefel nachliefert. Die mit ICP-MS ermittelten Se-Gehalte in den dekantierten Lösungen zeigen, dass 98% des ursprünglichen Selens in Pyrit eingebaut und somit aus der Lösung entfernt wurden. In den MFR-Experimenten wurden sogar 99,5% des Selens in Pyrit eingebaut. In der Hochtemperatursynthese von Se-dotiertem Pyrit mittels CVT konnte 1,1 Gew.% Selen in Pyrit-Einkristallen mit einer Größe bis zu 0,5 cm eingebaut werden.

Die XPS-Messungen an den Se-dotierten Eisensulfiden weisen auf einen reduzierten Valenzzustand (Se(-II,-I,0)) des eingebauten Selens hin. Die XAFS-Analysen zeigen, dass eine Substitution von S durch Se nur in den Batchversuchen bei hoch übersättigten Lösungen (SI: 11-13) erfolgte, da unter diesen Bedingungen eine direkte Ausfällung des

metastabilen Mackinawits erfolgte, der durch Auflösung und Wiederausfällung in Selen dotierten Pyrit transformiert wurde. Im Selenid-dotierten Mackinawit der Batchversuche wurde S^{2-} durch Se^{2-} substituiert, woraus eine Kristallstruktur resultiert, die der des Mackinawits ähnelt. In Selenid-dotiertem Pyrit wurde S^{-} durch Se^{-} substituiert, was wiederum zu einer FeS_xSe_y Verbindung geführt hat, die sich als geringfügig gestörte Pyritstruktur bezeichnen lässt. Für die Versuche mit weniger gesättigten Lösungen in den MFR-Experimenten zeigen die XAFS-Messungen, dass Se^{2-} und Se^{4+} hauptsächlich als Se^{0} im Pyrit eingebaut wurden. Das gleiche gilt für die CVT-Experimente, bei denen ebenso Se^{0} in Pyrit ohne weitere Bindung als Kristalldefekt eingebaut wurde. Die MFR- und CVT-Ergebnisse stimmen mit erstellten Stabilitätsdiagrammen überein. Diese zeigen, dass unter den hydrochemischen Bedingungen für die Pyritausfällung das elementare Selen die thermodynamisch stabilste Selenphase darstellt.

Diese Studie zeigt, wie unter kontrollierten Bedingungen der Einbau von Se in Pyrit und Mackinawit erfolgreich durchgeführt und mittels XAFS strukturell nachgewiesen werden kann. Generell verfügen Pyrit und Mackinawit über eine große Aufnahmekapazität für Selenid und Selenit, was letztlich zu einer Verringerung der Mobilität von ^{79}Se aus einem radioaktiven Endlager in die Biosphäre beitragen kann. Letztlich ist aber elementares Selen unter den hydrochemischen Bedingungen der Pyritbildung die thermodynamisch stabilste Se-Valenz. Auch wenn ein struktureller Einbau von Selen in Pyrit und Mackinawit unter anoxischen und sauren Bedingungen eher unwahrscheinlich ist, so sind die Ergebnisse trotzdem vielversprechend, da Se^{0} sehr unlöslich ist und die Se-Mobilität erheblich reduzieren würde. Der spektroskopische Nachweis mit XAFS stellt hinsichtlich der Speziation und dem Einbau von Radionukliden in stabile Mineralphasen eine Schlüsselanalytik für den Nachweis der Langzeitsicherheit von Untertagedeponien dar.

Outline

List of Figures

List of Tables

Chapter 1

Introduction

Selenium is a critical element because it is as micronutrient essential to humans and animals, it accumulates in the food-chain and the range between toxic dosage and necessary uptake is narrow (Ch. 2.1.2; Schrauzer, 2004). In addition, the ^{79}Se isotope is a long-lived fission product of ^{235}U and ^{239}Pu which is chemically and radiologically toxic (Ch. 2.1.3; Jörg et al., 2010). The deep geological storage of high-level nuclear waste in a multi-barrier system is considered to be the safest concept, but this has to be ensured over a geological time span of one million years. Radionuclides could possibly migrate from such a repository into the biosphere, if a disposal site gets into contact with groundwater. Geochemical processes like the coprecipitation of a contaminant with a mineral can lead to its retention in an aquifer system (Grambow, 2008). In this regard, the structural incorporation of trace elements into host minerals is a common and effective decontamination process in natural systems, but it has not yet been studied for the iron-sulfur-selenium system (Ch. 2.3). The synopsis of spectroscopy, geochemical modeling and batch experiments with purified minerals increases the understanding of the whole process. Séby et al. (1998) and Grambow (2008) describe the actual lack of knowledge with regard to selenium as follows:

Séby: "The general behaviour of this element being rather complex, it seems essential to identify the predominating equilibria of the different Se species and the influence of parameters such as pH, redox potential, microbial activity and the presence of complexing and precipitating agents on its release during a long period."

Grambow: "In conclusion, we do not yet have a fully verified model for Se solubility in repository systems which would cover repository conditions from the very reducing iron rich conditions close to the waste to the less reducing conditions in the host rock at some larger distance."

In this respect, pyrite is a relevant part of many host rocks which are considered as high-level waste (HLW) repositories and it is a common point of view that pyrite plays a major role in the fixation of selenium (Ch. 2.2.2 - 2.2.4). The study on hand tries to enlarge the knowledge of selenium behavior in the Fe-S-Se system mainly under reducing conditions by using advanced spectroscopic techniques to determine the supposedly high affinity of selenium to iron sulfides and the type of structural bonding (Ch. 5). As well, these spectroscopic results will be compared with thermodynamic results, modeling the behavior of dissolved Fe-S-Se species under defined hydrochemical conditions (Ch. 2.3; 5.1).

The task was to synthesize selenide (Se^{2-}) and selenite (Se^{4+}) doted pyrite and mackinawite by different techniques (Ch. 4). The methods of choice were:

1.) Classical batch reactions under standard and anoxic conditions by mixing solutions and keeping the potential steady using an electrochemical cell. In this regard, highly supersaturated solutions allowed a simulation of nucleation with limited crystal growth by kinetically rapid formation of selenium doted pyrite in the µm-scale.
2.) Simulating pyrite crystal growth and groundwater flow under standard and anoxic conditions by continuously pumping of separate Se-, S- and Fe- solutions into a mixed flow reactor (MFR). Natural Se-poor grounded pyrites served as seeds for a

further crystal growth with coatings of selenium doted pyrite from slightly supersaturated solutions.

3.) The high-temperature synthesis by chemical vapor transport is a good option to simulate hydrothermal conditions of selenium doted pyrite precipitation. In comparison to the previous mentioned synthesis procedures, this method allowed a direct precipitation of Se doted pyrite through the gaseous phase by achieving larger single crystals in the mm-scale.

In all cases, commercially available selenium compounds were used as analog for testing the ^{79}Se chemical behavior. Both, Se^{2-} and Se^{4+} are proposed as most important valence states which contribute to the potential thread of ^{79}Se radionuclide under the hydrochemical conditions in a high-level waste (HLW) disposal site, commonly supposed as neutral to alkaline and anoxic (Ch. 2.1.3). Pyrite is by far the most widely-spread iron sulfide in the earth crust and mackinawite itself is, though thermodynamically unstable, usually the first precipitated iron sulfide phase under ambient conditions (Ch. 2.2.1; 2.3.4). Due to this common knowledge, these selenium valence states and iron sulfides were chosen for investigations of dissolved species-mineral reactions.

Questions to answer:

The incorporation of a contaminant into a mineral is, compared to other types like colloidal binding and inner- or outer-sphere sorption, presumably the most efficient process of removal because the remobilization can only take place through diffusion of the ion out of the mineral or by dissolution of the mineral. Objective of this study is to gain knowledge about the reactions taking place during the incorporation of Se^{2-} and Se^{4+} into pyrite and mackinawite for certain pH and Eh solution conditions:

- Is the final valence state of structurally fixed Se the same as the initial one? How is Se bound in mackinawite and pyrite? Is there a difference in Se speciation and

structural incorporation with regard to different hydrochemical conditions? Do the experimental results fit to the predicted stability fields which are calculated on the basis of thermodynamic data?

- What is the amount of incorporated selenium under consideration of the progressing time of experiments? Does the incorporation vary with regard to the two different minerals, the initial Se valence states or changes in the hydrochemical conditions?
- If incorporation should happen, how is Se distributed? Is it spatially homogeneous or does preferential incorporation occur with extraordinary differences in the selenium concentrations?

To answer these questions, a suite of powerful analytical techniques were applied: X-ray absorption fluorescence spectroscopy (XAFS) was used because it is an effective tool for investigations of the structural parameters, e.g. determination of the valence state of an element, type and distances of atomic neighbors and the related coordination number (Ch. 3.2).

To determine the initial and final Fe-, S- and Se-concentrations as well as the concentrations for certain time steps after starting an experiment, inductively coupled plasma - mass spectrometry (ICP-MS) and inductively coupled plasma - optical emission spectroscopy (ICP-OES) measurements were performed.

To reveal that only the desired monomineralic phase did precipitate from solution, either pyrite or mackinawite, investigations by x-ray diffraction (XRD) and scanning electron microscopy (SEM) were carried out. Hence, the distribution of selenium in iron sulfides was determined by energy dispersive x-ray systems (EDX), belonging to focused ion beam and scanning or transmission electron microscope (Ch. 3.1).

Chapter 2

Geochemistry of selenium and pyrite

The selenium as well as the pyrite system show a rather complex chemical behavior due to their high dependence on the hydrochemical conditions as well as on kinetics (Rickard and Luther, 2007; Lenz and Lens, 2009). The general perception of selenium changed remarkably during the past. In the early decades of the last century, selenium was identified solely as poison, threatening to health of humans and cattle. Nowadays, the role of selenium is more clearly identified as essential toxin, since it is also a necessary micronutrient for the vertebrates (Ch. 2.1; Lenz and Lens, 2009). In the last three decades, another aspect of high relevance regarding selenium was identified. Different performance assessment reports of high-level waste nuclear repositories evaluated a migration of the radionuclide ^{79}Se from the disposal site into the biosphere, if the repository should come into contact with groundwater (Ch. 2.1; Mallants et al., 2001).

The geochemistry of selenium is closely related to sulfides, because the chemical behavior of selenium is similar to sulfur (Howard, 1977). Pyrite as most important near-surface iron sulfide and part of the host rocks of considered HLW-repositories could play a major role in the fixation of selenium (Ch. 2.2). Since the chemical behavior of selenium in the Fe-S-Se

system is highly dependent on its valence state, the oxidation states of selenium and sulfur are figured out in Eh-pH diagrams as well as the reaction pathways of mackinawite and pyrite (Ch. 2.3).

2.1 Selenium in the environment

Selenium was first discovered in 1818 by the Swedish chemist Berzelius and is named after the Greek goddess of the moon, “Selene”. Its atomic number is 34 and the atomic mass amounts to 78.96 u. Elemental selenium has a melting point of 217°C and a boiling point of 685°C. Selenium belongs to the group of chalcogens , is located between sulfur and tellurium in the group VIA of the Periodic Table of the Elements, and has 6 stabile isotopes (the numbers in brackets show the global distribution): ^{74}Se (0.87%), ^{76}Se (9.02%), ^{77}Se (7.58%), ^{78}Se (23.52%), ^{80}Se (49.82%), ^{82}Se (9.19%); and 9 radioactive isotopes with half-lives <8 h, except ^{75}Se (120 d) and ^{79}Se (295000 – 377000 yrs.) (Schrauzer, 2004; Lenz and Lens, 2009).

There are no economically important selenium ore deposits; but selenium is produced as a by-product during electrolytic refining of copper, lead and silver, since e.g. copper anodes contain 0.5 – 280 g Se in 1 kg of copper (Schrauzer, 2004). The world production of selenium amounts to ~2000 t/a. Selenium is used by the glass industry (~25 % of the total sum in the year 1996), in inorganic pigments (~25 %) and due to its photoelectric and semiconducting properties of Se^0, it is often applied in electronics (~15 %). To counteract selenium deficiency in soils and human health, selenium is part of fertilizers as well as in dietary supplements (~20 %), amongst others for cancer prevention. Furthermore, Table 2.1 shows some common applications of different Se-compounds (Schrauzer, 2004; Lenz and Lens, 2009).

Tab. 2.1: Selenium compounds and their applications (Schrauzer, 2004).

Selenium	**Rectifiers, photoelectric cells, blasting caps; xerography, stainless steel; as dehydrogenation-catalyst**
Tellurium-selenium alloys	**Erasing optical stores**
Sodium selenite (Na_2SeO_4)	**Insecticide; glass manufacture; veterinary pharmaceuticals**
Selenium diethyldithiocarbamate	**Fungicide; vulcanizing agent**
Selenium monosulfide (SeS)	**Veterinary medicine; dandruff removal**
Selenium disulfide (SeS_2)	**Veterinary medicine; dandruff removal**
Selenium dioxide (SeO_2)	**Catalyst for oxidation, hydrogenation or dehydrogenation of organic compounds**
Selenium hexafluoride (SeF_6)	**Gaseous electric insulator**
Selenium oxychloride ($SeOCl_2$)	**Solvent for sulfur, selenium, tellurium, rubber, bakelite, gums, resins, glue asphalt among others**
Aluminium selenide (Al_2Se_3)	**Preparation of hydrogen selenide for semiconductors**
Ammonium selenite [$(NH_4)_2SeO_3$]	**Manufacture of red glass**
Cadmium selenide (CdSe)	**Photoconductors, photoelectric cells, rectifiers**
Cupric selenate ($CuSeO_4$)	**In coloring copper and copper alloys**
Tungsten diselenide (WSe_2)	**In lubricants**

2.1.1 Global distribution and cycling of selenium

Selenium is overall, but very heterogeneously distributed over the earth's surface with an average abundance of 0.05 – 0.09 mg/kg in crustal rocks. The patchy distribution of Se in soils on the global scale is highly variable and is primarily controlled by the geological background and its weathering, e.g. by Se-rich rocks like cretaceous shales (<1 – 300 mg/kg Se), phosphate rocks (1 – 178 mg/kg Se), volcanic rocks (up to 120 mg/kg), sandstones, uranium-rich deposits or magmatic sulfides, which show a Se/S ratio of approximately 1:10. Selenium is a major part of 22 selenides, 6 sulfosalts, 4 selenites, 1 oxide, 1 selenate and minor constituent of 22 sulfides and tellurides (Engberg et al., 1998; Schrauzer, 2004; Ryser et al., 2005; Lenz and Lens, 2009). Table 2.2 shows that the mean concentrations of selenium in the atmosphere as well as in aquatic environments are comparatively low to soils and rocks.

Tab. 2.2: Overview of Se concentrations in the environment (Schrauzer, 2004).

Origin	Average Conc.	Range
Atmosphere		
Urban	3 ng/m^3	0.01-30 ng/m^3
Rural	1.3 ng/m^3	0.01-3 ng/m^3
Lithosphere		
Agricultural soils	0.4 mg/kg	0.02-2 mg/kg
Hydrosphere		
Freshwater	0.2 µg/L	0.02-450 µg/L
Ocean	0.2 µg/L	
Biosphere		
Primary accumulator	1000 mg/kg	100-5000 mg/kg
Second. accumulator	100 mg/kg	10-500 mg/kg
Food crops	0.1 mg/kg	<0.05-1 mg/kg
Mankind		
Tissue	0.1 mg/kg	<0.05-5 mg/kg
Blood	0.07-0.25 mg/L	0.05-1 mg/L

The global natural emission of Se compounds into the atmosphere is estimated as 6000 – 13000 t/a, with 60% – 80% of marine biogenic origin. The selenium concentrations in ground and surface waters is predominantly low with <10 µg/L, but can be sometimes enlarged in areas with seleniferous soils (>0.5 mg/kg). In the biosphere, selenium concentrations can be extraordinarily high in primary accumulators, which are generally non-food plants. They can incorporate up to 5 Se g/kg dry weight by incorporation into cellular proteins (Schrauzer, 2004).

Anthropogenic activities have deeply influenced the global selenium cycle, e.g. releasing selenium into the environment due to Se-rich coal (up to >1000 mg/kg Se) and oil combustion, mining activities, utilization of Se-agricultural products as fertilizer, non-ferrous metal melting, wastewater discharge of oil refineries or irrigation drainage into lakes or wetlands with continuing Se-accumulation. The rough estimation of the total anthropogenic Se-emission into environment is between 3000 and 9600 t/a, with 40% being of volatile and 60% of particulate emission. The most relevant processes and reservoirs contributing to the

selenium cycle are shown in Figure 2.1 (Mayland et al., 1989; Engberg et al., 1998; Terry and Zayed, 1998; Schrauzer, 2004; Ryser et al., 2005; Lenz and Lens, 2009).

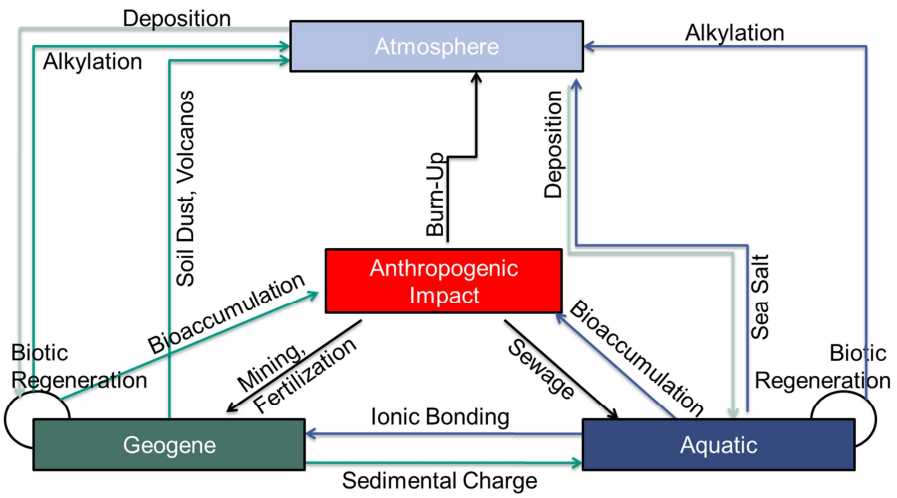

Fig. 2.1: Schematic overview of the reservoirs and most important environmental processes within the global cycle of selenium (modified after Lenz and Lens, 2009).

The potential threat could rise, if the increasing energy demand is covered by fossil fuel combustion. The estimated selenium emissions to the atmosphere due to anthropogenic activities amount to 37.5 – 40.6 % of the total emission. Atmospheric selenium transport is associated with particulate matter (Schrauzer, 2004; Lenz and Lens, 2009).

2.1.2 Health effects due to selenium toxicity

In the past decades, comprehensive studies about selenium in the environment have been performed, since it is both a trace nutrient and a toxin (Shaw and Ashworth, 2010). In its role as essential trace element selenium is of high concern for humans as well as for all vertebrates worldwide for which the range between deficiency and toxic dose is narrow (Mayland et al., 1989). The desirable range of daily Se-uptake for children is 1.7 µg/kg and for adults 0.9 µg/kg body weight. With regard to daily dietary intake, by far the most denotative contribution of selenium for humans is foodstuff, especially in high-selenium areas. Most drinking-water contains much less than the health based WHO-guideline value

for drinking water of 40 µg/L (WHO, 2011), while the average global intake of selenium from food amounts to 70 µg/d, with a range of 10 – 350 µg/d. Daily intake of selenium due to inhalation from the atmosphere in urban environments is usually negligible with 0.07 µg/d and a range of 0.0002 – 0.7 µg/d (Schrauzer, 2004). In the body, inorganic selenium is largely transformed into selenoproteins which are essential as antioxidants for humans. They protect e.g. against cancer and heart disease, although there is a lot of discussion among scientists with regard to the actual human-health benefits of e.g. due to supplementary intake. The predominant form of selenium supplementation is selenomethione, one of 30 already detected selenoproteins (Lacour et al., 2004; Tinggi, 2008).

For animals, the necessary daily selenium intake is higher than 0.05 – 0.1 mg/kg (Mayland et al., 1989). One problem in this context is that selenium is known to accumulate in living organisms along the food chain predominantly as Se^{4+} and Se^{6+} in the food chain, which have the highest bioavailability. Therefore, it is possible that toxic levels are achieved within the food chain, causing various diseases in humans and livestock (Hamilton, 2004; Wu, 2004; Agüero et al., 2008; Navarro-Alarcon and Cabrera-Vique, 2008).

Since the past century, deficiency related diseases of selenium uptake known. The multi-pathogeny Keshan disease is a heart enlargement affecting especially children, often leading to death, while multi-pathogeny Kashin-Beck disease is apparent in deformity of extremities. Furthermore, animals with Se-deficiency suffer from potentially mortal white muscle disease or skeletal degeneration. Especially the mortality rates of lamps, calves, pigs and poultry as most endangered species can reach up to 60% (Kishchak, 1998). Cases of acute selenosis were published, resulting in hair and nail loss in most cases, disorder of the nervous system, skin lesions and decayed teeth (Li et al., 2011). The common selenosis in cattle results in teratogenesis, dystrophic growth of the hoof and hair loss. In birds, the indications are emaciation, teratogenesis, nail necrosis or toxic lesions (O´Toole and Raisbeck, 1998). The most severe cases of deficiency and toxicity related diseases occurred in areas where human population and farm animals highly depended on food supply from local Se-poor or –enriched crops (Li et al., 2011).

2.1.3 The ^{79}Se isotope in high-level waste disposal sites

The ^{79}Se radioisotope is generated from the decay of ^{235}U and ^{239}Pu mainly by nuclear fission of these radionuclides which originate mostly from the reactor core of nuclear power plants. The fission yield of formation accounts to 0.0487% for uranium and 0.05504% for plutonium, as result from the cumulated fission yields of the respective masses. The isotopes ^{77}Se, ^{78}Se, ^{79}Se, ^{80}Se and ^{82}Se occur naturally as well as stable end points of isobaric fission beta decay chains which differ with regard to their isotopic composition (Fig. 2.2; Jörg et al., 2010).

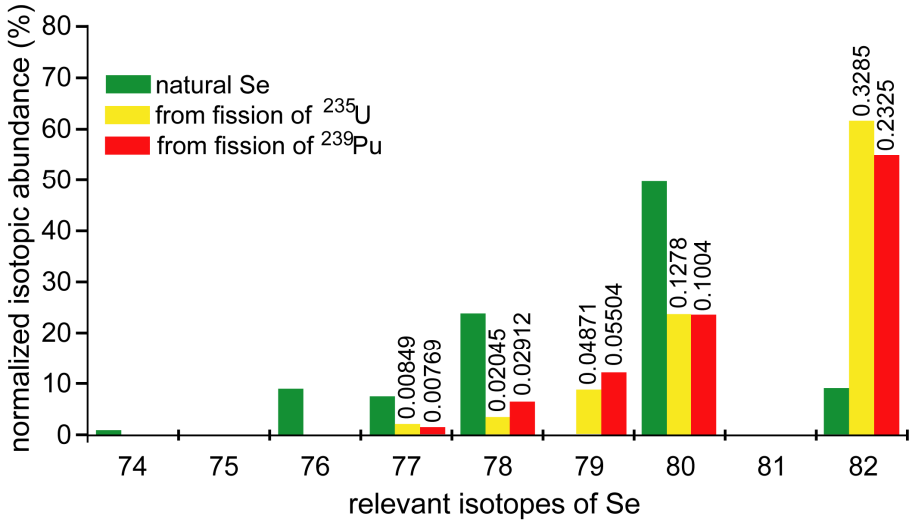

Fig. 2.2: Isotopic composition of natural Se and normalized fission profiles of Se from fission of ^{235}U and ^{239}Pu. Numbers above bars are the actual cumulated fission yields of the respective masses (modified after Jörg et al., 2010).

.

The ^{79}Se decays in a β^- process with a relatively low specific activity of 150.9 keV (Jörg et al., 2010) form the reaction:

$$^{79}_{34}\mathrm{Se} \xrightarrow{\beta-} {}^{79}_{35}Br \qquad (2.1).$$

Concerning the retention of high level nuclear waste (HLW) in deep geological formations for at least one million years, the ^{79}Se isotope is one of the long-term harmful radionuclides due to its high mobility and long lifetime (Bienvenu et al., 2007). The hydrochemical environment for these disposal sites is generally assumed as anoxic with neutral to alkaline conditions

with only a few exceptions, like Yucca Mountain (Nevada, USA) with oxidizing conditions (Geckeis and Rabung, 2008). The assumption that the long-term safety of HLW repositories is possible relies especially on the fact that the most radiotoxic radionuclides, the actinides, are much less mobile than some less radiotoxic anionic fission and activation products such as ^{129}I, ^{36}Cl or ^{79}Se (Geckeis and Rabung, 2008; Grambow, 2008).

Different performance assessment calculations for such repositories show a predominance of the ^{79}Se radionuclide in the total exposure to the biosphere for the period of $10^4 - 10^6$ years after disposal (Fig. 2.3; Takasu et al., 2000; Umeki, 2000; Mallants et al., 2001; Agüero et al., 2008; Malekifarsani and Skachek, 2009). Latest calculations yield a ^{79}Se half-life between $(2.95 \pm 0.38) \cdot 10^5$ and $(3.77 \pm 0.19) \cdot 10^5$ years while the highest accuracy calculates a half-life of $3.27 \cdot 10^5 \pm 8$ years (Jiang et al., 2002; Bienvenu et al., 2007; Jörg et al., 2010).

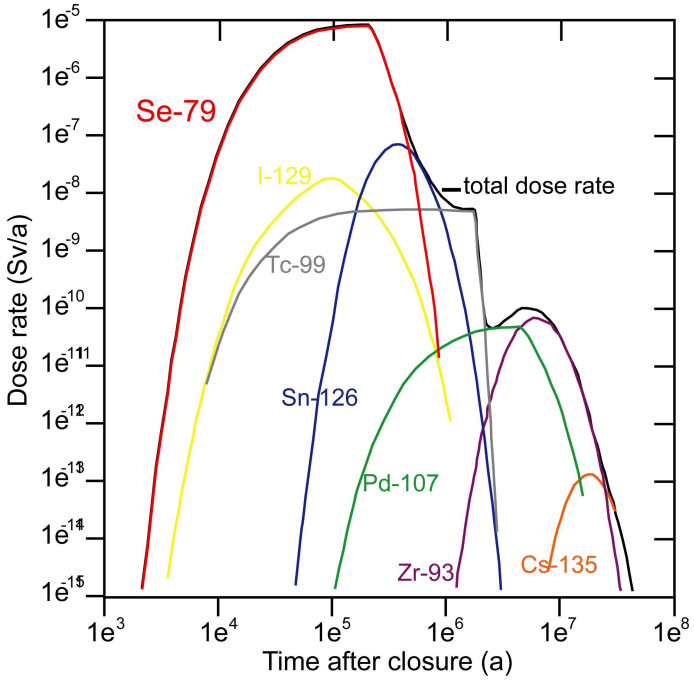

Fig. 2.3: Reference case dose evaluation of activation and fission products for the well pathway in Boom Clay geological formation, Belgium (modified after Mallants et al., 2001).

There is yet some controversy regarding the assumed ^{79}Se concentration in high-level radioactive waste. Séby et al. (1998) assumed a value of ~10^{-7} mol/L Se in the near-field further declining due to migration to 10^{-10} mol/L Se in the biosphere, while Grambow (2008) reports a substantially lower initial concentration of 10^{-9} mol/L Se, equal to 4 Bq/L, in the near-field. Compared to the WHO (2004) proposed maximum of 47 Bq/L of ^{79}Se in drinking-water (corresponding to $1.3 \cdot 10^{-7}$ M for total selenium) the author points out that "if solution concentrations were lower than drinking-water standards already at the waste product/near field interface, no radiological health effect can be expected in hundreds of meters of distance at the interface of the geosphere to the biosphere."

The fate of released ^{79}Se in the near-field of HLW deposits depends highly on the selenium valence state in the vitrified waste, which is part of the technical barrier in the multi-barrier concept for HLW disposal (Grambow, 2008). The multi-barrier concept consists of 3 different barriers to avoid the migration of radionuclides (Fig. 2.4; Kim et al., 2001; BGR 2007).

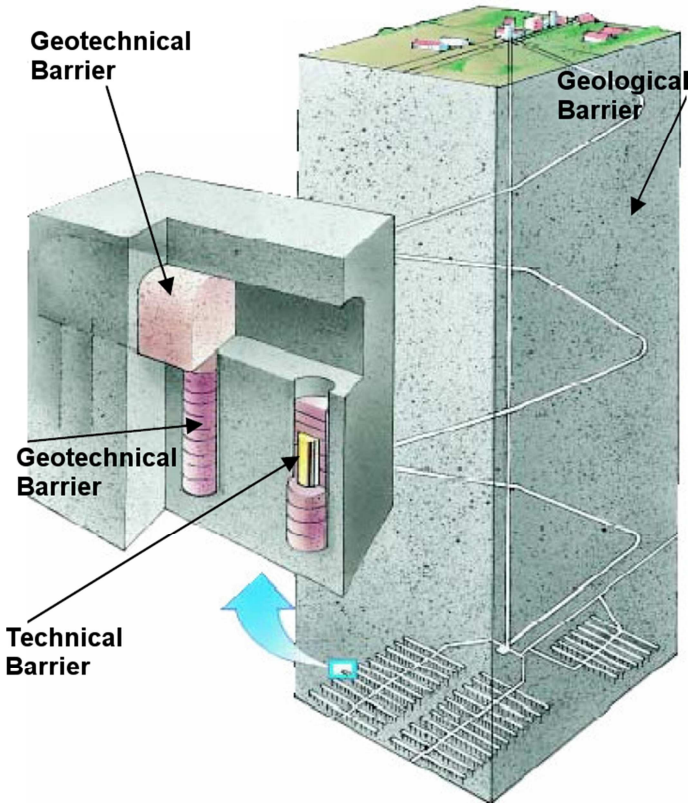

Fig. 2.4: Scheme of the multi-barrier concept for HLW-disposal sites (modified after: http://www.dalton.manchester.ac.uk/facilities/dalton-cumbrian-facility/radioactive-waste-management/).

The technical barrier is built up of the HLW vitrified in a matrix of e.g. borosilicate, and this glass is filled into cases of e.g. steel. The geotechnical barrier is the backfill material (e.g. bentonite, salt grit) to close the open pits, while the geological barrier consists of the local host rock. Especially clay stone, granite and salt as geological formations are examined as applicable host rocks for the storage of high-level radioactive waste (Kim et al, 2001; BGR, 2007).

Of main concern is ^{79}Se in the form of selenate because it does not coprecipitate in substantial amounts with minerals. The reduction rate of Se^{6+} can be very slow in absence of microbially induced reduction (Zhang et al., 2003; He and Yao, 2010), because it involves the transfer of multiple electrons along with multiple oxygen atoms. In general, the higher the oxidation number of Se, the slower is the reduction rate (Séby et al., 1998; De Canniére et al., 2010).

The main species of selenium in the above-mentioned alkali borosilicate glasses is Se^{4+}. However, oxidation due to irradiation resulting from the decay of radioactive elements has to be considered within these vitrified wastes (Bingham et al., 2011). Existing Se^{4+} may be sorbed largely to metal-(oxy)hydroxides or clays. Under the proposed hydrochemical conditions for HLW disposal sites, Se^{4+} may also be reduced to Se^{0} or Se^{2-}. This would lead to the formation of solids, Se^{0} or iron selenides, of very low solubility (Séby et al. 1998; De Canniére et al., 2010).

2.2 Pyrite and mackinawite and their ability for selenium retention

Pyrite (FeS_2) and mackinawite (FeS) are both iron sulfides (Tab. 2.3), which play an important role in the lower temperature environments of ≤25°C, typical for much of the Earth's surface as well as in many biogeochemical processes (Rickard and Luther, 2007).

Pyrite itself is the most widespread sulfide mineral in the Earth´s crust as well as the most important sulfide reservoir in sediments while mackinawite is usually the precursor

precipitating under anoxic and low temperature aqueous conditions (Rickard and Morse, 2005). For the formation of both minerals, a sulfide-source is a prerequisite. Abiotic sulfate reduction at temperatures below ~150°C is kinetica lly extremely slow, but sulfate reduction through microbial respiration is relatively fast and therefore the dominating reduction mechanism. Due to the higher solubility in water, SO_4^{2-} is an available electron acceptor for microbial respiration next to O_2. The general importance of this process is well explained by Rickard and Luther (2007): "Respiration via microbial sulfate reduction is the most important pathway for mineralization of organic matter in marine sediments. Since the mineralization and burial of organic matter ultimately determines the oxygen content of the atmosphere, the fixation of pyrite sulfur in sediments is largely responsible for the oxygenated surface environment of the planet at the present and through much of geological time."

Tab. 2.3: Structure, properties and deposits of selected iron sulfides (Rickard and Luther, 2007).

Mineral	Formula	Structure	Properties	Natural deposits
Pyrite	**FeS_2**	**Cubic *Pa*3**	**stable iron(II) disulfide known as "fool's gold"**	**the most abundant mineral on the Earth's surface**
Marcasite	**FeS_2**	**Orthorombic *Pnnm***	**metastable iron(II) disulfide**	**locally common mineral in hydrothermal systems and in sedimentary rocks**
Pyrrhotite	**$Fe_{1-x}S$**	**variable**	**nonstoichiometric stable group where $x > 0.2$**	**most abundant Fe sulfides in the Earth and solar system; rare in marine systems**
Troilite	**FeS**	**Hexagonal *P*62*c***	**stoichiometric end member of the $Fe_{1-x}S$ group**	**mainly found in meteorites**
Mackinawite	**FeS**	**Tetragonal *P*4/*nmm***	**metastable material, major constituent of FeS precipe-tated from aqueous solutions**	**widespread mineral in low-temperature aqueous environments**
Greigite	**Fe_3S_4**	**Cubic Fd3m**	**metastable $Fe^{II}Fe^{III}$ sulfide; the thiospinel of iron**	**fairly widespread mineral; particularly associated with fresh water systems**

Until today, Fe^{2+} and S^{2-} rich environments can be found in sedimentary pore waters and in deep waters of anoxic basins, where mainly pyrite and the metastable phases mackinawite

and greigite have been observed. On a global perspective, about 5 million tons of pyrite is formed every year in the oceans (Rickard and Luther, 2007).

2.2.1 Structure, formation and occurrence of mackinawite and pyrite

Tetragonal mackinawite is named after the Mackinaw Mine in Washington, where it was found and characterized as a mineral in 1964. Different names exist for this mineral, which has been described as hydrotroilite, kansite, precipitated FeS or amorphous FeS (Rickard and Morse, 2005). The crystal structure of mackinawite consists of sheets of edge-sharing FeS_4 tetrahedra, belonging to space group *P4/nmm* while the cell parameters consist of $a = b = 3.6735$ Å and $c = 5.0329$ Å. The iron atoms are linked to four equidistant sulfur atoms and the Fe-Fe distance is 2.5967 Å (Fig. 2.5; Makovicky, 2006; Rickard and Luther, 2007). The iron sheets are stacked along the *c* axis. Van der Waals forces between the S atoms are holding the sheets together. The stoichiometry of mackinawite is FeS. Deviations from this composition, typically reported in older literature where mackinawite is often noted as $Fe_{1+x}S$, derived from the incorporation of other metals into the mackinawite structure, while the Fe/S-ratio of pure mackinawite is 1:1.

In natural systems, mackinawite has only rarely been found in marine sediments, supposedly due to the low iron aqueous activity ($<10^{-9}$). The precipitation of mackinawite has been reported for inshore marine and freshwater systems with comparatively higher iron concentrations. Mackinawite formation occurs due to the reaction between S^{2-} and Fe^{2+}, while the necessary iron sources are hexaqua-Fe^{2+} or dissolved iron(oxy)hydroxides in natural environment (Rickard and Morse, 2005; Rickard and Luther, 2007). Since mackinawite is a metastable mineral, it is an important temporary sink for many trace metals during the diagenesis in anoxic sediments as long as the mackinawite persists (Morse and Arakaki, 1993).

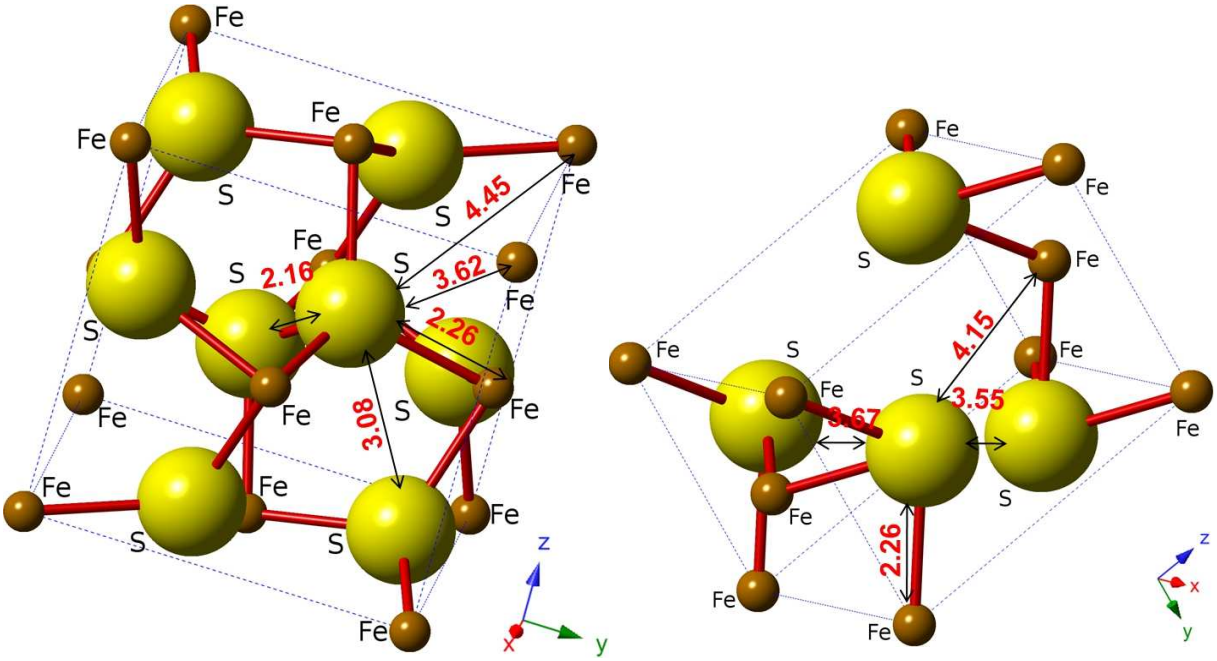

Fig. 2.5: Display of cubic pyrite (left) and tetragonal mackinawite (right) unit cells, together with atomic distances (mackinawite structure data are obtained from Lennie et al., 1995, and pyrite crystal structure from Rieder et al., 2007).

Pyrite, named after the Greek word of fire and well known for his nickname “fool´s gold”, has a NaCl-type structure which belongs to space group *Pa*3 (Fig. 2.5). In the cubic pyrite crystal structure, three coordinated octahedral of low-spin divalent iron are bound to the S_2 double bond without edge-sharing. The S_2^{2-} groups are located at the cube center and at the midpoints of cube edges, while the low-spin Fe^{2+} atoms (d^6, t_{2g}^6) are located at the corners and face centers. The structure has 3-fold axes along the [111] directions and 2-fold axes along the [100] directions. The stoichiometry of pyrite is FeS_2 with a very narrow homogeneity range of less than 1%. Deviations from this composition are due to analytical uncertainties or because of the presence of trace elements in pyrite. The different morphologies of pyrite are cubes, octahedrons and spherulites, with single euhedra and framboids being the most common forms (Wang and Morse, 1996; Morse and Wang, 1997; Rickard and Morse, 2005; Rickard and Luther, 2007).

Pyrite is distributed in a variety of geological settings extending from igneous rocks to sedimentary and hydrothermal deposits, being as well the most abundant phase in sulfide

ore deposits. It is probably only the most widespread iron sulfide on the earth near-surface environments but not from the earth as a whole, because pyrrhotite group minerals are very common in mantle rocks and meteorites where pyrite is not stable and decomposes (Rickard and Luther, 2007; Demoisson et al., 2008).

Figure 2.6 shows idealized, typical vertical profiles for sedimentary pore waters and the water column of enclosed anoxic basins concerning the compounds O_2, NO_3^-, Mn^{2+}, Fe^{2+}, H_2S, and SO_4^{2-} but without consideration of physical forces (bioturbation, vertical and lateral mixing of water due to e.g. storms). Exact concentrations for local profiles are additionally dependent on the deliverance of inorganic and organic matter to the sediment. At the overlap of the curves belonging to soluble species, redox and/or solubility reactions take place, potentially accompanied with the removing of species from solution (Rickard and Luther, 2007).

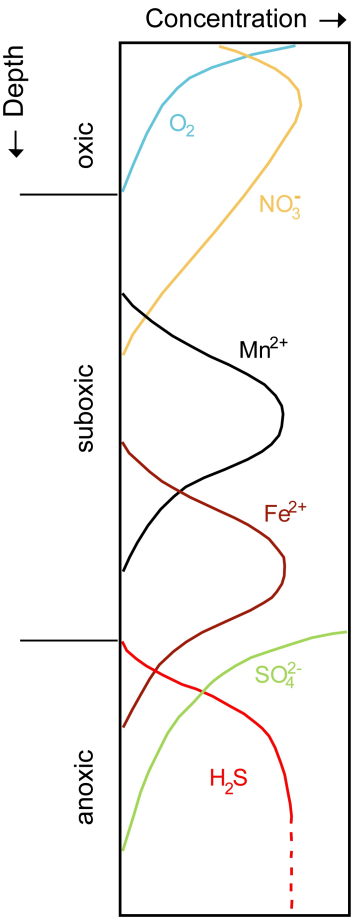

In an idealized profile, the sediment-water interface can be partitioned in three zones. The oxic zone persists until O_2 is depleted. The suboxic region follows below and is characterized by high dissolved manganese and iron concentrations. In the anoxic zone S^{2-} occurs. Permanently anoxic basins are defined as environments with less than 10^{-6} M $O_{2(aq)}$ which also contain sulfide minerals in the scale between micrometer to millimeter. In the anoxic zone, the formation of pyrite can take place especially close to the interface of Fe^{2+} and H_2S curves.

Fig. 2.6: Schematic representation of trends in pore water profiles with depth below the sediment-water interface. The concentrations are not steady units. Moreover, they represent the typical relative occurrence (modified after Rickard and Luther, 2007).

The pyrite formation depends on various rate-limiting factors. In non-euxinic, terrigenous marine sediments, organic matter which is needed for microbiological growth and as catalyst

for microbially induced reduction processes, seems to be the major control on pyrite formation, because dissolved sulfate and iron minerals are sufficiently abundant. By contrast, pyrite formation in non-marine, freshwater sediments is limited due to low concentrations of sulfate. Sufficient H_2S is built under marine euxinic conditions. Here, the dominant rate-controlling factor is the availability of reactive iron minerals of which the most important phases seem to be iron(III)oxyhydroxides, probably in the form of nanoparticulate goethite (Berner, 1984; Rickard and Luther, 2007).

2.2.2 Pyrite in high-level waste disposal sites

Pyrite is part of host rocks and bentonite backfills considered for use in HLW repositories. It may serve as nuclei for further surface coating and as an important iron and sulfur source via dissolution and re-precipitation. Up to 0.4 – 1.9 wt.% pyrite are contained in Callovo-Oxfordian clay (CO; France), 1.1 ± 0.5 wt.% in Opalinus clay (OPA; Switzerland), 1 – 5 wt.% in Boom clay (BC; Belgium), and 0.5 wt.% in bentonite, the most common backfill buffer material (De Craen et al., 2004; Gaucher et al., 2004; Bildstein et al., 2006; Corkum and Martin, 2007; Joseph et al., 2011).

But how likely is a further formation of pyrite? This is difficult to answer, but locally high SO_4^{2-} concentrations of $<6.3 \cdot 10^{-3}$ – $2.5 \cdot 10^{-1}$ mol/L and iron concentrations of up to $1.05 \cdot 10^{-2}$ mol/L were measured in BC squeezed pore water (De Craen et al., 2004). OPA host rock leaching experiments resulted in a release of $1.4 \cdot 10^{-2}$ mol/L of SO_4^{2-} (Joseph et al., 2011) and CO leached pore water contained a mean SO_4^{2-} concentration of $8.27 \cdot 10^{-2}$ mol/L. Furthermore, CO host rocks contained 0.85 – 5.5 wt.% Fe_2O_3 and 0.22 – 1.03 wt.% $S_{[tot]}$ on the average (Gaucher et al., 2004). An additional iron source in geological periods could be the corrosion of steel containers containing vitrified nuclear waste. To sum these results up, iron and sulfur are partly relevant fractions of the varying local environment around to HLW disposals and may initiate the formation of selenium doted pyrite.

2.2.3 Selenium in natural pyrite

One possibility of removing selenium from the solution on a sustained basis is the incorporation into a mineral structure, which is a very efficient type of retardation. Pyrite is the most common near-surface iron sulfide, well-known for its capacity to incorporate elements up to several mol%. During formation, more than 60% of the nonsiliceous bound fraction of potentially toxic elements like As, Cu, Hg in anoxic sediments coprecipitate with pyrite (Morse, 1994; Morse and Luther, 1999; Abraitis et al., 2004; Rickard and Luther, 2007).

In surface sediments, Se is often associated with Fe-Zn-Cu sulfide minerals such as pyrite, marcasite, sphalerite, mackinawite, and chalcopyrite; reported concentrations of selenium in pyrite are between 8 and 760 ppm (Umeki, 2000). High selenium concentrations are often associated with Cu-rich deposits and bituminous coals. The highest ever detected selenium concentration in pyrite was found in a sample from Yutangba, China, with a content of 6.68 wt.%. Further analysis of this sample revealed that selenium was partly incorporated into the pyrite lattice due to isomorphic substitution (Zhu et al., 2004).

Pyrite precipitation at high temperature conditions typically occurs in geological formations of hydrothermal deposits (100° – 350° C). In general, the concentration of selenium which is coprecipitated with pyrite can cover a wide range: 1.3 – 245 ppm Se at Lucky Strike hydrothermal field, Mid-Atlantic ridge; 0 – 300 ppm Se in hydrothermal concretion pipes, Mesozoic shales in SE-France; 0 – 116 ppm Se in Queensland epithermal deposit, Australia (Gaidon et al., 1988; Griffin et al., 1991; Xiong, 2003; Rouxel et al., 2004). These concentrations of coprecipitated selenium in pyrite are relatively low, compared to the possibly three to five times higher uptakes of selenium into chalcopyrite and Ni-sulfide compounds (Orberger et al., 2003).

Selective leaching tests of marine and fresh water sediments showed that selenium seems to be rarely incorporated into pyrite as ideal solid solution by a ferroselite-pyrite or a FeSSe compound, accompanied with an isomorphic substitution of sulfur by selenium (Velinsky and Cutter, 1990).

From uranium ores in quartz-sandstone formations (Seluchekinskoye deposit, Kazakhstan), solid-solutions of pyrite and dzharkenite (cubic $FeSe_2$), a dimorphous of ferroselite with pyrite structure, were reported (Yakovleva et al., 2003). Micro-XAS analysis revealed the speciation and structure of Se in mine-waste rocks, which show that rarely found dzharkenite persists next to Se-substituted pyrite as well as a di-selenide carbon compound (Ryser et al., 2005).

If selenium doted pyrite is exposed to oxidizing conditions, pyrite acts a source for selenium releasing the formerly fixed selenium free into the environment, because oxidative dissolution processes take place (Presser and Swain, 1990; Ryser et al., 2005; Grambow, 2008).

2.2.4 Coprecipitation of trace elements in synthetic pyrite

Aqueous solid solutions are common phenomena in nature. The precipitation of minerals from a multicomponent solution often results in the formation of solids with a certain compositional range (Prieto, 2009). Concerning HLW disposal sites, solid solutions are an essential part of the repository, starting from the waste source, known as near-field, up to the biosphere. A solid solution is defined as “a homogeneous crystalline structure in which one or more types of atoms or molecules may be partly substituted for the original atoms or molecules without changing the structure, although the lattice parameters may vary” (Bruno et al., 2007). The concentrations of the end-members in the solid solution define its stoichiometry. Of importance with regard to the retention of potentially hazardous radionuclides are the distribution ratios R_d, describing the ratio of concentration in one phase to that in another phase. Of concern are especially all those radionuclides with generally low R_d values (like e.g. Se^{6+}) because these dissolved species stay in the solution and do not react substantially with the minerals (Grambow, 2008). The solid-liquid partitioning variable is named as K_d (Ashworth et al., 2008).

In general, if an ion is not in a dissolved state, several possibilities exist for a more or less strong fixation in the soil or rock matrix (Fig. 2.7). The aqueous complexation in form of e.g. colloids could lead to clogging in the pore system of host rocks. Due to the transfer and partitioning of components from the aqueous phase to the surface of a mineral by sorption,

an ion is fixed until the process of desorption takes place. If not, coprecipitation is likely to occur after some time, meaning the precipitation of the component and further crystal growth. Finally, due to ion-diffusion into the crystal structure und further rebuilding by recrystallization, the formation of a solid solution would take place, accompanied with a substitution of an element by keeping the regular crystal system (Bruno et al., 2007).

The precise analysis of the selenium valence state and its distances to atomic neighbors is a prerequisite for the determination of the crystalline structure which results from the Se coprecipitation with minerals. Examples are the reduction of Se^{4+} to Se^{0} by diffusion from ponded waters to sediments (Tokunaga et al., 1998) or Se^{4+} reduction by sorption onto montmorillonite (Charlet et al., 2007).

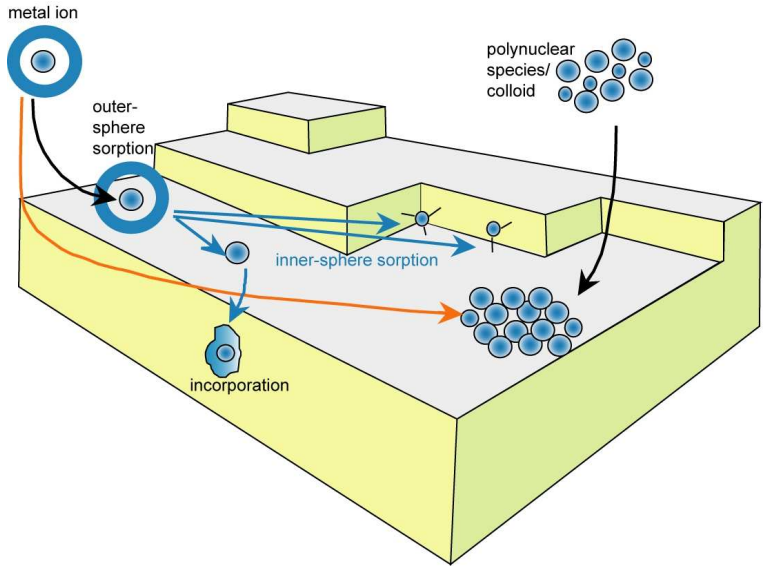

Fig. 2.7: Scheme of the different possible states of ion-bonding with a mineral (modified after Manceau et al., 2002).

Scheinost et al. (2008a, 2008b) examined Se^{4+} reduction at nanoparticulate mackinawite (FeS). The results showed that the redox reaction is kinetically fast and takes place within one day. The mineral precipitations are pH dependent. At pH 4.4, FeSe precipitates, while at pH 6.3 Se^{0} is dominant. This is probably due to the much higher solubility of mackinawite at

decreasing pH. For FeSe precipitations, S^{2-} and Fe^{2+} surface atoms are oxidized at a ratio of 1:4.

A XAS study about the migration behavior of Se^{6+} in a granite drill core showed that generally sulfide bearing minerals and especially FeS were the most efficient minerals to immobilize Se^{6+} accompanied with a partial reduction into more reduced Se forms at the mineral surface (Yllera de Llano et al., 1996). It is important to note that the trace element concentration incorporated in metastable mackinawite is not necessarily equal to the concentration in pyrite, because its trace element load is released back into solution during mackinawite dissolution (Rickard and Luther, 2007).

By introducing a Se^{4+} solution into reducing Boom clay environment, Bruggeman et al. (2005) detected an adsorption of Se^{4+} at the pyrite surface, which led to its reduction and precipitation as Se^0 after 60 days. The Se^0 had a very low solubility of $3 \cdot 10^{-9}$ M. Breynaert et al. (2008) confirmed these results, because they noticed a Se^{4+} reduction to Se^0 after three weeks of solution contact with pyrite, and to $FeSe_x$ with troilite (mainly found in meteorites with chemical sum FeS). The authors found out that the type of sulfide mineral dictates the final speciation.

Naveau et al. (2007) investigated the sorption of Se^{2-} and Se^{4+} on natural and synthetic pyrite under ambient conditions after 1 d of stirring. The percentage of sorbed selenium is very similar for both valence states. For synthesized pyrite, the sorption efficiency exceeds >95 % under acidic pH conditions (<6) and drops rapidly down to less than 5% of the initial sum at neutral to alkaline conditions (pH 7 – 10). Though the specific surface area (SSA) of synthesized pyrite (0.8 m^2/g) was even smaller than of natural pyrite (1.1 m^2/g), the sorbed fraction for the second one is generally much less, starting with ~60 % at pH ~2 and dropping linearly to a sorption of ~20 % at pH 5. The newly formed precipitates contained reduced Se species while only pyritic sulfur oxidized but not pyritic iron.

Liu et al. (2008) observed an oxidation of Se^{2-} to Se^0 by adsorption onto synthetic pyrite (SSA: 4.8 m^2/g) under strongly reduced conditions (-340 mV) within 1 d in an electrochemical cell, accompanied by a cleavage of S-S bonding and a reduction to HS^-:

$$FeS_2 + HSe^- \leftrightarrows FeS + Se^0 + HS^- \quad (2.2).$$

The sorption kinetics was extremely fast, because >97 % of initial Se^{2-} was removed from the solution within 5 minutes. The K_d values for $10^{-4} - 10^{-6}$ mol/L Se^{2-} in solution are ranging between 7 and 65 L/g. The distribution values were decreasing with higher initial Se^{2-} contents due to full site occupation.

The predictions of equilibrium thermodynamic calculations with regard to selenium incorporation into pyrite under reduced conditions are not consistent. Masscheleyn et al. (1990) proposed that a mixed solid solution phase would be formed with selenide substituting for sulfide and precipitated iron sulfide will contain FeSe. Howard (1977) instead calculated that Se^0 incorporates into pyrite or that ferroselite ($FeSe_2$) precipitates. In a thermodynamic study simulating the hydrological processes in hydrothermal solutions, it is predicted that the selenium species Se^0 and Se^{2-} are dominating (Xiong, 2003). Commonly accepted is that elemental Se has a wide stability field under acid conditions and that formation of achavalite is favored for neutral to alkaline conditions (Lenz and Lens, 2009).

To sum up, the geochemistry of selenium is largely controlled by iron bearing minerals under oxidizing and reducing conditions (Zingaro et al, 1997; Séby et al., 1998). Selenium adsorption behavior on mineral surfaces depends highly on its oxidation state. Selenate sorption is lower than those of selenite and much less than selenide sorption on the different iron sulfides. The probable reason for the weaker sorption of Se^{6+} is the formation of outer sphere complexes at the mineral surfaces. Selenite has a comparatively strong affinity to metal oxides and metal hydroxides. The sorption mechanism of selenite involves very often a ligand exchange reaction with formation of an inner sphere surface complex. The precipitation/dissolution reactions govern selenium solubility only in reduced conditions with formation of Se^0 and $Me^{2+}Se^{2-}$-compounds. Selenide could replace sulfide in the pyrite structure because of similar radii and equal charge (Séby et al., 1998; Lenz and Lens, 2009). Up to date, only Se^{2-} and Se^{4+} sorption on pyrite surfaces has been investigated, but there is no experimental study about incorporation into the crystal lattice yet.

With regard to the incorporation of Se into pyrite, probable types of binding are $FeSe_2$-FeS_2 solid solutions ($FeSe_2$ as ferroselite or dzharkenite), furthermore an isomorphic substitution ending in a FeS_xSe_y compound or the fixation of Se^0 without any bonding. For mackinawite, solid solutions of FeSe-FeS (FeSe as achavalite) could form or Se^0 becomes incorporated. Assuming an equilibrium system, the formation of both, pyrite and $FeSe_2$ next to each other or as solid-solution phase could be possible because of their very similar solubility products. Taken the thermodynamic values from WATEQ4F database (which is integrated e.g. in the open source software PhreeqC and noted in Ball and Nordstrom, 2001), pyrite has a $\log_{10} K_{SP}$ = -18.48 and $FeSe_2$ a $\log_{10} K_{SP}$ = -18.58.

The type of bonding of selenium in pyrite is important because the stability of fixed selenium is supposably higher in a real solid solution accompanied with Se bonding with Fe and/or S. Now it is interesting to see, if the often proposed formation of FeS_xSe_y-compounds or the incorporation of Se^0 into pyrite structure takes place under different hydrochemical and temperature conditions. Therefore, our investigations focus on Se^{2-} and Se^{4+} incorporation into pyrite and mackinawite as solid solution phase for anoxic conditions; conditions which are also predicted for nuclear waste repositories. Hence, the investigations should clarify the type of structural bonding as a function of the initial aqueous valence state of incorporated selenium.

2.3 The aqueous iron-sulfur-selenium system

Knowledge about the speciation of dissolved aquatic compounds is important in order to understand potential reaction pathways that may lead to precipitation of solid phases. Thermodynamic modeling can provide predictions of geochemical processes (e.g. mineral solubility, aqueous speciation), if the underlying thermodynamic data are accurate and complete with regard to the modeled solution (Faure, 1998; Oelkers et al., 2009).

In general, there are two different ways to carry out thermodynamic calculations with respect to the distribution of aquatic species. One possibility is the determination of the most stable

phases by minimization of the enthalpies of formation (e.g. GEMS, CHEMSAGE). The second way is to calculate the most stable phases for all equilibrium constants in the system (e.g. PhreeqC, EQ3/6). Both methods presuppose the setting of a chemical equilibrium within the aqueous solution (Merkel and Planer-Friedrich, 2008). The thermodynamic calculations in this study have been performed by the open source software PhreeqC using the integrated, comprehensive WATEQ4F database (Parkhurst and Appelo, 1999). The list of all integrated equilibrium constants is noted in appendix A while the most relevant species are noted in this chapter. Therefore, the predominantly aqueous dissolved Fe-, S-, Se-species and the solid phases mackinawite and pyrite conditions are presented for certain pH-Eh values in Pourbaix-diagrams as well as their stability constants or solubility products with belonging reactions. Pourbaix diagrams display the stability fields for a given solution with defined activities of the phases under defined temperature and pressure conditions. Of course, it has to be kept in mind that these stability fields are changing if e.g. the solution composition is modified, but it gives generally a good impression of the expected species for certain pH-Eh conditions. Apart from the most stable phase, further species occur with significant activities especially close to the boundaries of a stability field (Merkel and Planer-Friedrich, 2008).

2.3.1. Sulfur

The stability diagram for dissolved sulfur species shows that sulfate (SO_4^{2-}) dominates completely under oxidized conditions (Fig. 2.8):

SO_4^{2-}	$SO_4^{-2} \leftrightarrows SO_4^{2-}$	($\log_{10} K = 0.0$)
HSO_4^-	$H^+ + SO_4^{2-} \leftrightarrows HSO_4^-$	($\log_{10} K = 1.988$)

Only a comparatively small stability field under acidic conditions is covered by rhombic, elemental sulfur, of which the composition is normally noted as S^0 but in fact it occurs as S_8:

S^0	$S + 2e^- \leftrightarrows S^{2-}$	($\log_{10} K_{SP} = -15.026$)

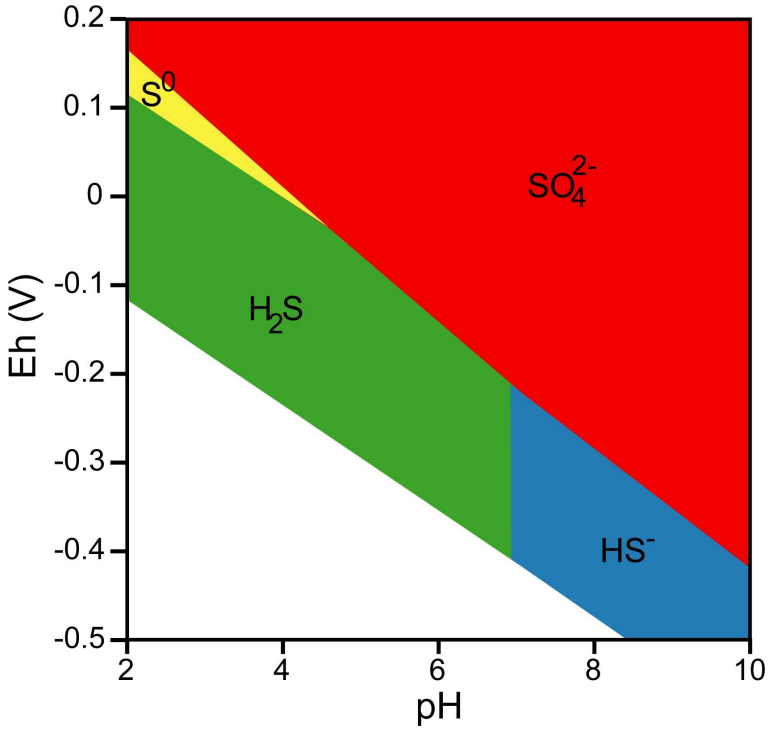

Fig. 2.8: Pourbaix diagram for $[S_{tot}] = 10^{-3}$ M at standard conditions (modified after Rickard and Luther, 2007).

Under reduced conditions, H_2S dominates up to pH 7 and HS^- under reduced alkaline conditions (Rickard and Luther, 2007):

$H_2S_{(aq)}$	$SO_4^{2-} + 10H^+ + 8e^- \leftrightarrows H_2S + 4H_2O$	($\log_{10} K = 40.644$)
$H_2S_{(g)}$	$H_2S \leftrightarrows H_2S$	($\log_{10} K = -0.997$)
HS^-	$H_2S \leftrightarrows HS^- + H^+$	($\log_{10} K = -6.994$)
S^{2-}	$HS^- \leftrightarrows S^{2-} + H^+$	($\log_{10} K = -12.918$)

HS^- and H_2S are the most important dissolved species which serve as sulfide-sources for iron sulfide formation, indicated by the $\log_{10} K\,(HS^-) = 6.99$ for an aqueous solution containing $[S_{tot}] = 10^{-3}$ M (Fig. 2.9). The species H_2S is dominating under acidic conditions but HS^- as the minor species has still a significant activity close to slightly acidic up to neutral conditions. The activity (maximum at pH 10: ~10^{-11}) of the aqueous ion S^{2-} is negligible (Rickard and Morse, 2005; Rickard and Luther, 2007).

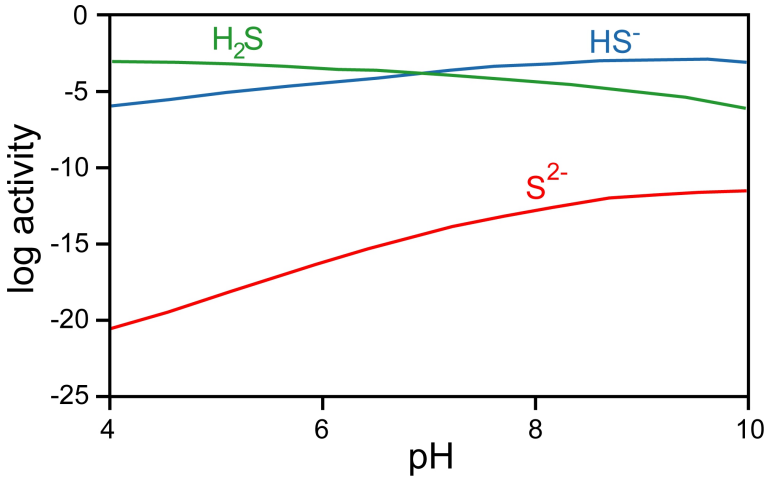

Fig. 2.9: Distribution of aqueous sulfide species at $[S^{2-}_{tot}] = 10^{-3}$ M at 25°C and 1 bar pressure (modified after Rickard an d Luther, 2007).

Since pyrite is an iron disulfide, it is well possible that a disulfide species could be involved in its formation. Disulfides are part of the polysulfides, which consist of chains of sulfur atoms and they are noted as S_n^{2-} with n = 2 – 8. Solutions of polysulfides are mixtures of S_n^{2-}, S^{2-}, and S^0 species and their protonated forms:

S_2^{2-}	$HS^- + HS^- \leftrightarrows S_2^{2-} + 2H^+$	($\log_{10} K$ = -14.528)
S_3^{2-}	$HS^- + S_2^{2-} \leftrightarrows S_3^{2-} + H^+$	($\log_{10} K$ = -13.282)
S_4^{2-}	$HS^- + S_3^{2-} \leftrightarrows S_4^{2-} + H^+$	($\log_{10} K$ = -9.829)
S_5^{2-}	$HS^- + S_4^{2-} \leftrightarrows S_5^{2-} + H^+$	($\log_{10} K$ = -9.595)
S_6^{2-}	$HS^- + S_5^{2-} \leftrightarrows S_6^{2-} + H^+$	($\log_{10} K$ = -9.881)

Excluding stable sulfide species and rhombic sulfur from Pourbaix diagram (Fig. 2.8) reveals the underlying metastable polysulfide distribution (Fig. 2.10). Around the SO_4^{2-}/S^{2-} redox boundary at pH 2 – 6, where originally S^0 is the most stable phase, the dominant polysulfide species in this context are the longer chained S_8^{2-} and S_6^{2-}. Remarkable is the relative stability of HS_2^- above pH 5 which contributes to ~1 % of the total dissolved sulfide concentration in much of the system (Rickard and Morse, 2005; Rickard and Luther, 2007).

.

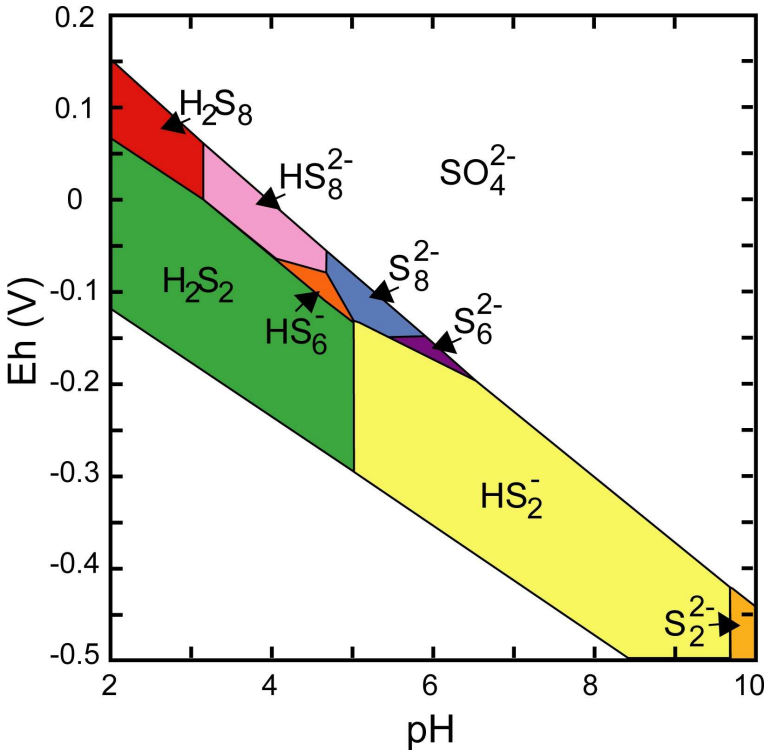

Fig. 2.10: Stability diagram of polysulfide distribution for [S_{tot}] = 10^{-3} M after excluding stable phases from the calculations (modified after Rickard and Luther, 2007).

Equation 2.3 describes the further formation of polysulfides:

$$S^{0}_{(s)} + S_{n-1}{}^{2-}{}_{(aq)} \rightarrow S_{n}{}^{2-}{}_{(aq)} \qquad (2.3).$$

Under hydrochemical conditions without excess rhombic sulfur present, the total activity of polysulfide species is negligible because it approaches activities of 10^{-12} at pH <7 (equal to 10 ppm) and 10^{-15} at pH >7 (equal to 0.1 ppb) of the total sulfide activity. The polysulfide activity reaches a maximum close to the sulfate/sulfide boundary zone in low-temperature natural systems (Rickard and Morse, 2005; Rickard and Luther, 2007).

2.3.2 Iron

The formation of iron sulfides in natural aqueous systems involves reactions of a sulfur source with iron species. The ferrous ion in aqueous solution is commonly written as Fe^{2+},

which is the short notation form for the stoichiometric composition of the hexaqua species $Fe(H_2O)_6^{2+}$:

Fe^{2+}	$Fe^{2+} \leftrightarrows Fe^{2+}$	($\log_{10} K = 0.0$)
Fe^{3+}	$Fe^{2+} \leftrightarrows Fe^{3+} + e^-$	($\log_{10} K = -13.020$)
$FeOH^{2+}$	$Fe^{3+} + H_2O \leftrightarrows FeOH^{2+} + H^+$	($\log_{10} K = -2.19$)
$FeOH^+$	$Fe^{2+} + H_2O \leftrightarrows FeOH^+ + H^+$	($\log_{10} K = -9.5$)
$Fe(OH)_3$	$Fe^{+3} + 3H_2O \leftrightarrows Fe(OH)_3 + 3H^+$	($\log_{10} K = -12.56$)

The stability diagram for iron shows Fe^{2+} as most important stable species for both, reduced and moderate oxidizing up to slightly alkaline aqueous conditions (Fig. 2.11), while $FeOH^+$ has a significant activity under reduced alkaline conditions. Solid $Fe(OH)_3$ is the most stable phase under oxidizing, acidic up to reduced alkaline conditions.

The stable mineral phases in the Fe-H_2O system at 25°C and 1 bar pressure are hematite (Fe_2O_3), magnetite (Fe_3O_4), wüstite (FeO) and goethite (α-FeOOH) (Rickard and Luther, 2007):

Magnetite	$Fe_3O_4 + 8H^+ \leftrightarrows 2Fe^{3+} + Fe^{2+} + 4H_2O$	($\log_{10} K_{SP} = 3.737$)
Hematite	$Fe_2O_3 + 6H^+ \leftrightarrows 2Fe^{3+} + 3H_2O$	($\log_{10} K_{SP} = -4.008$)
Maghemite	$Fe_2O_3 + 6H^+ \leftrightarrows 2Fe^{3+} + 3H_2O$	($\log_{10} K_{SP} = 6.386$)
Goethite	$FeOOH + 3H^+ \leftrightarrows Fe^{3+} + 2H_2O$	($\log_{10} K_{SP} = -1.0$)

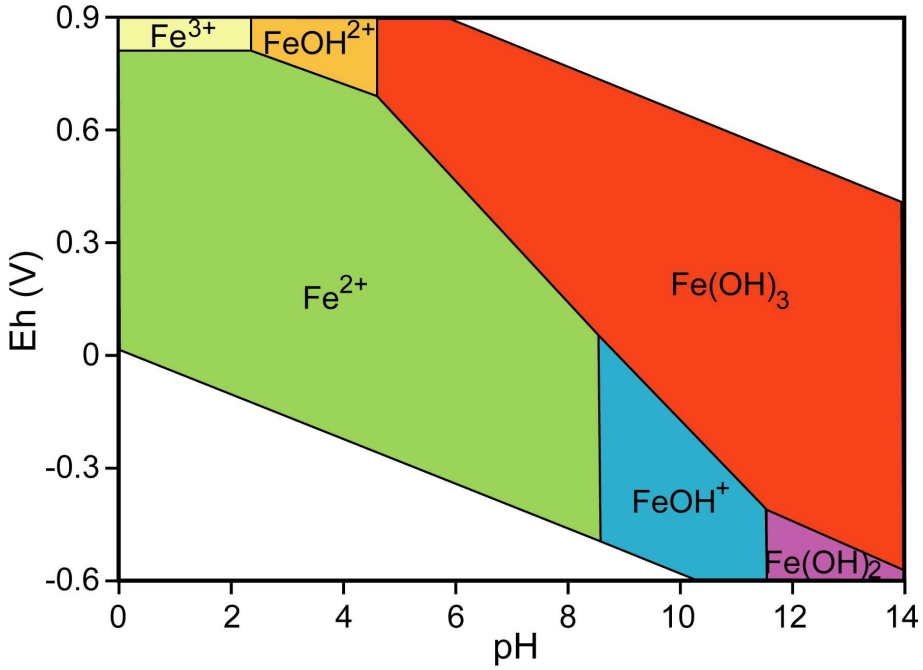

Fig. 2.11: Pourbaix diagram for dissolved [Fe_{tot}] = 10^{-3} M at standard conditions, 25°C, 1 bar pressure (modified after Rickard and M orse, 2005).

Aqueous FeS clusters

Presumably FeS clusters (FeS_{aq}) are ubiquitous in sulfidic aqueous environments, which transport Fe^{2+} in S^{2+}-rich systems and both are involved in iron sulfide formation (Rickard and Luther, 2007). These clusters may form from dissolved Fe-S species:

$FeSO_4$	$Fe^{2+} + SO_4^{2-} \leftrightarrows FeSO_4$	($\log_{10} K = 2.25$)
$Fe(SO_4)_2^-$	$Fe^{3+} + 2SO_4^{2-} \leftrightarrows Fe(SO_4)_2^-$	($\log_{10} K = 5.38$)
$Fe(HS)_2$	$Fe^{2+} + 2HS^- \leftrightarrows Fe(HS)_2$	($\log_{10} K = 8.95$)
$Fe(HS)_3^-$	$Fe^{2+} + 3HS^- \leftrightarrows Fe(HS)_3^-$	($\log_{10} K$ =10.987)

The FeS_{aq} concentration is linearly correlated with pyrite formation in estuarine sediments (Rickard and Luther, 2007). Its stoichiometry ranges from Fe_2S_2 to $Fe_{150}S_{150}$ which is identical with the first condensed phase of mackinawite. The analyzed structure of the aqueous cluster Fe_2S_2 and Fe_4S_4 is relatively similar to the mackinawite crystal model (Wolthers, 2003; Rickard and Morse, 2005; Rickard and Luther, 2006).

2.3.3 Selenium

In aquatic environments, selenium behavior is quite complex because it exists in the oxidation states −II, 0, +IV and +VI in nature, in both inorganic and organic forms, in solid, liquid and gas phase and in 6 stable isotopes and 9 radionuclides (Schrauzer, 2004; Lenz and Lens, 2009). Selenium can interact with mineral phases, can be bound to organic or inorganic ligands, can be part of occurring redox processes or may be transformed by microorganisms. Under the presumed anoxic and anaerobic hydrochemical conditions in a radioactive waste disposal, the most stable forms would be Se^{2-}, Se^{0}, Se^{4+}. But the presence of Se^{6+} is also considered because of the low kinetic of its reduction (Séby et al., 1998; Lenz and Lens, 2009).

Under reducing conditions, selenium appears as Se^{0} in a wide pH range. Compared to sulfur, elemental selenium has a much broader stability field. Under highly reducing conditions, selenide (in form of the species: HSe^-, H_2Se) is stable with HSe^- as major Se species in solution (Fig. 2.12). Both represent 80 – 100 % of the total selenium content below the potential of zero (Séby et al., 1998) and the dissolved species are transformed due to following reactions:

HSe^-	$SeO_3^{2-} + 7H^+ + 6e^- \leftrightarrows HSe^- + 3H_2O$	($\log_{10} K = 42.514$)
H_2Se	$HSe^- + H^+ \leftrightarrows H_2Se$	($\log_{10} K = 3.8$)
Se^0	$Se + H^+ + 2e^- \leftrightarrows HSe^-$	($\log_{10} K_{SP} = -17.322$)

Seven different allotropic forms exist for elemental selenium, including hexagonal (grey), different monoclinic (red), different cubic, a rhombohedric and an ortho-rhombic form (Schrauzer, 2004). In the non-metallic Se-modification, the selenium atoms are structured in form of eight-membered rings, like sulfur. In its hexagonal metallic form, Se^0 shows the properties of a semiconductor, since its electrical conductivity increases with temperature. As well, Se_6, Se_7 and Se_8 rings have been detected in organic solvents being in equilibrium with each other. Furthermore, Se^0 can be mixed with S in any ratio (Schrauzer, 2004; Lenz and Lens, 2009).

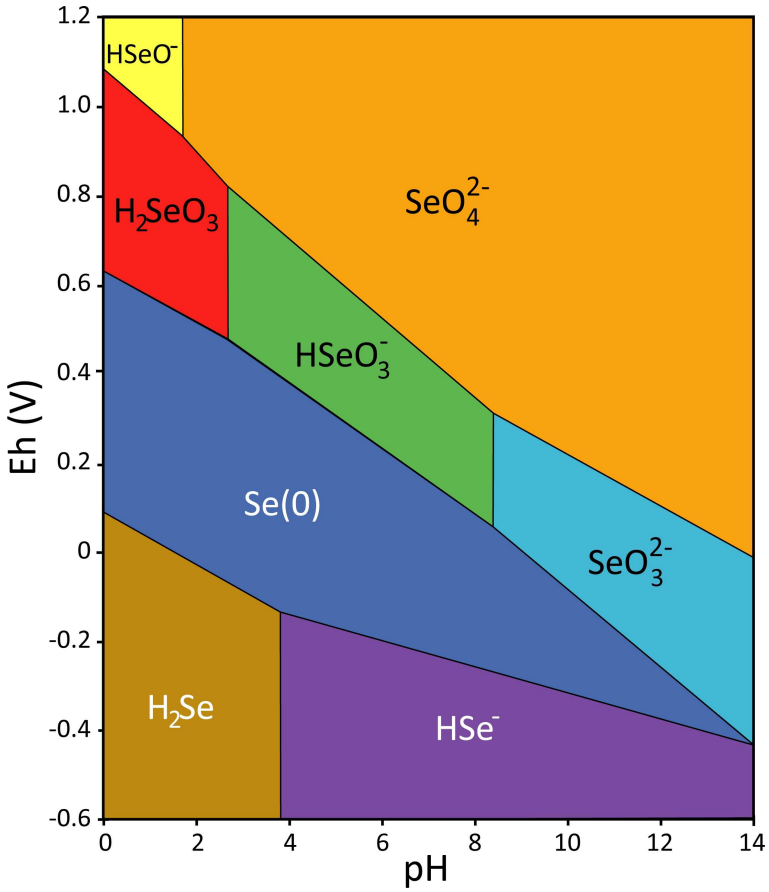

Fig. 2.12: Pourbaix diagram for [Se_{tot}] = 10^{-6} M at standard conditions (modified after Olin et al., 2005).

Selenite (as SeO_3^{2-}, $HSeO_3^-$, H_2SeO_3) is predominant under moderate redox conditions, e.g. ~0.6 V at pH 4 and ~0 V at pH 10. Under highly oxidizing conditions, selenate (as SeO_4^{2-}, $HSeO_4^-$) is stable mainly as SeO_4^{2-} over a wide pH range. Both species are typical for surface waters and oxidized groundwater where they occur mostly in particulate-associated form. Furthermore, they have a high bioavailability and bioaccumulation potential (Séby et al., 1998; Olin et al., 2005):

SeO_4^{2-}	$SeO_4^{2-} \leftrightarrows SeO_4^{2-}$	($\log_{10} K = 0.0$)
SeO_3^{2-}	$SeO_4^{2-} + 2H^+ + 2e^- \leftrightarrows SeO_3^{2-} + H_2O$	($\log_{10} K = 30.256$)
H_2SeO_3	$SeO_3^{2-} + 2H^+ \leftrightarrows H_2SeO_3$	($\log_{10} K = 11.25$)
$HSeO_3^-$	$SeO_3^{2-} + H^+ \leftrightarrows HSeO_3^-$	($\log_{10} K = 8.5$)
$HSeO_4^-$	$SeO_4^{2-} + H^+ \leftrightarrows HSeO_4^-$	($\log_{10} K = 1.66$)

Both, Se^{2-} and Se^{0} are oxidized to selenite close to neutral conditions and Se^{4+} is oxidized to Se^{6+} above ~0.6 V at pH 4 and ~0.2 V at pH 10, which happens fast at alkaline pH- and slow at acidic pH-values. Under highly oxidizing conditions of 450 mV, selenate species are stable with a share of 75 % for pH-values close to 7 and 95 % at pH-values ranging from 8.5 to 9 (Masscheleyn et al., 1990; Séby et al., 1998). The most stable solid Fe-Se phase under reducing conditions is ferroselite:

Ferroselite	$FeSe_2 + 2H^+ + 2e^- \leftrightarrows Fe^{2+} + 2HSe^-$	($\log_{10} K_{SP}$ = -18.580)

Redox-transformations between these species are often microbially mediated (Séby et al., 1998). Biotic transformations of selenium species can be categorized as assimilatory and dissimilatory reduction, alkylation, dealkylation and oxidation reactions. All types of reduction from Se^{6+} and Se^{4+} to Se^{0}, from Se^{0} to Se^{2-} as well as the 3 - 4 times slower oxidation of reduced selenium valences under oxidizing conditions can be facilitated by microorganisms. Microbes use Se^{6+} and Se^{4+} as terminal electron acceptors for growth support reducing these species into red and amorphous Se^{0} with Se^{4+} as intermediate species. The microbial reduction of Se^{0} into Se^{-2} was also reported for strongly reducing conditions with toxically, gaseous H_2Se as final compound (Séby et al., 1998; Séby et al., 2001; Lenz and Lens, 2009).

2.3.4 Iron sulfide reaction pathways

A Pourbaix diagram with a Fe/S ratio of 1:2 for the Fe-S-H_2O system is shown in Figure 2.13. Pyrite has a stability field covering the whole pH range from 0 – 14, with an Eh-gradient from slightly oxidizing conditions at highly acidic conditions to reducing conditions under an alkaline pH-value. Mackinawite (FeS) is only stable under more reducing conditions than pyrite:

Mackinawite	$FeS + H^+ \leftrightarrows Fe^{2+} + HS^-$	($\log_{10} K_{SP}$ = -4.648)
Greigite	$Fe_3S_4 + 4H^+ \leftrightarrows 2Fe^{3+} + Fe^{2+} + 4HS^-$	($\log_{10} K_{SP}$ = -45.035)
Pyrite	$FeS_2 + 2H^+ + 2e^- \leftrightarrows Fe^{2+} + 2HS^-$	($\log_{10} K_{SP}$ = -18.479)

Pyrrhotite ($Fe_{1-x}S$) and troilite (FeS) have no stability fields under these conditions, which is in agreement with studies concerning marine sediments where they were merely found. Pyrrhotite is the most important iron sulfide in the earth mantle and troilite is often found in meteorites (Rickard and Luther, 2007).

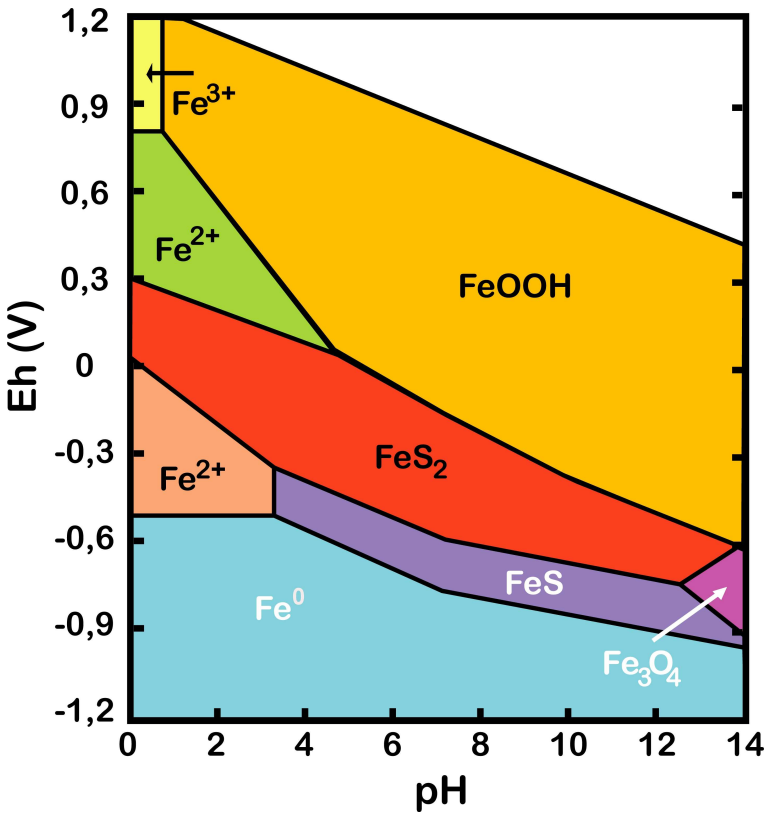

Fig. 2.13: Pourbaix diagram for the Fe-S-H_2O system at 25°C and 1 bar pressure for $[S_{tot}]$ = 0.067 M, $[Fe_{tot}]$ = 0.033 M (modified after Wei and Osseo-Asare, 1997).

Mackinawite formation and kinetics at standard conditions

The HS^- and H_2S species are the dominant sulfides in aqueous solutions at 25° C and 1 bar pressure (Ch. 2.3.1). Due to this fact, two reaction pathways exist for mackinawite precipitation, which are pH dependent (Rickard and Morse, 2005). Under acidic conditions, the reaction will follow mainly as

$$Fe^{2+}_{(aq)} + H_2S_{(aq)} \leftrightarrows FeS_{(s)} + 2H^+ \quad (2.4).$$

It is presumed that the FeS_{aq} cluster $Fe(HS)_{2(aq)}$ is a complex of the intermediate reaction steps for mackinawite formation via HS^- (Ch. 2.3.3). Under pH-conditions above 7, the dominant mackinawite formation pathway mainly is:

$$Fe^{2+}_{(aq)} + HS^-_{(aq)} \leftrightarrows FeS_{(s)} + H^+ \quad (2.5).$$

The kinetics of mackinawite formation are extraordinarily fast, because it takes only 1 ms up to 1 s to precipitate (Rickard and Morse, 2005; Rickard and Luther, 2007), on the basis of the following rate law:

$$\Delta FeS/\Delta t = k \cdot \{Fe^{2+}\} \cdot \{H_2S\} \quad (2.6)$$

with ΔFeS being the rate of mackinawite formation in mol/L·s, k as the rate constant amounting to $\log k = 7 \pm 1$ L/mol·s and $\{Fe^{2+}\}$ and $\{H_2S\}$ as the iron and H_2S activities. Iron disulfides dissolve only in the presence of an oxidizing agent while FeS (mackinawite and troilite) can dissolve oxidatively as well as non-oxidatively (Rickard and Luther, 2007; Breynaert et al., 2008).

In older literature (e.g. Morse and Cornwell, 1987; Lennie et al., 1995), mackinawite was named as an essential precursor phase for pyrite formation at ambient conditions. Because it is thermodynamically metastable under near-surface conditions, it transforms as solid-state formation to greigite; or it dissolves, enabling pyrite formation during burial diagenesis in sediments, since the solubility product of mackinawite is much greater than that of pyrite. But mackinawite is just one important Fe-source among other minerals like FeOOH, Fe_2O_3, $Fe(OH)_3$, green rust, or other Fe phases that react with sulfide to form pyrite. Nanoparticulate mackinawite (size: ~2 nm) nucleation is extremely quick in low-temperature aqueous environments and it is usually the first iron sulfide precipitating. But it only subsists, because the formation of pyrite is kinetically hindered (Rickard and Morse, 2005; Rickard and Luther, 2007).

Pyrite formation and kinetics at standard conditions

The pyrite formation reaction under standard conditions is determined by two alternative mechanisms, which are named as H_2S and polysulfide pathway (Rickard and Morse, 2005). The generation of pyrite (Fig. 2.13) follows a progressive sulfidation, dissolution and precipitation pathway by involving changes in aqueous sulfur speciation (Schoonen and Barnes, 1991; Wang and Morse, 1996; Morse and Wang, 1997; Benning et al., 2000). Furthermore, usually an intermediate mineral is involved, such as mackinawite, greigite, magnetite, or goethite, which provides a necessary source of iron (Eq. 2.7). Afterwards, a dissolved FeS intermediate is required for pyrite formation (Wei and Osseo-Asare, 1997; Benning et al., 2000; Rickard and Luther, 2007). Known as the "Bunsen Reaction" or "Polysulfide pathway" (Rickard and Luther, 2007), Equation 2.8 describes the reaction of dissolved FeS with polysulfide species (Fig. 2.9):

$$Fe^{2+}_{(aq)} + HS^-_{(aq)} \rightarrow FeS_{(s)} + H^+ \quad (2.7).$$

$$FeS_{(aq)} + S_n^{2-}{}_{(aq)} \rightarrow FeS_{2(s)} + S_{n-1}^{2-}{}_{(aq)} \quad (2.8).$$

The rate of pyrite formation in the presence of polysulfides is first order and increases with increasing polysulfide concentration (Rickard and Luther, 2007). The nucleophilicity for pyrite precipitation varies in the sequence $S_5^{2-} > S_4^{2-} > HS^- > HS_2^- > S_3^{2-} > H_2S$, indicating that the polysulfide pathway is especially important near the sulfide/sulfate redox boundary (Rickard and Luther, 2007). In this zone, the dominant sulfide species in the stability field of rhombic elemental sulfur are polysulfides with $n \geq 5$. Hence, their relative abundance is expected to raise the rate of pyrite formation (Luther, 1991; Rickard and Luther, 2007).

Additionally, in all reported laboratory syntheses of pyrite, its formation happened via the "H_2S-pathway" or "Berzelius Reaction" (Rickard and Morse, 2005):

$$FeS_{(s)} + H_2S \rightarrow [Fe–S \rightarrow SH_2] \rightarrow FeS_{2(s)} + H_{2(g)} \quad (2.9).$$

The term $[Fe–S \rightarrow SH_2]$ is a dissolved FeS transition intermediate. The reaction involves the formation of an inner sphere complex between FeS and H_2S followed by an electron transfer

between S^{2-} and H^{+} for S^{-} production. It is important to note that most aqueous environments where pyrite precipitation occurs include both, polysulfides and monosulfides, meaning that both reaction pathways take place, simultaneously. Highly relevant is the acceleration of both pathways by a factor of up to 10^5 through bacterial sulfur disproportionation (Rickard and Luther, 2007).

The formation of pyrite is divided into two kinetically different processes. The nucleation is normally the rate-limiting factor because it is slow and requires relatively high supersaturations and/or catalytic effects of active surfaces. The crystal growth itself is comparatively rapid and takes place through the reaction between Fe^{2+} and S_2^{2-}, which is present in sufficient concentrations in any experimental or natural S_2^{2-} solution for pyrite formation (Rickard and Luther, 2007).

The processes for the pyrite nucleation on metastable iron sulfides, especially mackinawite and greigite, are heterogeneous nucleation as an epitaxial overgrowth of pyrite nuclei at defects on their mineral's surface and the formation of pyrite clusters which are smaller than the critical nucleus (Rickard and Luther, 2007). These clusters are concentrated on the surface under the influence of the crystal molecular field, forming a transition layer between the metastable iron sulfide and the bulk solution where nucleation of pyrite is accelerated. Without these metastable iron sulfide minerals, the nucleation of pyrite is kinetically limited, resulting in a long formation period. Direct nucleation of pyrite requires an extremely high supersaturation indexes, e.g. an SI $>10^{14}$ at pH 6.5. With the increasing supersaturation of pyrite in the aqueous solution, pyrite morphology changes in the following order: cube → octahedron → spherulite (Schoonen and Barnes, 1991; Wang and Morse, 1996; Rickard and Luther, 2007).

Increasing total Fe and S concentrations result in a broadening of the pyrite predominance field (Fig. 2.14), mainly in a progressively broader pH axis and downwards to more negative redox potentials on the Eh axis. The lines of equal supersaturation are compressed close to the upper boundary of the pyrite stability field, resulting in an intensive SI-gradient near the SO_4^{2-}/S^{2-} redox boundary zone. Figure 2.14 also shows that pyrite formation is possible even

in natural systems with submicromolar concentrations of sulfides, since its solubility product is so low ($\log_{10} K_{SP}$ = -18.479) (Butler and Rickard, 2000; Rickard and Morse, 2005; Rickard and Luther, 2007).

The full rate equation for pyrite precipitation (Eq. 2.10; Rickard and Luther, 2007) includes both parts of polysulfide and H_2S reaction pathways:

$$\Delta FeS_{2p}/\Delta t = k_{H2S}[FeS]\cdot[H_2S] + k_{Sn(-II)}[FeS]^2\cdot[S^0]\cdot[S^{2-}_{tot}]\cdot[H^+] \quad (2.10)$$

where ΔFeS_{2p} is the rate of pyrite formation in mol/L·s, [FeS] represents the molar concentration of metastable iron sulfides; $[H_2S]$ is the molar concentration of H_2S while the term $[S^0]\cdot[S^{2-}_{tot}]$ describes the molar rate of formation for the generation of polysulfides (Rickard and Morse, 2005). The rate constants k_{H2S} and $k_{Sn(-II)}$ are measured for the Berzelius and Bunsen reaction and noted in Giggenbach (1972) and Rickard (1975).

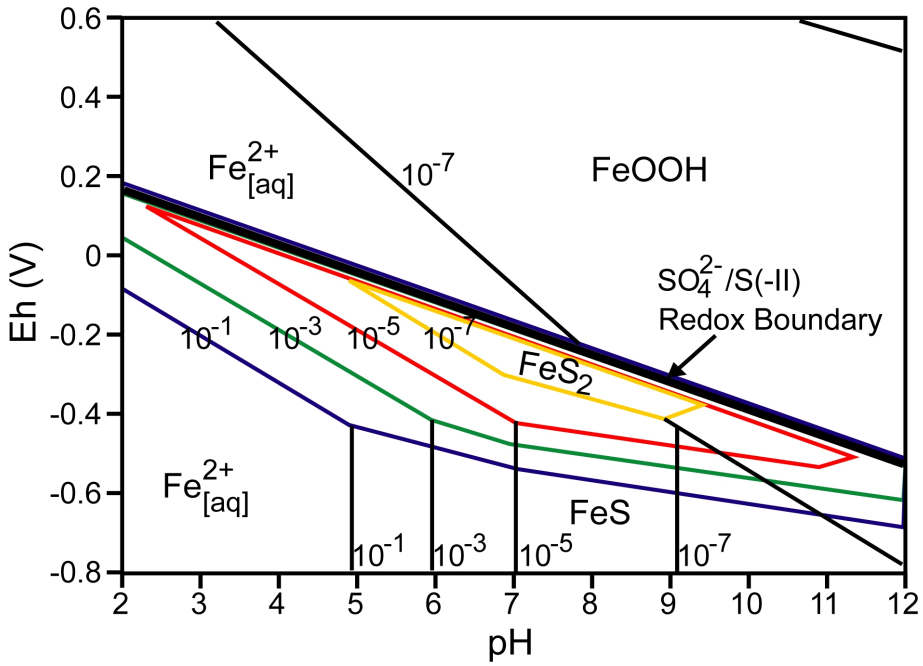

Fig. 2.14: Stability diagram for the system Fe-S-H_20 at 25°C and 1 bar pressure. The contours for the pyrite stability field are drawn in terms of the ion activity potential for pyrite where $\sum a(Fe^{2+}_{(aq)}) = \sum a(S^{2-}_{(aq)})$. The diagram is schematic since the solubility of FeOOH with respect to $\sum Fe^{2+}_{(aq)}$ is variable depending on the nature of the FeOOH phase considered (modified after Rickard and Morse, 2005).

Pyrite formation under high temperature conditions

The synthesis of pyrite single crystals at high temperatures depends on the chosen temperature and the initial amount of sulfur (Fig. 2.15). With a sulfur concentration >53 wt.% and temperatures between 400 and 743°C, pyrite for mation is feasible. At lower sulfur concentrations of 40 – 53 wt.%, mixtures of pyrite and pyrrhotite are obtained. Above a temperature of 743°C, pyrite (FeS_2) decomposes into pyrrhotite ($Fe_{1-x}S$) (Fleet, 2006). According to this Figure 2.15, the synthesis of pure mackinawite single crystals is not possible.

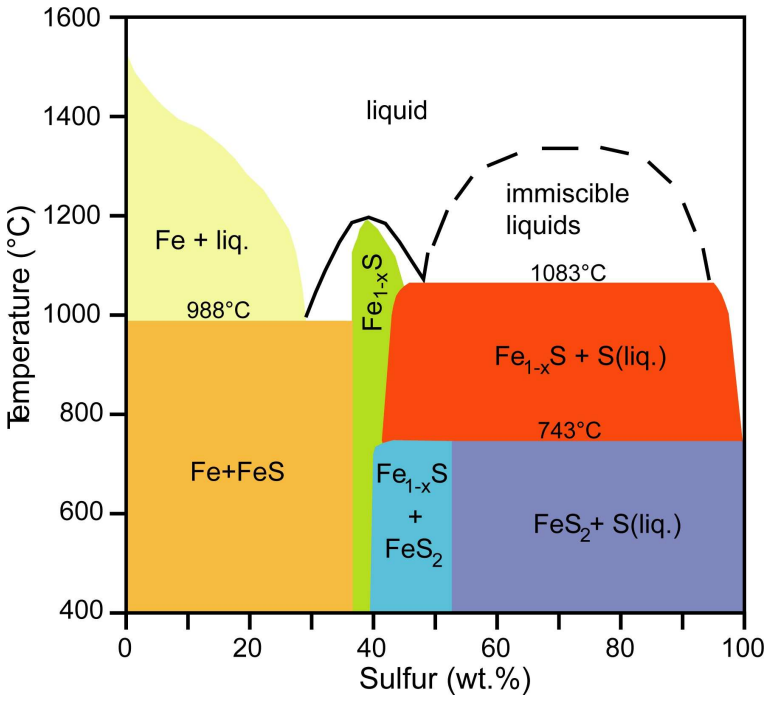

Fig. 2.15: Phase relations in the Fe-S system above 400°C. All phases and phase assemblages coexist with vapor (modified after Fleet, 2006).

With regard to the preparation of selenium doted homogeneous mixed crystals of iron sulfides or selenides at high temperatures, it is malfunctioning by sublimation with pyrite as starting material, because the solids decompose according to the principal reaction (Hotje et al., 2005; Binnewies et al., 2011):

$$FeX_{2(s)}\ (X = S, Se) \rightarrow FeX_{2-n(s)} + X_{2(g)} \qquad (n = 0, \ldots, 1) \qquad (2.11).$$

Instead, a chemical vapor phase transport reaction of the solid after addition of a halogen as transport agent is a feasible way to increase the activity of iron (Tomm et al., 1995). To obtain selenium doted pyrite, the temperature must be hold below the thermal decomposition of the reaction product. The decomposition pressure is given by the equation 2.12 (Binnewies and Mielke, 2002):

$$\lg(p(S_2),K) = -14.93 \cdot 103 \cdot T - 1 - 0.39 \cdot \lg(T) + 15.74 \quad (2.12).$$

For the chosen temperature gradient, the following pressures result: $p(S_2, 600°C) = 3$ mbar, $p(S_2, 700°C) = 170$ mbar and $p(S_2, 752°C) = 1$ bar.

In the first reaction step of the synthesis, the elements react according to equations (2.13) and (2.14):

$$Fe_{(s)} + S_{8(aq)} \rightarrow FeS_{2(aq)} + S_{6(aq)} \quad (2.13).$$

$$Fe_{(s)} + 2\ Se_{(aq)} \rightarrow FeSe_{2(aq)} \quad (2.14).$$

The second step, which leads to the formation of the selenium doted single pyrite crystals, can be explained as partly hydrolysis of the highly reactive solid $AlBr_3$ during the preparation process according to the reaction described in equation 2.15 (Binnewies et al., 2011):

$$2\ AlBr_{3(g)} + 3\ H_2O_{(g)} \leftrightarrows Al_2O_{3(s)} + 6\ HBr_{(g)} \quad (2.15).$$

The chemical transport reaction of solid Al_2O_3 with HCl requires a temperature of about 1300°C (Binnewies et al., 2011). Therefore, it is likely that Al_2O_3 does not disturb the reaction. This finding is in line with the own results of the analysis (Ch. 5.2). The formation of gaseous HBr presumably leads to the transport relevant gas phase reaction (Eq. 2.16):

$$FeX_2\ (X = S, Se)_{(s)} + 2\ HBr_{(g)} \rightarrow FeBr_{2\,(g)} + H_{2\,(g)} + X_{2(g)} \quad (2.16).$$

Bromides of sulfur or selenium (S_2Br_2, SBr_2, etc.) do not exist at the reaction temperature of 700°– 600°C, therefore sulfur or selenium occurs as elements in the gas phase. At lower temperatures, larger sulfur molecules S_x (x = 2, …, 8) might appear (Binnewies et al., 2011).

Following these reaction steps, doted pyrite single crystals with a size of ~5 mm ± 2 mm in diameter are obtained. Examples of successful doting of pyrite by chemical vapor transport

are described for As, Co and Ni (Lehner and Savage, 2008), for Au, Co, Cr (Tomm et al., 1995) and with P (Blenk et al., 1993).

Chapter 3

Methods and experimental details

All samples were stored in a desiccator under anoxic conditions within the glovebox (O_2 <3 ppm), filled with silica gel for an additional prevention of oxidation. For every spectroscopic investigation, only a part of a dried solid sample was used and finally discarded because of probable surface oxidation.

3.1 Analytical methods

Eh- and pH-values were routinely measured during the batch experiments, as well as the temperature of the solution, using a daily calibrated WTW Multi 340i (John Morris Scientific Pty Ltd.) system. The precision of the pH value is ± 0.01; that of the Eh-value is ± 1 mV and that of the temperature ± 1° C.

The potentiostat (Uniscan PG580) in connection with an **electrochemical cell** was used to apply constant potentials in the solutions. This assembling allowed reducing Se^{4+} to Se^{2-} as well as the setting of a constant Eh for Se doted iron sulfide synthesis in batch reactions. The electrochemical cell consists of a glassy carbon working electrode, a platinum auxiliary

electrode, and an Ag/AgCl reference electrode, filled with 3 M KCl. The accuracy of the **potentiostat** is ± 1 mV and its range of Eh-values is -2 – 2 V.

X-ray powder diffraction (XRD) served for mineralogical characterization of precipitated solids. X-ray diffraction patterns were measured using a Siemens Kristalloflex D500 with monochromatic Cu-Kα radiation with 40 kV and 20 mA in a θ – 2θ geometry. The measurements were carried out in angles between 10° to 70° with an increment of 0.02°, by continuous scanning at 0.5° per minute. The minimum detectable mineral content is about 1 wt.%. **Crystallographic identification** on the basis of 2θ–peaks was done with QualX, version 1.2, using the American Mineralogist Crystal Structure Database for the reference peaks.

Scanning electron microscopy (SEM) was additionally used for the identification of minerals using a LEO 1530 SEM at the Laboratory of Electron Microscopy (LEM) at the Karlsruhe Institute of Technology (KIT), Germany, working in conjunction with energy-dispersive X-ray spectroscopy (EDX). The SEM was operated with an acceleration voltage of 10 keV. A maximum resolution of 1 nm was achieved. The selenium concentration in different mineral particles was analyzed by EDX using the excitation energy of 5 keV and a penetration depth of 0.25 µm. The detection limit of Se by EDX was 0.1 wt.%. To avoid surface charging, the samples were carbon coated before the measurements.

Focused ion beam (FIB) allowed preparing a 30 nm thick thin section which was carried out using a focused ion-beam system (FEI Strata 400 STEM) with a 30 keV gallium ion beam mill at the LEM at KIT. The excitation energy of the EDX system was set to 30 keV while mapping the Se concentration within the grains.

Transmission electron microscope (TEM) helped to identify the size and orientation of the microcrystals within the synthetically precipitated pyrites. The 30 nm thick thin section was analyzed with the FEI Titan 80 and the FEI Titan 300 at the LEM at KIT.

Brunauer-Emmett-Teller measurements (BET) for the determination of the specific surface area (in m^2/g) were carried out using a Quantachrome Autosorb 1-MP instrument under

nitrogen atmosphere at the Institute of Functional Interfaces (IFG), KIT, Germany. The accuracy was ± 0.15 %.

Energy dispersive X-ray fluorescence (ED-XRF) was applied for measuring the selenium concentrations of the solids with a PANalytical Epsilon 5 ED-XRF instrument. The calibration standards were specially prepared by mixing elemental selenium with pure quartz powder. Four standards were prepared in logarithmic scale to allow a wide range of Se-measurements: 100 ppm Se, 1000 ppm Se, 10000 ppm Se, 100000 ppm Se. The amount of Se doted iron sulfides samples for measurements was 0.1 – 0.2 g, which was not enough for ED-XRF investigations. For this reason, the samples were also mixed with quartz powder. The average of three measured values was taken. The precision of the solid element detector amounts to an uncertainty of ~5 % and a detection limit of ~1 ppm. The accuracy of the samples was calculated of the prepared standards. The relative standard deviation was 3.2 %.

High-resolution inductively coupled plasma mass spectrometry (HR-ICP-MS) was used to measure the concentrations of selenium and to some extent iron and sulfur in the solutions before and after the synthesis (Axiom, VG Elemental 2, Thermo). The concentrations were calculated as the mean of three measurements from ^{77}Se and ^{82}Se isotopic measurements. The detection limit for Se, Fe, and S is >10 ng/L. The calibration standard for sulfur was CertiPur-sulfur ICP-standard from Merck with a stock solution of 1000 mg/L (± 0.4 %). For iron and selenium, the sulfur-free ICP-multi element standard VI CertiPur from Merck was applied, with stock solutions of 100 ± 5 mg/L each. The accuracy of the measurements was calculated from reference standard Trace Metals - ICP (Promochem, high purity standard), which has been measured after calibration and after the samples. The selenium concentration of the reference standard was 252 µg/L and the relative standard deviation (RSD) amounted to 3.8 %. With regard to the precision of the double-focusing sector field SF-ICP-MS (axiom of VG Elemental), the RSD was calculated of the three measurements of a sample and was always between 1 and 3 %.

Inductively coupled plasma optical emission spectroscopy (ICP-OES) was used initially for the analysis of Fe and S by a Varian 715-ES instrument. Due to the observation that the concentrations within the samples were partially below the detection limit, only the previous one-third of the samples has been measured with ICP-OES. Iron was measured at a wavelength of 238.204 nm and sulfur at 181.972 nm. The reference standards CertiPur (VWR) contained 1 g/L of Fe and S. The detection limit is 1 µg/L for Fe, 13 µg/L for S, and 16 µg/L for Se. The calibration standards used for the measurements were the same as for HR-ICP-MS. The accuracy of the ICP-OES was calculated from the differences of the standards and amounted to a RSD of 3.1 %.

X-ray photoelectron spectroscopy (XPS) analysis was performed to achieve further insight into the valence state of selenium doted pyrite. Samples are prepared onto indium-foil within an inert-gas glove box and transferred without air-contact into the X-ray photoelectron spectrometer located at the Institute for Nuclear Waste Disposal (INE), KIT, Germany. The measurements are carried out in ultra-high vacuum on a PHI model 5600ci (Physical Electronics Inc.) instrument with monochromatic Al Kα X-ray excitation (1486.6 eV). Elemental lines of pure metals (Mg Kα: Cu $2p_{3/2}$ at 932.62 eV, Ag $3d_{5/2}$ at 368.22 eV, Au $4f_{7/2}$ at 83.95 eV) with well-established binding energies are used to calibrate the binding energy scale of the spectrometer (Seah et al., 1998). Narrow scans are measured at 23.5 eV pass energy of the hemispherical analyzer which results in a full width at half maximum of 0.74 eV for the Ag $3d_{5/2}$ elemental line. A shift of elemental lines for charge referencing is not necessary, since the samples are well-conductive.

Error propagations for the concentrations of S, Se and Fe measured with HR-ICP-MS, ICP-OES and ED-XRF have been performed using the following equation (Hillebrand, 2009):

$$\Delta E = \sum_{i=1}^{n} \left| \frac{\delta E}{\delta \chi i} \right| \Delta \chi_i \qquad (3.1).$$

ΔE represents the error of the concentration E which is defined as a function of *n* variables. $F = F(\chi_1, \chi_2, \dots, \chi_n)$ is related to the errors of the variables $\Delta\chi_1, \Delta\chi_2, \dots, \Delta\chi_n$.

Thermodynamic equilibria were calculated with PhreeqC, version 2.17, using the WATEQ4F database (relevant stability constants are listed in Appendix A as well as in Ball and Nordstrom, 2001). The calculations were performed for the same concentrations under standard conditions which were chosen for aqueous solutions, prepared for the syntheses of Se doted iron sulfides. The results of interest were the ionic strength of the solution, the saturation indices of the minerals containing Fe, Se, S or in combination of these elements, the amount of the different dissolved Se-, S- and Fe-species present in the solution before and as residual after the reaction as well as the type of precipitated minerals. Stability diagrams were created to get an overview of the predominant species and phases within the stability field of water. This should allow a general overview of the stability fields of pyrite and selenium.

3.2 Theory and setup of X-ray absorption fine structure (XAFS)

X-ray absorption fine-structure spectroscopy is an element-selective method which provides information about oxidation state, site symmetry, ligand´s identity and coordination number as well as interatomic distances of an element at concentrations in the area of several 100 ppm contents of an element. The basic principle of XAFS is scanning through the surrounding energy of an element with synchrotron radiation while measuring the absorption of incident X-rays as a function of energy (Newville, 2004).

X-rays are radiations with energies ranging from ~500 eV up to 500 keV with corresponding wavelengths from ~25Å to 0.25Å. When the X-ray energy (E) exceeds the binding energy of a core level electron (E_0), the electron can be removed from its quantum level. The energy of the X-ray in an amount of the electronic binding energy is absorbed and given to a photo-electron which ejects from the atom. By reordering the Lambert-Beer law, the absorption coefficient μ can be calculated after (Newville, 2004):

$$\mu(E)\cdot t = \ln \frac{I_0}{I} \qquad (3.2)$$

with *t* as the thickness of the sample, I is the intensity transmitted through the sample and I_0 as the initial x-ray intensity before a sample. In XAFS investigations, monochromatic X-rays from a synchrotron radiation source are directed onto a sample (Fig. 3.1). A synchrotron facility itself consists of a ring of magnets which accelerate a beam of electrons in the radial direction of a circular orbit. In the direction of the tangent, the electron decelerates and loses energy in the form of photons, the so called synchrotron radiation. The most important advantage of this synchrotron beam is its high brilliance, meaning the high-energetic, well focused beam combined with low noise (Dove, 2003).

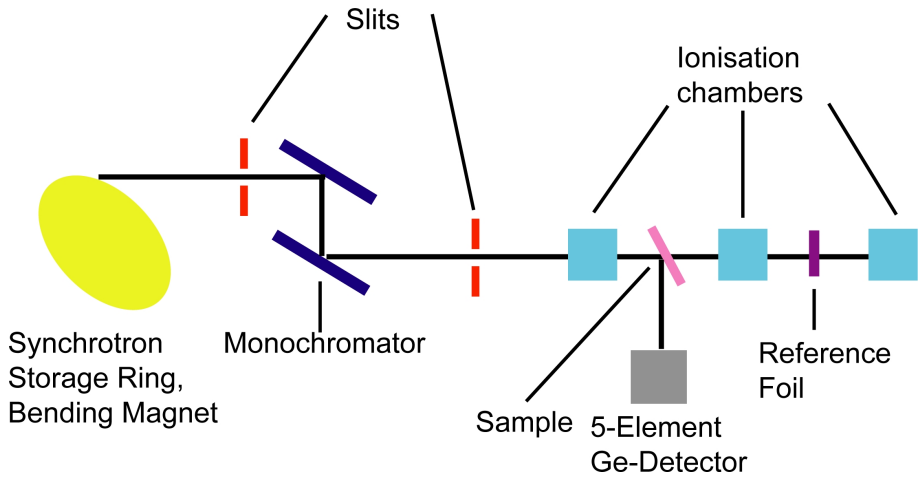

Fig. 3.1: Scheme of the experimental setup for XAFS investigations (modified after Newville, 2004).

In general, the X–ray energy varies by adjusting the Bragg–angle of a double crystal monochromator. In general, if the concentration of the concerning element exceeds low percentages within the sample, the energy dependence of the absorption coefficient μ(E) can be measured in transmission mode by detecting the intensity of the x–rays before (I_0) and after (I) the sample (Newville, 2004):

$$\mu(E) = \log \frac{I_0}{I} \qquad (3.3).$$

The fluorescence mode of the Auger emission is generally more applicable for lower element concentrations. In this case, μ is directly proportional to the quotient I_f/I_0 with I_f being the monitored intensity of the fluorescence (Newville, 2004):

$$\mu(E) \propto \frac{I_f}{I_0} \quad (3.4).$$

As mentioned above, the absorption process leads to the formation of a photo-electron. This travels as a wave which can be calculated as following:

$$\lambda \propto (E\text{-}E_0)^{-0.5} \quad (3.5).$$

λ is the wavenumber of the photo-electron and E_0 represents the bound core electron level, also called absorption edge or the white-line. In the XAFS spectra, the white-line is usually the sharp increasing peak. Hence, the electrons from core or valence level orbitals are excited into higher energy vacant orbitals or the continuum. The absorption close to the energy value of the white-line is the basis of X-ray Absorption Near-Edge Structure spectroscopy (XANES). The XANES spectra provide investigations of the chemical states of particular elements in a mineral, solution, gaseous phase or surface species. It is often used as fingerprint-method, meaning that the curves of the valence states with belonging E_0 value of the absorption edge are always equal for an identical electron configuration of an element. Therefore, since it is not yet possible to predict these white-lines, reference spectra are compared with those of the samples. Close below the edge, there are as well absorption peaks due to excitation of core electrons to some bound states (Fig. 3.2, Newville, 2004; Wincott and Vaughan, 2006; Oelkers et al., 2009).

The photoelectron as described before is a wave which becomes scattered back from neighboring atoms that can interfere either constructively or destructively with the outgoing wave. This interference results in an oscillation of the absorption rate while the amplitude and frequency of this modulation depend on the type and bonding of the neighboring atoms and their distances from the absorber (Fig. 3.2). This occurs at energies above the absorption edge, providing the fine structure spectra used in Extended X-ray Absorption Fine Structure spectroscopy (EXAFS). By fitting a theoretical model to this spectrum, the structural

information about the radial distances, the type and number of neighbored atoms from a selected element can be achieved (Newville, 2004; Wincott and Vaughan, 2006).

Initially, before fitting, the oscillations above the white-line have to be separated from the raw data. Therefore, the EXAFS fine-structure function χ (E) is defined as:

$$\chi(E) = \frac{\mu(E) - \mu_0(E)}{\Delta\mu_0(E)} \tag{3.6}$$

with $\mu_0(E)$ standing for the smooth background function and $\Delta\mu_0(E)$ as the jump edge, calculated from the rising of $\mu(E)$ at the absorption edge E_0. The most accessible way to describe EXAFS is in formalisms of the wave behavior of the photo-electron. Hence, the X-ray energy (E) has to be transformed into k-space with k ($Å^{-1}$) as the wave number of the photo-electron:

$$k = \sqrt{\frac{2m(E-E_0)}{\hbar^2}} \tag{3.7}$$

where m is the electron mass and ħ is the reduced Planck action quantum, written as $\hbar = \frac{h}{2\pi}$.

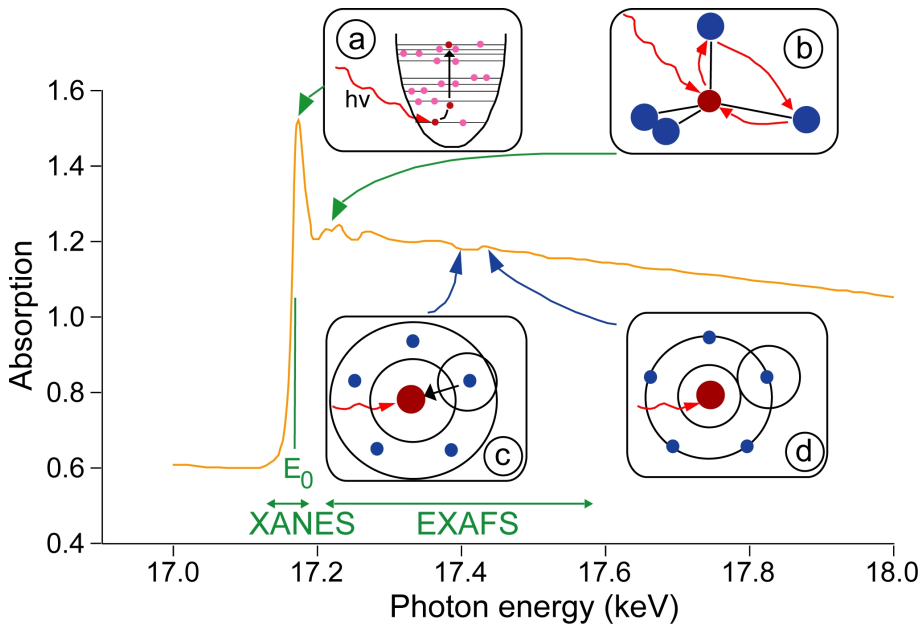

Fig. 3.2: XAS-spectra of the L_{III} edge of uranium in solid $CaUO_4$ (modified from Behrens, 1992; Rothe and Léon, 2008). A) Transition to empty bound state (XANES); B) Multiple scattering region (XANES); C) Destructive interference (EXAFS); D) Constructive interference (EXAFS).

$\chi(k)$ (Eq. 3.8) displays the oscillations as a function of the wave number and is often weighted by a power of *k* to enlarge the oscillations. The different frequencies in the oscillations in $\chi(k)$ belong to different atomic neighbors. The EXAFS formalism finally describes the sum of the contributions from each scattering coordination shell:

$$\chi\,(\mathrm{k}) = \sum_j \frac{N_j S_0^2 f_j(k) e^{-2R_j/\lambda(k)}\, e^{-2k^2\sigma_j^2}}{kR_j{}^2} \sin[2kR_j + \delta_j(k)] \qquad (3.8).$$

The sum $\sum_j$ stands for the scattering paths of the photo-electron, j represents the individual coordination shell of identical atoms at the same spatial distance from the central atom and k, which is equal to $\frac{2\pi}{\lambda}$, is the wavenumber of the emitted photoelectron. If the scattering properties of the neighboring atoms f(*k*) and δ(*k*) are known, both are dependent on the atomic number of the neighboring element as well as the mean-free-path λ(k), it is possible to determine the distance to the neighboring atoms R_j, the coordination numbers of the neighboring atoms N_j and the mean-square disorder of neighbor distances σ^2. Finally, S_0^2 stands for the amplitude reduction factor, describing the effects of multi-electron excitations accompanying the photo-effect in the inner shell (Newville, 2004).

The XAFS investigations described in this study have all been conducted at the synchrotron light source Ångströmquelle Karlsruhe (ANKA) at Karlsruhe Institute of Technology (KIT). ANKA is composed of an injector where the beam energy is accelerated from 70 keV by an electron gun to 53 MeV at the racetrack microtron to 500 MeV in the booster synchrotron. ANKA is finally operating with an energy of 2.5 GeV in the storage ring, at a beam current of 200 mA with an emittance of 50 nm·rad. There are three straight sections equipped with insertion devices (wiggler W74, undulator U10, undulator SCU14). The lifetime of the beam amounts to ~12 h within the circumference of the storage ring of 110.4 m (ANKA, 2010).

To determine the atomic environment of Se by XAFS measurements, six to nine line scans of iron sulfide samples and references were performed using the INE, XAS and SUL-X beamlines of the ANKA synchrotron radiation facility (Fig. 3.1). XAS (possible energy range E: 2.4 – 27 keV) and INE beamline (E: 2.1 – 25 keV; spot size: ~1 mm^2) use a solid-state

five-element Ge detector while their insertion device is a dipole magnet. SUL-X beamline (E: 1.5 – 20 keV; µ-focus: ~10 μm^2) consists of a 7 element SiLi-detector with a wiggler as insertion device.

For solid sample preparation, manually milled iron sulfides were mounted on samples holders of Plexiglas with housings of 1 cm in diameter and 1 mm in depth, covered by Kapton foil. Liquid samples of dissolved Se^{2-} and Se^{4+} species were stored in plastic flasks within the glovebox until measured. The samples were analyzed in the fluorescence mode in the typical energy range of Se surroundings (12.5 – 13.5 keV). The XANES range was scanned from 12600 eV in front of the absorption edge to 12700 eV above the absorption edge in steps of 0.42 eV and the EXAFS range until k = 15. While measuring the samples, spectra of a metallic Se-foil with a known k-edge value (12658 eV) were recorded as the reference for energy calibration.

The energy of the absorption edge of an element can reveal the oxidation state, while the shape of the normalized intensity of the white line is related to the molecular structure and can, therefore, be used for the identification of selenium by comparison with known standards. Since the XANES spectra of a compound is a unique fingerprint, the valence states of the selenium doted iron sulfide samples could be identified by comparison with the XANES spectra of some reference compounds ranging in oxidation state from IV to –II. As references for a comparison of XAFS spectra, compounds of reagent grade were applied, such as dissolved and solid Na_2Se (Alfa Aesar), grey, trigonal Se^0 (Merck), dissolved and solid Na_2SeO_3 (Merck), achavalite (Alfa Aesar), and ferroselite (Excalibur minerals). This is highly important, because the valence state of selenium gives a strong hint about whether selenium was structurally fixed or not and which type of neighbors can be expected.

With regard to XAFS investigations of selenium standards, the own results of the absorption edge at the peak of the white line (E_0) and/or structural analysis like the coordination number (CN) or the atomic distance from the selenium absorber to an atomic neighbor (R), were compared with some publications (Ryser et al, 2005; Charlet et al., 2007; Breynaert et al.,

2008; Scheinost et al., 2008). The XANES spectra of the cited studies are listed in Appendix B.

The curves in the k-space display the EXAFS spectra, while the Radial Structure–Function (RSF) shows the Fourier-transformed EXAFS spectra. The q-space are the theoretical fits of the EXAFS-spectra, which display the accordance with the EXAFS-spectra and also the range of fitting. Since there were no technical problems, the detectable amount of selenium was the limiting factor of a good signal to noise-ratio. Next to the XANES spectra, the EXAFS spectra also show differences between the selenium valence states, which is related to the different nature and radial distribution of the backscattering atoms around the central adsorbing selenium atom.

Energy calibration and averaging of line scans for each sample were performed with the software Artemis 0.8.014, while shell fitting was accomplished using Athena 0.8.061 (Ravel, 2009). Both are part of the IFEFFIT package (Newville, 2001).

For the interpretation of EXAFS spectra, the amplitude factor (S_0^2) was always between 0.7 and 1.0. The deviation of radial atomic distance (ΔR) was allowed to vary during the fit, but it was not to exceed ± 0.1 Å. Finally, it was added or substituted, based on initial guess. Shift of energy (ΔE_0) should not exceed 10 eV. It was valid for all shells and was allowed to change during the fitting process as was the coordination number (CN). Finally, the Debye-Waller factor (σ^2) of each shell had to range between 0.001 and 0.015 and the residual of fit (R-factor) should remain below 0.01. The values of these variables were defined in accordance to typical ranges for EXAFS interpretation (e.g. Kelly, 2009).

Chapter 4

Developed synthesis of selenium doted pyrite and mackinawite

Three different ways of selenium doted iron sulfides as solid solutions were developed. In batch reactions, selenium was incorporated into pyrite and mackinawite by spontaneous precipitation. This synthesis of Se doted iron sulfides covers the whole process of pyrite formation, starting from its rate-limiting nucleation of pyrite to crystal growth up to an average size of 1.5 µm in diameter (Diener and Neumann, 2011). But direct nucleation and formation of pyrite under ambient conditions does mostly not occur without a precursor phase. In this regard, mackinawite is by far the most important mineral because its formation is kinetically extremely rapid with less than 1 s, as it was measured during synthetical pyrite formation. This metastable precursor phase dissolves and finally reacts with dissolved sulfur species, resulting in precipitation of pyrite (Rickard and Luther, 2007).

Another way to incorporate selenium into pyrite is by using natural pyrite as nuclei for the further crystal growth, as it has been performed in a mixed flow reactor. This type of experiment reflects only crystal growth on persisting pyrite (Diener et al., 2012).

Finally, a high temperature synthesis of selenium doted pyrite was developed, using solid zero-valent Fe, S and Se, as base materials for a two-step chemical vapor transport reaction in a 2-zone furnace with a gradient of 700°C to 600°C. Under these conditions, sublimation of the initial reactants is taking place in a first step followed by condensation of solid matter at the cooler side of the reaction vessel. This type of synthesis may be a good option to simulate hydrothermal conditions for selenium doted pyrite formation (Diener and Köppe, 2012).

Additionally, pyrite crystal synthesis by diffusion through silica gel (Wang and Morse, 1996) using mackinawite nuclei was tried for different runs lasting for 3, 6 up to 9 months. Silica gel was produced by addition of 100 ml 0.75 M Na_2SiO_3 to 100 ml 1.5 M CH_3COOH, crystallizing within 1 hour from this solution after addition of sufficient HCl until a pH of 5 was reached, while 0.7 g of synthesized mackinawite nuclei were added to the silica gel under stirring. 50 ml of this prepared matrix were filled into petri dishes and covered with different solutions of 10 – 20 ml each of 0.1 M NaHS and 10^{-3} M Na_2Se. Only once, a further development of mackinawite to greigite (Fe_3S_4) was observed, but in no cases the formation of pyrite.

4.1 Spontaneous precipitation and nucleation of Se doted pyrite and mackinawite

The objective of the batch reaction synthesis for this type of experiments was to produce pyrite solid matter by wet chemical precipitation. A few studies have already been carried out reporting of pure pyrite aqueous syntheses under standard conditions in the literature (Tab. 4.1). These differed with regard to iron (Mohr´s salt, iron chlorides, iron sulfates, iron nitrates, iron-oxyhydoxides or iron monosulfides) and sulfur reactants which were used (hydrogen sulfide, sodium (hydrogen-) sulfides, long-chained sulfur phases), the pH range for the syntheses (3.6 – 8.0) and the duration of the reaction (2 d – 1 a). The experimental systems used were of the batch reactor type while the reactant concentrations were in the millimolar to molar range. In all cases, the saturation index of mackinawite was exceeded,

resulting in the initial formation of this precursor phase. The published pH was the final pH in most cases, which was normally reached within a few hours (Rickard and Luther, 2007). Concerning the synthesis of pyrite in aqueous media, there are publications apart from those mentioned in Table 4.1 (Schoonen and Barnes, 1991; Ohfuji and Rickard, 2005; Rickard and Luther, 2007). In the publications which were not listed, iron sulfide phases precipitating additionally to pyrite have been detected or higher solution temperatures were chosen for the pyrite synthesis were chosen.

Tab. 4.1: Pure pyrite syntheses reported for aqueous solutions at 25°C and 1 bar pressure.

Fe source	S source	pH	Duration	Reference
FeO(OH)	**H_2S**	**3.8 - 6.0**	**26 d**	**Roberts et al., 1969**
$FeSO_4$	**H_2S**	**7.0 - 8.0**	**~1 a**	**Farrand, 1970**
Fe(II)-salts	**Na_2S_n**	**5.5 - 8.0**	**>4 m**	**Luther, 1991**
$FeCl_3$	**NaHS**	**3.6 - 5.7**	**5 d**	**Wei and Osseo-Asare, 1996**
$FeCl_2$	**NaHS, Na_2S_n**	**3.6, 6.5**	**2 d, 9 d**	**Wei and Osseo-Asare, 1997**

Since most of the experiments take several months up to a year, it was most practical to perform pyrite syntheses with a short reaction time. Hence, the reported synthesis from Wei and Osseo-Asare (1996) was chosen for the experiments due to the rapid kinetics of pure pyrite formation. The starting solutions consist of 0.1 M $FeCl_3 \cdot 6H_2O$ in deoxygenated MilliQ water containing 0.01 M HCl to prevent oxidation of iron and 0.1 M $NaHS \cdot xH_2O$ in deoxygenated water, followed by mixing these solutions. The redox reaction between Fe^{3+} and S^{2-} ions leads to the formation of Fe^{2+}, HS^- and S° species (Eq. 4.1 and 4.2):

$$2\ Fe^{3+} + S^{2-} \rightarrow Fe^{2+} + S^0 \quad (4.1)$$

$$Fe^{3+} + S^{2-} + H_2O \rightarrow Fe^{2+} + HS^- + OH^- \quad (4.2)$$

With regard to the feasible reaction paths for pyrite formation, the mixed solution contains both, hydrogen sulfide as well as polysulfides from the S° intermediate product. Due to this composition, it is very likely that the formation of pyrite under these hydrochemical conditions (Tab. 4.1) follows both, the H_2S as well as the polysulfide pathway (Eq. 2.8 and Eq. 2.9).

Pyrite synthesized by this procedure contains also elemental sulfur, which could be removed by solvent extraction using CS_2 in a Soxhlet apparatus (Roberts et al., 1969; Wei and Osseo-Asare, 1996).

Wei and Osseo-Asare (1996) describe their produced precipitations as spheroidal particles with a pyrite content of 99.46 %, a mean diameter of ~1.5 µm, formed in the pH range of 3.6 – 5.7 at Eh values between -0.05 and 0.01 V. The intermediate products of elemental sulfur and FeS or $Fe(HS)^+$ were necessary precursors for pyrite formation, which are both thermodynamically stable under the described aqueous conditions. Pyrite does not precipitate below pH ~3.6. Because of the preferential stability of Fe^{2+}, the solution would be undersaturated with regard to the necessary pyrite precursor species FeS or $Fe(HS)^+$, On the other side, the inhibition of pyrite formation above pH ~5.7 is due to hydrochemical conditions with FeS being unstable in comparison to FeOOH. Furthermore, the pyrite formation experiments were restricted to acidic solutions because the solubility of the important mackinawite precursor phase is comparatively low at circumneutral to alkaline conditions (Schoonen and Barnes, 1991; Wei and Osseo-Asare, 1996, Wei and Osseo-Asare, 1997).

Synthesis of selenium doted pyrite

The synthesis of Se doted pyrite were carried out under anaerobic conditions in a glovebox with an oxygen content of less than 3 ppm (Fig. 4.1). The dissolved oxygen was purged out of all liquids before usage for one hour using a vacuum pump. All chemicals used for iron sulfide synthesis were of reagent grade.

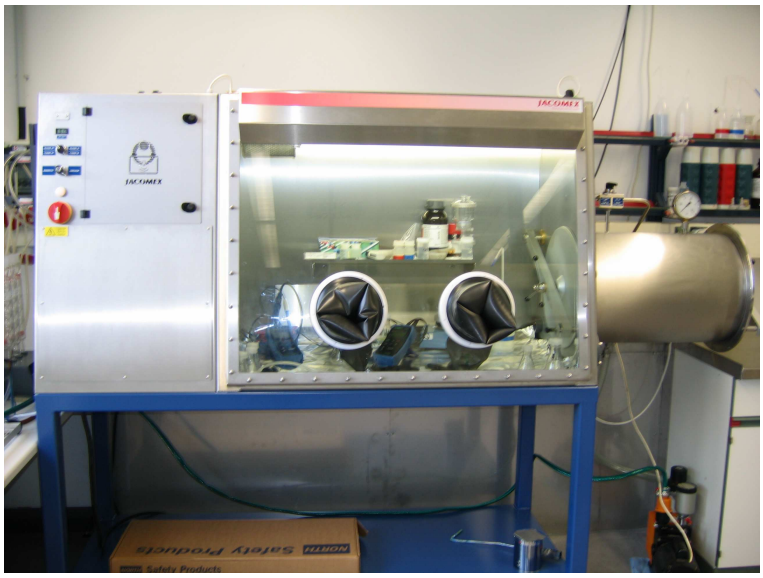

Fig. 4.1: Jacomex glovebox.

The electrochemical reduction of Se^{4+} to Se^{2-} occurred in an electrochemical cell controlled by electronic hardware, the potentiostat (Fig. 4.2.; Lingane, 1948; Liu et al., 2008). The electrochemical cell consists of three electrons and its basic principle is to keep the potential of the working electrode (WE) at a constant level in an electric circuit with regard to the counter electrode (CE), together forming a half cell. The reference electrode (RE) is placed between those two electrodes and measures the difference of the potential between the WE and CE. Furthermore, the RE observes the current within a solution containing a necessary electrolyte (e.g. NaCl, NH_4Cl) (Plieth, 2008).

The preparation of selenide was carried out at a potential of -1.5 V. To avoid hydrolysis, the glassy carbon electrode was dotted with mercury. Therefore, 0.17 g of $HgNO_3$ in a 100 ml 1 M NH_4Cl solution was kept at a potential of -0.8 V (with respect to SHE) for one minute. This was carried out two more times with one hour intervals. Then, the desired amount of selenium was introduced as Na_2SeO_3 in a 100 ml 0.1 M NaCl solution and reduced for 3 hours by applying a potential of -1.5 V. Finally, a Se^{2-} solution of $1 \cdot 10^{-3}$ mol/L could be obtained within three hours. To confirm the effect of this preparation, a potential of +50 mV was applied to the selenide solution outside of the glovebox. The rapid oxidation of selenide resulted in the precipitation of elemental selenium within minutes. Alternatively, commercially

available selenide in the form of Na_2Se can be used, which simplifies the incorporation procedure, but it was not always available.

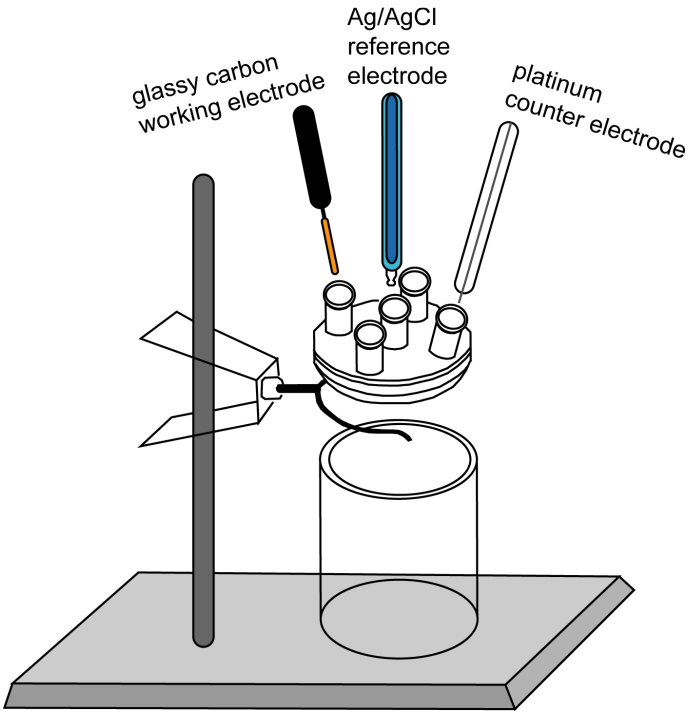

Fig. 4.2: Scheme of the electrochemical cell.

Next, the solutions of 0.066 M NaHS, 0.0175 M $FeCl_3 \cdot 6H_2O$ and varying Na_2Se or Na_2SeO_3 concentrations from $1 \cdot 10^{-6}$ M up to $1 \cdot 10^{-3}$ M with the desired valence states Se^{2-} or Se^{4+}, were mixed. The range for the solution pH was 3.6 – 5.7 and the solution potential was kept constant by the potentiostat and the electrochemical cell at Eh -0.1 – 0.05 V for selenide and Eh 0.05 – 0.1 V for selenite. The exothermic reaction of selenium doted iron sulfide precipitation took place immediately, leading to the formation of black solid particles and a raise in the water temperature of ~1°C for 2 – 3 hours. To adjust the pH, droplets of 1 M NaOH or 1 M HCl were added to the solution. Buffering with sodium acetate ($Na(CH_3COOH)$) in batch systems was proven as unsuitable, since either the buffer itself reacted with the Fe and S reactants and inhibited the precipitation or the buffer capability was exceeded. This observation was also confirmed by Rickard and Luther (2007). The pH-

value was checked and adjusted twice daily; the potential of the solution was maintained between -200 and 100 mV, using a potentiostat.

After 100 h, the solution was decanted. To avoid further precipitation in the residual solution, 100 µl of double distilled 60% HNO_3 was added to 10 ml of the decanted solution. Samples were stored in plastic flasks in the glovebox until further analyses (ICP-MS analysis for selenium concentrations and ICP-OES for iron and sulfur). The precipitated solids were washed with MilliQ several times to remove residual NaCl and again with acetone to eliminate any iron oxyhydroxide coatings on the particles. The solid samples were dried in a desiccator placed in the glovebox. Results obtained via SEM analyses reveal that pure dispersed spheroidal pyrite grains with a mean diameter of 1 – 2 µm were synthesized. The SEM combined with an EDX-system show precipitated Se^{2-} doted pyrite after the reaction of $FeCl_3$, Na_2SeO_3 or Na_2Se and NaHS (Fig. 4.3).

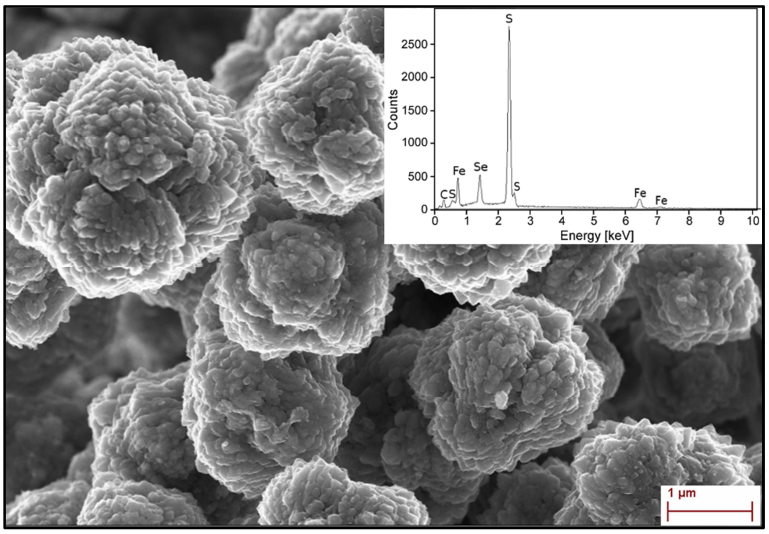

Fig. 4.3: SEM image of spheroidal selenide doted pyrite particles and its EDX spectra.

Because the precipitated solids consisted of a mixture of elemental sulfur and pyrite, they were purified in a Soxhlet apparatus by extracting the elemental sulfur with carbon disulfide as solvent. About 0.3 g of solid was purified by 50 ml CS_2 within 2 hours at 50°C. This procedure was performed under an extractor hood while the Soxhlet apparatus was flooded

continuously with nitrogen. After returning the residual solid into the glovebox, the procedure of cleaning with MilliQ and acetone was repeated. All samples were dried and stored in a desiccator under anoxic conditions within the glove box, filled with silica gel for additional prevention of oxidation from air moisture. Before measurements, it is necessary to remove possible coatings on the solids with acetone again. For every spectroscopic investigation, only a part of a sample was used and finally discarded because of probable mineral surface oxidation. The most important aspects for the synthesis of Se doted pyrite by batch reaction are shown in Figure 4.4.

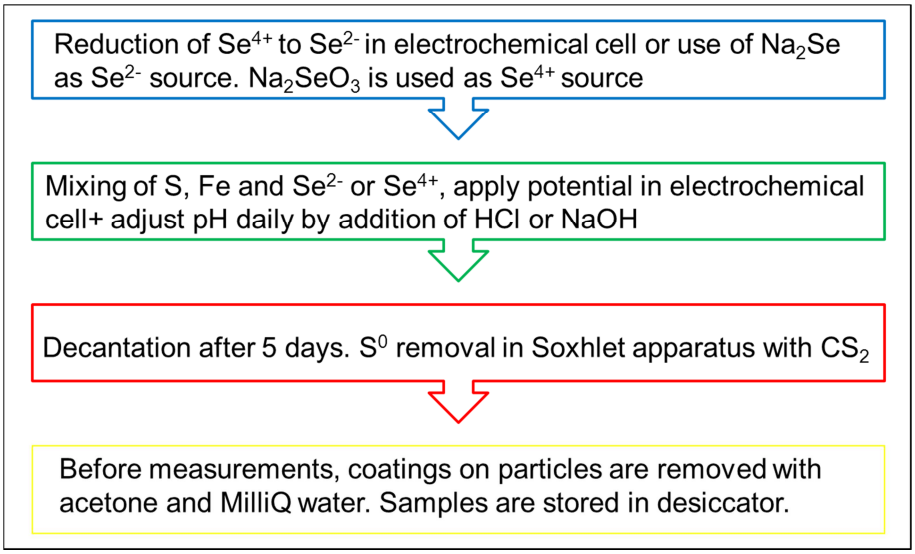

Fig. 4.4: Scheme of the synthesis of selenium doted pyrite.

Synthesis of selenium doted mackinawite

The synthesis of selenide and selenite doted mackinawite was carried out in a glovebox with less than 3 ppm oxygen under a room temperature of 25°C and 1 bar atmospheric pressure. (Tab. 4.2). In all reported studies, Na_2S was selected as sulfur reactant. With respect to iron sources, elemental iron, iron dichloride or iron ammonium sulfate was used.

Tab. 4.2: Pure mackinawite syntheses reported for aqueous solutions at 25°C and 1 bar pressure (n.m.: not me ntioned).

Fe source	S source	pH	Duration	Reference
$Fe(NH_4)_2(SO_4)_2$	Na_2S	n.m	n.m	Arakaki and Morse, 1993
$FeCl_2$	Na_2S	7	4d	Wang and Morse, 1996
Fe^0	Na_2S	6.5	1d	Lennie et al., 1997
$FeCl_2$; $FeSO_4$	Na_2S	n.m	<12 d	Bourdoiseau et al., 2008

Compared to other laboratory syntheses of mackinawite, the advantage of the chosen method after Drobner et al. (1990) and Wang and Morse (1996) is the higher crystallinity of the obtained mackinawite. Following Wang and Morse (1996), the pH-value in the solution was adjusted to. At this pH, equal amounts of H_2S and HS^- are present in the solution (Ch. 2.3.4) and both possible reaction paths lead to the precipitation of mackinawite (Eq. 2.4 and Eq. 2.5).

The solution for the synthesis of selenium doted mackinawite consisted of 0.16 M Na_2S, 0.137 M $FeCl_2$, and $9.1 \cdot 10^{-5}$ M of Na_2Se for Se^{2-}-doting or Na_2SeO_3 as Se^{4+}-source. The solution was adjusted to pH 7 and at an Eh-value of -0.2 V for Se^{2-} or at an Eh-value of +0.1 V for Se^{4+} in the deoxygenized solution. The whole solution was set aside for a period of four days and decanted. Finally, the precipitated mackinawite was washed with deoxygenized MilliQ for several times to remove residual NaCl at the mineral surface and also with acetone to eliminate coatings of the mackinawite particles. The samples were dried in a desiccator, placed in the glovebox until analysis. The precipitated particles had diameters between 20 and 100 µm (Fig. 4.5).

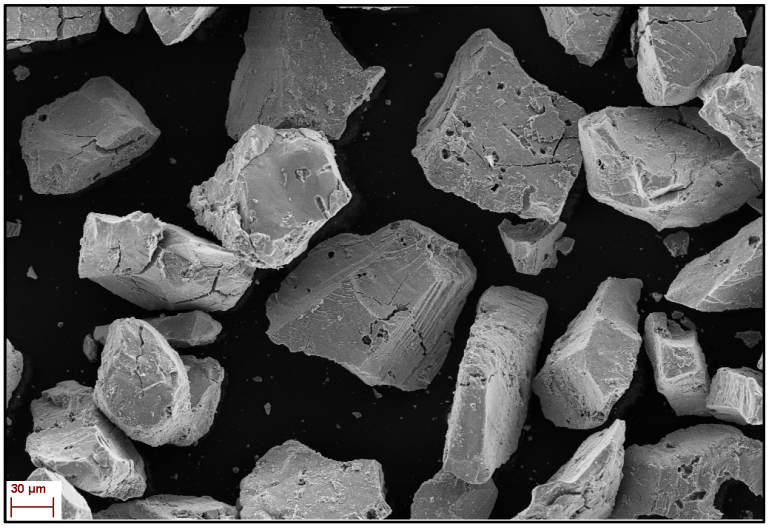

Fig. 4.5: SEM image of selenium doted mackinawite.

In some batch experiments it occurred that the synthesis of Se^{2-} doted pyrite was the aim but pure Se^{2-} doted mackinawite did precipitate. These initial solutions contained $5.5 \cdot 10^{-2}$ – $6.6 \cdot 10^{-2}$ M S^{2-}, $1.6 \cdot 10^{-2}$ – $3.3 \cdot 10^{-2}$ M Fe^{3+}, and $9.1 \cdot 10^{-7}$ – 10^{-3} M of Se^{2-} (experiments with the runs 3 – 10; Tab. 5.7). Therefore, mackinawite precipitated where the formation of pyrite was kinetically hindered, for example at stronger reduced acidic (pH 3.5 and pH 4.5 with Eh between -250 – -300 mV) or slighter reduced acidic conditions (pH 5.1 - 5.8 with Eh between -100 – -200 mV).

4.2 Crystal growth of selenium doted pyrite on natural pyrite nuclei

Further coprecipitation experiments were accomplished in a mixed flow reactor (MFR) with a slightly supersaturated solution (Fig. 4.6). This type of experiment, to simulate pyrite crystal growth with an MFR, has not been reported before. The MFR consists of three solution entries, a magnetic stirring bar for the continuous mixing of the pumped solutions while a ceramic filter is placed in front of the outgoing solution. To avoid grinding effects, the reactor walls are protected by Teflon.

To synthesize selenium doted pyrite, three solutions of $6 \cdot 10^{-3}$ M NaHS, $3 \cdot 10^{-3}$ M $FeCl_3 \cdot 6H_2O$, and $2.5 \cdot 10^{-4}$ M Na_2Se for Se^{2-} or Na_2SeO_3 for Se^{4+}, respectively, were injected into the 90 ml

reactor under continuous stirring of ~700 rpm by a magnetic bar. Prior to this, 0.5 g of ground natural pyrite (containing 2 ppm Se) were inserted into the MFR as nuclei for further pyrite growth. The iron and sulfur solutions were stored in 200 ml test glasses, whereas 100 ml of the selenide solution were kept at a constant Eh value of -300 mV by a potentiostat. For dissolved selenite, the potential was steady at 50 mV.

This solution composition was chosen for the MFR-experiments, because mackinawite is undersaturated (SI = -0.69), while pyrite should precipitate (SI = 7.80) (Ch. 5.1). Under these conditions, enough selenium doted pyrite was expected to grow on persisting natural pyrite nuclei for reasonable mineralogical and structural investigations, to obtain a good signal to noise-ratio far above the different detection limits of the measuring instruments (e.g. XAFS).

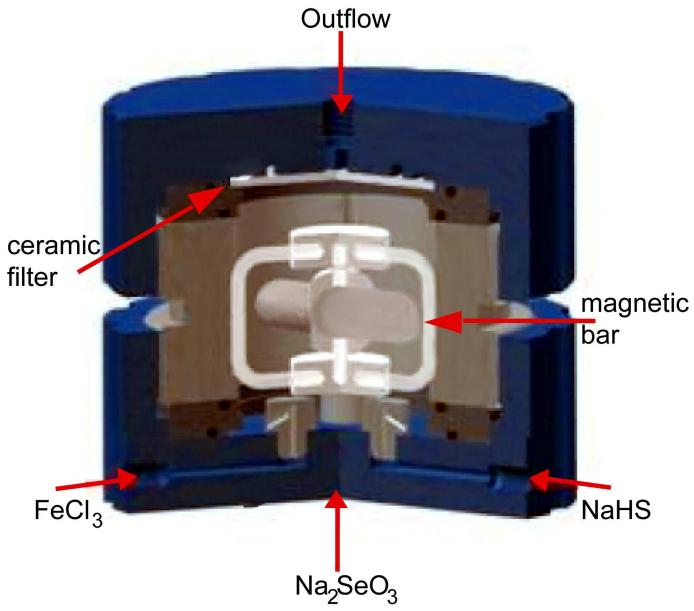

Fig. 4.6: Scheme of the mixed flow reactor (modified after Heberling, 2010).

The Ismatec ISM 915 was used as pump drive for the continuous flow of the solutions into the MFR. The inner diameter of each tube is 0.76 mm and the resulting flow velocity into the reactor was 5.7 ml/h. An exchange of the entire solution in the reactor takes 15.8 h. The syntheses performed by MFR experiments lasted for 120 h. The total amount of solution running through the MFR is 228 ml each.

The precipitated matter was washed with deoxygenized MilliQ for several times to remove residual NaCl at the mineral surface. Afterwards, the samples were dried in a desiccator, which was placed in the glovebox until analysis. SEM images show coatings on totally covered, aggregated, natural pyrite grain and the corresponding EDX spectra exhibit significant Se peaks (Fig. 4.7).

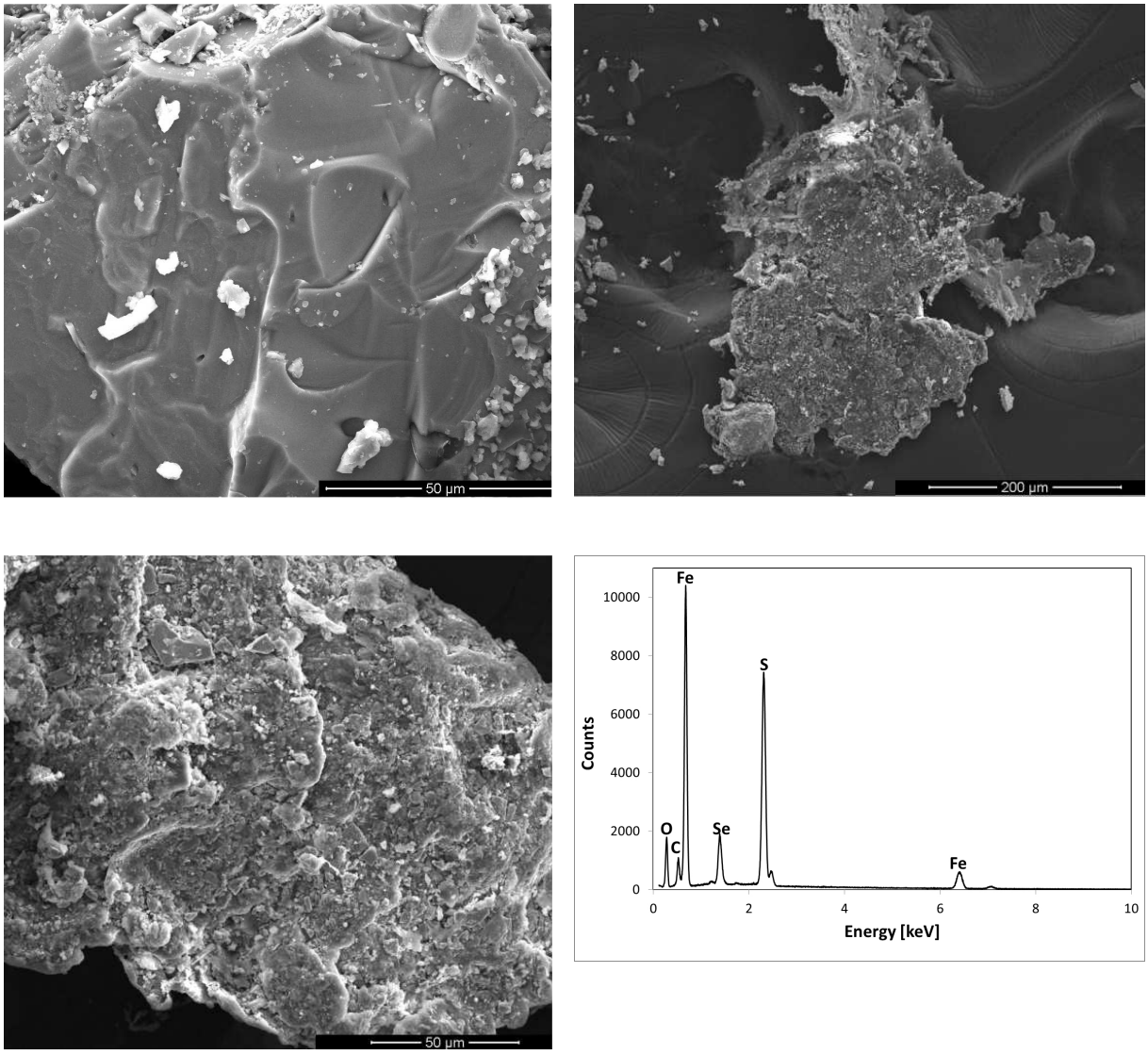

Fig. 4.7: SEM images of selenide doted pyrite from MFR-experiments showing: upper left: initially used, grounded natural pyrite grains; upper right: coatings on totally covered, aggregated natural pyrite grains; down left: close-up view of the coatings; and down right: EDX-spectra of down left.

4.3 Synthesis of selenium doted pyrite by condensation from gaseous phase

The different studies dealing with pyrite formation by chemical vapor transport preferably use chlorine or bromine as transport agent to increase the transport rate of iron, which allow an average transport rate of pyrite formation of ~6 mg/h (Tab. 4.3; Bouchard, 1968; Fiechter et al., 1986; Willeke et al., 1992; Blenk et al., 1993; Tomm et al., 1995). The sulfur source was in all cases elemental sulfur, while as iron source mainly elemental iron was taken, but also natural pyrite or mackinawite. In former studies, a gradient of 100°C within the reaction vessel has proven to be successful (Fiechter et al., 1986). As well, high temperature gradients of 750°C (Blenk et al., 1993) or low gra dients of 20°C (Tomm et al., 1995) lead to the precipitation of single-crystal pyrite. In general, the lower the temperature gradient and the higher the reaction time, the bigger the resulting single-crystals (Tomm et al., 1995).

Tab. 4.3: Pyrite syntheses reported for chemical vapor transport reaction at 1 bar pressure.

Fe source	S source	Agent	Temp. (℃)	Duration	Reference
Pyrite	**S^0**	**Cl_2**	**715-655**	**11-16d**	**Bouchard, 1968**
Fe^0	**S^0**	**I_2, Br_2, Cl_2**	**647-547**	**5-10d**	**Fiechter et al., 1986**
Fe^0	**S^0**	**Br_2**	**1050-300**	**21d**	**Blenk et al., 1993**
FeS, Fe^0	**S^0**	**Br_2, Cl_2**	**630-580; 680-700**	**10-18d**	**Tomm et al., 1995**
Pyrite	**S^0**	**I_2, Br_2, Cl_2**	**743-623**	**14d**	**Etzel, 2008**

The synthesis of Se doted pyrite took place in two reaction steps. Firstly, 0.419 g Fe^0 ($7.5 \cdot 10^{-3}$ Mol), 0.433 g S^0 ($1.35 \cdot 10^{-2}$ Mol), 0.118 g Se^0 ($1.5 \cdot 10^{-3}$ Mol) and 0.04 g $AlBr_3$ as transporting agent, all of reagent grade, were placed in a dry quartz tube (diameter: 1.6 cm, length 10 – 15 cm). After the vessel was evacuated to a pressure of ~10^{-3} mbar, the tube was sealed by welding and placed in a high temperature 2-zone furnace (Fig. 4.8). The range for the starting temperature is limited since pyrite decomposes above 743°C into pyrrhotite while the boiling point of Se^0 is 685°C. Hence, the starting temperature was set to 700°C.

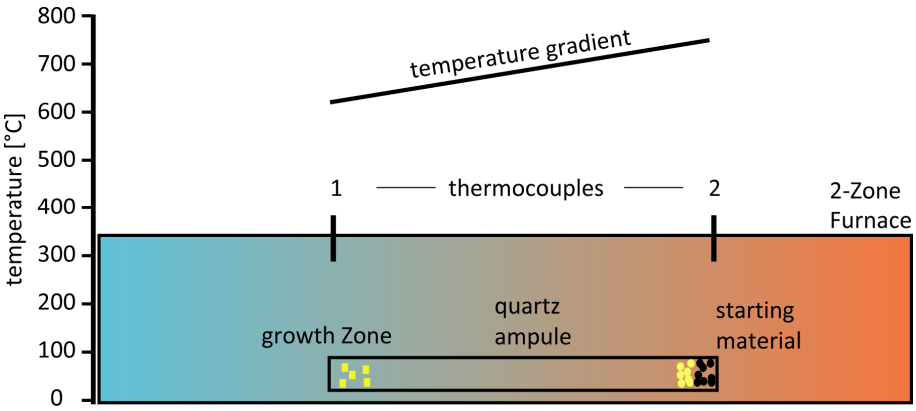

Fig. 4.8: Scheme of the chemical vapor transport in a 2-zone furnace (modified after Etzel, 2008).

The temperature was slowly increased to 600°C with in one day to allow the elements to react and to avoid the complete vaporization of sulfur and selenium which might lead to the explosion of the sealed tube. Afterwards, as first reaction step, the temperature gradient was set from 700°C at the educt side to 600°C at the product side. The condensed matter precipitated as a reddish, amorphous solid. In the second reaction step, the temperature gradient was reversed, from 700°C at the product side of the amorphous precipitation to 600°C at the formerly educt side. At the low temperature side of the quartz tube, selenium doted pyrite precipitated within 14 days. The samples were stored in the glovebox until analysis. The solid/gas phase reaction itself is described by the following equation 4.3 (Binnewies et al., 1977):

$$FeHal_{2(g} \text{ (Hal = Cl, Br)} + X_{2(g)} \text{ (X = S, Se)} \rightarrow FeX_{2(s)} + Hal_{2(g)} \qquad (4.3).$$

The gaseous iron-halogene compound reacts with gaseous S_2 and Se_2, leading to the precipitation of selenium doted pyrite. The single crystals of selenium doted pyrite have a size of 3 – 5 mm in diameter with well pronounced crystal faces (Fig. 4.9).

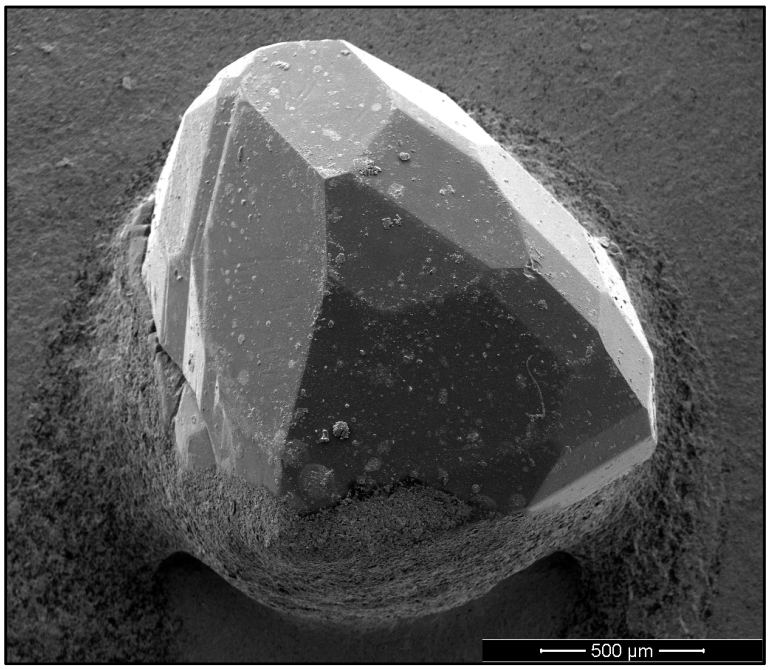

Fig. 4.9: SEM image of selenium doted pyrite from CVT-experiment.

Chapter 5

Results and discussion

The motivation behind this study was to obtain structural information of selenium doted iron sulfides which have been synthesized at defined hydrochemical conditions, reflecting both, formation by nucleation and limited crystal growth or further crystal growth on persisting pyrite in aqueous solution. The type of Se-bonding in pyrite is important, because the stability of fixed selenium is supposably higher in a real solid solution accompanied with a Se bonding with Fe and/or S. Consequently, it is important to know, if the often proposed formation of FeS_xSe_y-compounds or the incorporation of elemental selenium into pyrite structure takes place under defined conditions. Therefore, the stabilities for detected solid solutions were compared with calculated stabilities of possibly precipitating phases, calculated from thermodynamic data, which allow a general overview about the predicted phases for the whole pH-Eh range for a solution.

5.1 Thermodynamic predominance of the aqueous species and phases

The thermodynamic calculations using PhreeqC were performed for the same concentrations under standard conditions which were chosen for the aqueous solutions prepared for the syntheses of selenium doted iron sulfides in batch and MFR-experiments.

A simple FeSSe solid solution mineral with a stoichiometry of 1:1:1, consisting of an equal mixture of pyrite and ferroselite, was added to the WATEQ4F-database to determine its saturation index and possible precipitation. The equation for its formation is:

$$FeSSe + 2H^+ + 2e^- \leftrightarrows Fe^{2+} + HSe^- + HS^- \quad (5.1)$$

The FeSSe-solubility product ($\log_{10} K_{SP}$ = -18.5295) was calculated by addition of pyrite ($\log_{10} K_{SP}$ = -18.479) and ferroselite ($\log_{10} K_{SP}$ = -18.580) solubility products, divided by two. Due to the lack of thermodynamic data of achavalite in the database, the $\log_{10} K_{SP}$ = -26.0 was added, taken from literature (Masscheleyn et al., 1990). The reaction pathway is described as selenium analog to mackinawite (Eq. 5.2):

$$FeSe + H^+ \leftrightarrows Fe^{2+} + HSe^- \quad (5.2)$$

The description of the saturation indices of the phases and the molar concentrations of the species initially and after equilibrium for defined aqueous solutions is presented in this chapter, but will be furthermore discussed in combination with the analytical results of the laboratory syntheses of selenium doted iron sulfides (Ch. 5.3 and 5.5). These calculations are of high importance, because the comparison between analytical and modeled results allow a quality check of the own data with respect to consistency. Are the types of the precipitated phases in both systems, theoretically by thermodynamical calculations and analytically, identical? Which oxidation state of selenium occurs during precipitation? Furthermore, the thermodynamic results of the dissolved species in solution are helpful to describe the reaction pathways that occurred in the different types of syntheses. To perform the thermodynamic calculations, typical solution compositions for each doting experiment were chosen.

Species and equilibrium phases of the Se doted mackinawite experiments

The modeled solution to describe the synthesis of Se doted mackinawite with Se^{2-} initially present in solution consists of S^{2-} = 0.16 M , Fe^{2+} = 0.137 M, Se^{2-} = $9.1 \cdot 10^{-5}$ M , Na^{+} = 0.32 M, Cl^{-} = 0.274 M. The pH-value was inserted as 7, the pe-value was -3.4 (Eh = -0.2 V) and the O_2-content amounted to 3 ppm. The ionic strength before reaction of the solution was 0.41 M. The dissolved iron was mainly present in form of Fe^{2+} ($5.4 \cdot 10^{-2}$ M) and $Fe(HS)_2$ ($8.08 \cdot 10^{-2}$ M), while apart from the aqueous $Fe(HS)_2$ cluster, further dissolved sulfur species were in low amounts present as HS^{-} ($1.1 \cdot 10^{-4}$ M) and H_2S ($6.39 \cdot 10^{-5}$ M). The predominant selenium species in solution was HSe^{-}, with a concentration of $9.1 \cdot 10^{-5}$ M (Tab. 5.1).

Tab. 5.1: Dissolved species of Se doted mackinawite with Se^{2-} initially present in the solution before (upper line) and in (lower line) equilibrium (concentrations in M).

H_2S	$Fe(HS)_2$	HS^{-}	S_5^{2-}	S_6^{2-}	S_4^{2-}	S_3^{2-}	S_2^{2-}
6.39E-05	8.08E-02	1.10E-04	4.80E-07	2.27E-07	3.15E-07	1.29E-10	8.51E-12
1.50E-05	3.45E-08	7.22E-08	8.80E-13	4.16E-13	5.76E-13	2.37E-16	1.56E-17
S^{2-}	Fe^{2+}	$Fe(HS)_3^{-}$	$FeOH^{+}$	$Fe(OH)_2$	$Fe(OH)_3^{-}$	HSe^{-}	H_2Se
3.40E-10	5.40E-02	1.07E-03	6.58E-05	3.68E-09	2.03E-12	9.38E-05	3.93E-08
6.24E-16	5.34E-02	2.98E-13	1.82E-07	2.84E-14	4.38E-20	2.33E-11	3.50E-12

This solution was oversaturated with respect to mackinawite (SI = 5.7), pyrite (SI = 15.7), achavalite (SI = 27.0), ferroselite (SI = 15.6), FeSSe (SI = 15.7) and Se^0 (SI = 13.4). Although the solution was oversaturated of many phases, the calculated precipitating phases with the solution being in equilibrium were limited to mackinawite (maximum of precipitating amount (max) = $1.54 \cdot 10^{-4}$ M), pyrite (max = $8.24 \cdot 10^{-2}$ M) and Se^0 (max = $9.1 \cdot 10^{-5}$ M). After the reaction within the solution, the saturation indices of mackinawite, pyrite and Se^0 were zero, because these phases are in equilibrium with the solution. This means that in total the dissolution and precipitation of these phases was zero.

The solution composition of the Se doted mackinawite with Se^{4+} initially present in the solution differed only with regard to the selenium source (Na_2SeO_3) and the initial pe-value of 1.7 (Eh = 0.1 V). The dissolved sulfur was present as HS^{-} ($1.1 \cdot 10^{-4}$ M) and H_2S ($6.39 \cdot 10^{-5}$ M)

and iron was predominantly occurring in form of Fe^{2+} ($5.4 \cdot 10^{-2}$ M). Apart from these species, the aqueous $Fe(HS)_2$ cluster was present with a concentration $8.08 \cdot 10^{-2}$ M, while selenium occurred as $HSeO_3^-$ ($8.68 \cdot 10^{-5}$ M) and SeO_3^{2-} ($7.03 \cdot 10^{-6}$ M) (Tab. 5.2).

.

Tab. 5.2: Dissolved species in batch-experiments of Se doted mackinawite with Se^{4+} initially present in the solution before (upper line) and in (lower line) equilibrium (concentrations in M).

H_2S	$Fe(HS)_2$	HS^-	S_5^{2-}	S_6^{2-}	S_4^{2-}	S_3^{2-}	S_2^{2-}
6.39E-05	8.08E-02	1.10E-04	4.80E-07	2.27E-07	3.15E-07	1.29E-10	8.51E-12
1.50E-05	3.43E-08	7.21E-08	8.80E-13	4.16E-13	5.76E-13	2.37E-16	1.56E-17
S^{2-}	Fe^{2+}	$Fe(HS)_3^-$	$FeOH^+$	$Fe(OH)_2$	SeO_3^{2-}	H_2SeO_3	$HSeO_3^-$
3.40E-10	5.40E-02	1.07E-03	6.58E-05	3.68E-09	7.03E-06	3.24E-09	8.68E-05
6.24E-16	5.34E-02	2.97E-13	1.82E-07	2.85E-14	0.00E+00	0.00E+00	0.00E+00

The solution was oversaturated with regard to the minerals mackinawite (SI = 5.7), pyrite (SI = 25.9), Se^0 (SI = 13.4) and S^0 (SI = 8.4). The precipitating phases with the solution being in equilibrium were identical compared to the simulation of Se doted mackinawite by using Se^{2-}. These phases were mackinawite (max = $1.61 \cdot 10^{-4}$ M), pyrite (max = $8.24 \cdot 10^{-2}$ M) and Se^0 (max = $9.38 \cdot 10^{-5}$ M).

These results show that, independent of the initial Se valence state (Se^{2-}, Se^{4+}), the calculations predict the precipitation of selenium as Se^0 (without any iron-selenium compounds) next to the formation of mackinawite and pyrite.

Species and equilibrium phases of the instantaneous precipitation in batch-experiments

The modeled aqueous solution inserted into PhreeqC to calculate the reactions for the Se incorporation into pyrite with Se^{2-} initially present, contained $S^{2-} = 6.6 \cdot 10^{-2}$ M, $Fe^{2+} = 1.75 \cdot 10^{-2}$ M, $Se^{2-} = 1 \cdot 10^{-3}$ M, $Na^+ = 6.8 \cdot 10^{-2}$ M, $Cl^- = 5.25 \cdot 10^{-2}$ M. The oxygen concentration was 3 ppm, pH had a value of 4, and the pe was set to -1.7 (Eh = -0.1 V). The ionic strength of the solution was 0.077 M. As sulfur species, mainly H_2S ($4.8 \cdot 10^{-2}$ M) was initially present in the solution. Iron was predominantly dissolved in form of $Fe(HS)_2$ ($9.07 \cdot 10^{-}$

^{3} M) and Fe^{2+} ($8.24 \cdot 10^{-3}$ M), while the selenium species were HSe^{-} ($6.74 \cdot 10^{-4}$ M) and H_2Se ($6.74 \cdot 10^{-4}$ M) (Tab. 5.3). The solution was oversaturated with respect to the phases pyrite (SI = 12.1), mackinawite (SI = 1.9), Se^{0} (SI = 14.7), ferroselite (SI = 14.2), achavalite (SI = 24.3) and the solid solution phase FeSSe (SI = 13.1). With the solution being in equilibrium, the thermodynamic calculations predict that just the phases pyrite (max = $1.73 \cdot 10^{-2}$ M) and Se^{0} (max = $1 \cdot 10^{-3}$ M) precipitate from solution.

Tab. 5.3: Dissolved species in batch-experiments of Se doted pyrite with Se^{2-} initially present in the solution before (upper line) and in (lower line) equilibrium (concentrations in M).

H_2S	$Fe(HS)_2$	HS^-	S_5^{2-}	S_6^{2-}	S_4^{2-}	S_3^{2-}	S_2^{2-}
4.80E-02	9.07E-03	7.01E-05	2.64E-10	1.30E-10	1.64E-10	6.19E-14	3.75E-15
3.18E-02	7.66E-09	3.48E-07	9.83E-15	4.85E-15	6.06E-15	2.28E-18	1.38E-19
S^{2-}	Fe^{2+}	$Fe(HS)_3^-$	$FeOH^+$	$Fe(OH)_2$	$Fe(OH)_3^-$	HSe^-	H_2Se
1.68E-13	8.23E-03	7.05E-05	1.31E-08	8.72E-16	4.13E-22	6.74E-04	3.33E-04
6.13E-18	2.68E-04	2.95E-13	3.32E-12	1.69E-21	5.99E-30	1.18E-14	7.79E-13

With regard to the selenite incorporation into pyrite by batch experiments, the only difference in the hydrochemical composition was that selenite instead of selenide was taken as selenium source and the pe was 1.7 (Eh = 0.1 V). The most important species in solution were for iron $Fe(HS)_2$ ($9.07 \cdot 10^{-3}$ M) and Fe^{2+} ($8.24 \cdot 10^{-3}$ M), for sulfur H_2S ($4.8 \cdot 10^{-2}$ M) and for selenium $HSeO3^-$ ($9.64 \cdot 10^{-4}$ M) and H_2SeO_3. ($4.24 \cdot 10^{-5}$ M) (Tab. 5.4).

Tab. 5.4: Dissolved species in batch-experiments of Se doted pyrite with Se^{4+} initially present in the solution before (upper line) and in (lower line) equilibrium (concentrations in M).

H_2S	$Fe(HS)_2$	$Fe(HS)_3^-$	HS^-	S_5^{2-}	S_6^{2-}	S_4^{2-}	S_3^{2-}	S_2^{2-}
4.80E-02	9.07E-03	7.05E-05	7.02E-05	2.64E-10	1.30E-10	1.64E-10	6.19E-14	3.75E-15
3.17E-02	6.42E-09	2.49E-13	3.51E-07	1.00E-14	4.95E-15	6.19E-15	2.33E-18	1.40E-19
S^{2-}	Fe^{2+}	$FeOH^+$	$Fe(OH)_2$	HSe^-	H_2Se	SeO_3^{2-}	H_2SeO_3	$HSeO_3^-$
1.68E-13	8.24E-03	1.31E-08	8.72E-16	0.00E+00	0.00E+00	6.03E-08	4.24E-05	9.64E-04
6.25E-18	2.21E-04	2.77E-12	1.43E-21	1.00E-14	6.53E-13	0.00E+00	0.00E+00	0.00E+00

The solution is oversaturated of pyrite (SI = 18.9), mackinawite (SI = 1.9), S^0 (SI = 5.3), Se^0 (SI = 14.7), ferroselite (SI = 14.1), achavalite (SI = 24.0) and FeSSe (SI = 13.2). Finally, after equilibrium was attained, the calculations predict the precipitation of the phases pyrite (max = $1.74 \cdot 10^{-2}$ M) and Se^0 (max = $1 \cdot 10^{-3}$ M).

Species and equilibrium phases of the crystal growth synthesis in MFR-experiments

The modeled aqueous solution which was inserted into PhreeqC to simulate the MFR coprecipitation-experiments of Se incorporation into pyrite with Se^{2-} initially present in the solution, contained $S^{2-} = 10^{-3}$ M, $Fe^{2+} = 5 \cdot 10^{-4}$ M, $Se^{2-} = 2.5 \cdot 10^{-4}$ M, $Na^{+} = 10^{-3}$ M, and $Cl^{-} = 1.5 \cdot 10^{-3}$ M (Tab. 5.5). The pH was set steady at a value of 4, while the pe was set to -1.7, which is equal to an Eh-value of -0.1 V. The calculated value for the ionic strength of the solution was 0.0024 M.

Tab. 5.5: Dissolved species in MFR-coprecipitation experiments of Se doted pyrite with Se^{2-} initially present in the solution before (upper line) and in (lower line) equilibrium (concentrations in M).

H_2S	$Fe(HS)_2$	HS^-	S_5^{2-}	S_6^{2-}	S_4^{2-}	S_3^{2-}	S_2^{2-}
9.98E-04	4.67E-07	1.21E-06	3.52E-12	1.81E-12	2.06E-12	7.31E-16	4.17E-17
2.78E-04	2.54E-10	5.23E-08	2.36E-14	1.21E-14	1.38E-14	4.89E-18	2.78E-19
S^{2-}	Fe^{2+}	$Fe(HS)_3^-$	$FeOH^+$	$Fe(OH)_2$	$Fe(OH)_3^-$	HSe^-	H_2Se
1.71E-15	4.99E-04	6.14E-11	1.34E-09	1.08E-16	4.24E-23	1.57E-04	9.35E-05
1.14E-17	1.39E-04	1.45E-15	5.96E-11	7.56E-19	4.61E-26	6.72E-15	2.58E-14

The calculated supersaturated phases were elemental selenium (SI = 14.09), pyrite (SI = 7.8), ferroselite (SI = 12.13) and the FeSSe solid solution (SI = 9.96). No other iron hydroxide or iron sulfide phase (like e.g. mackinawite, marcasite or greigite), no sulfur phase (e.g. S^0) or selenium phase (e.g. FeSe) was oversaturated in the solution.

Calculating the equilibrium of the solution, the results show that only pyrite, with a maximum amount of $3.61 \cdot 10^{-4}$ M and elemental selenium (max = $2.5 \cdot 10^{-4}$ M) precipitate from the solution. This shows that the whole initial amount of dissolved Se^{2-} precipitates as Se^0 and not as iron selenide compound (e.g. ferroselite, FeSSe).

The only difference in the hydrochemical composition of selenite coprecipitation experiments with respect to selenide is that Na_2SeO_3 as selenium source was taken and the electrochemical cell was adjusted to a pe of 1.7 (Eh = 0.1 V). The most important dissolved species present in the solution were H_2S ($9.87 \cdot 10^{-4}$ M), Fe^{2+} ($4.95 \cdot 10^{-4}$ M), and $HSeO_3^-$ ($2.46 \cdot 10^{-4}$ M) (Tab. 5.6). Following the calculations, the precipitates are pyrite ($5 \cdot 10^{-4}$ M) and Se^0 ($2.5 \cdot 10^{-4}$ M) and no other phase.

Tab. 5.6: Dissolved species in MFR-coprecipitation experiments of Se doted pyrite with Se^{4+} initially present in the solution before (upper line) and in (lower line) equilibrium (concentrations in M).

H_2S	$Fe(HS)_2$	HS^-	S_5^{2-}	S_6^{2-}	S_4^{2-}	S_3^{2-}	S_2^{2-}
9.98E-04	4.67E-07	1.21E-06	3.52E-12	1.81E-12	2.07E-12	7.32E-16	4.17E-17
2.61E-07	5.55E-19	3.77E-11	1.30E-17	6.71E-18	7.62E-18	2.70E-21	1.54E-22
S^{2-}	Fe^{2+}	$Fe(HS)_3^-$	$FeOH^+$	$Fe(OH)_2$	SeO_3^{2-}	H_2SeO_3	$HSeO_3^-$
1.71E-15	4.99E-04	6.13E-11	1.34E-09	1.08E-16	8.83E-09	1.26E-05	2.37E-04
6.29E-21	5.77E-07	2.28E-27	1.92E-13	1.88E-21	7.22E-37	7.37E-32	1.65E-31

Although the initial Se valence states vary (Se^{2-}, Se^{4+}) as well as the solutions (instantaneous precipitation and nucleation of Se doted pyrite in batch-experiments and crystal growth of Se incorporation into pyrite in MFR experiments) differ with regard to the initial concentrations and the hydrochemical conditions of the reactants, the predicted precipitations of the thermodynamical calculations are equal. For the solutions presented in Table 5.2 – 5.6, the equilibrium phases solely are pyrite and elemental selenium.

Pourbaix diagrams

Stability diagrams have been generated using PhreeqC for modeling the expected thermodynamically stable phases with regard to selenium and iron sulfides for a solution containing $S = 10^{-3}$ M, $Fe = 5 \cdot 10^{-4}$ M, and $Se = 2.5 \cdot 10^{-4}$ M (Figs. 5.1 – 5.3) identical to the aqueous solution from MFR experiments, or with the same concentrations of sulfur and iron but with less $[Se_{tot}] = 10^{-10}$ M (Fig. 5.3) at 25° C and 1 bar.

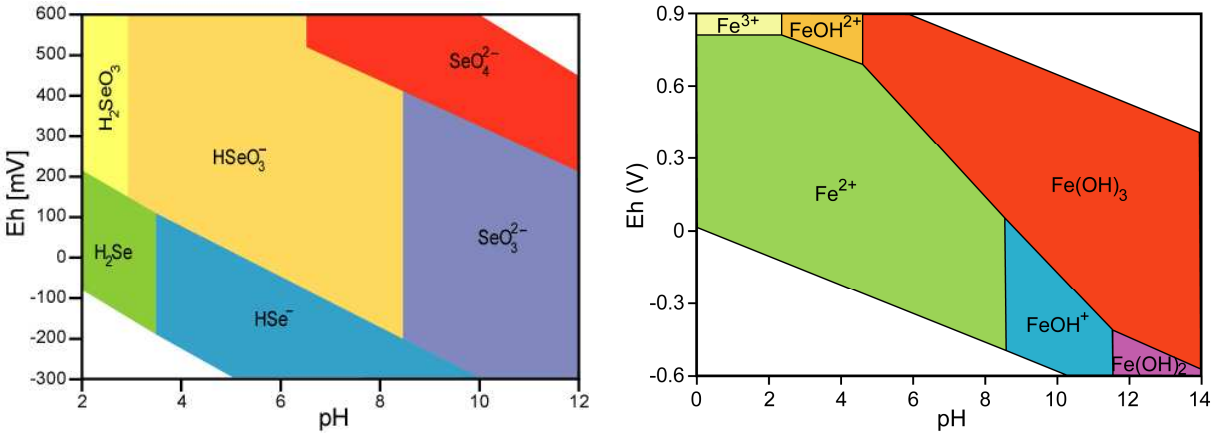

Fig. 5.1: Pourbaix diagrams for a solution containing [S_{tot}] = 10^{-3} M, [Fe_{tot}] = $5 \cdot 10^{-4}$ M, [Se_{tot}] = $2.5 \cdot 10^{-4}$ M at standard conditions and an ionic strength of ~0.1 mol/kg; Left: predominating dissolved selenium with stable phases removed; Right: predominating dissolved iron with stable phases removed.

Under acidic to circumneutral conditions (pH 0 – 8.5), iron is mainly stable as Fe^{2+} (Fig. 5.1), while under alkaline conditions above pH 8.5 $FeOH^+$ and $Fe(OH)_2$ are predominating under reducing conditions. The Pourbaix diagram only of the dissolved selenium species (Fig. 5.1) shows that the selenides H_2Se at pH <3.7 and HSe^- coincide with the pyrite stability field (Fig. 5.2), which is ranging from Eh -0.2 – 0.1 V at pH 2 until -0.3 V at pH 7.5.

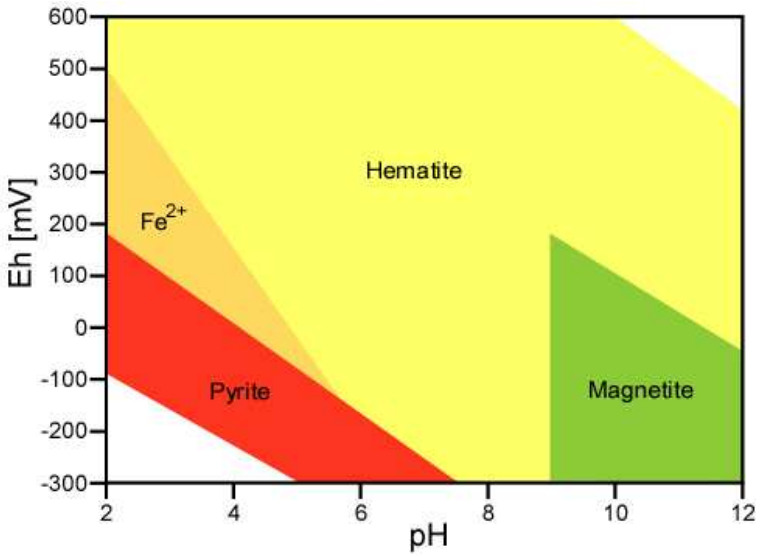

Fig. 5.2: Pourbaix diagrams for a solution containing [S_{tot}] = 10^{-3} M, [Fe_{tot}] = $5 \cdot 10^{-4}$ M, [Se_{tot}] = $2.5 \cdot 10^{-4}$ M at standard conditions and an ionic strength of ~0.1 mol/kg showing most stable phases in the Fe-S system.

This suggests that under anoxic and acidic conditions, a substitution of reduced sulfur by selenium could occur. But in fact, the most stable phase of Se under formation conditions of pyrite is Se^0 (Fig. 5.3), indicating that Se may precipitate and be incorporated into pyrite as a crystal defect without any further atomic bonding and not as a "true" solid solution.

This is also valid for much lower Se concentrations (Fig. 5.3) of about $[Se_{tot}] = 10^{-10}$ M which is assumed to be a likely amount reaching the biosphere from HLW disposal sites if getting into contact with groundwater (Séby et al., 1998).

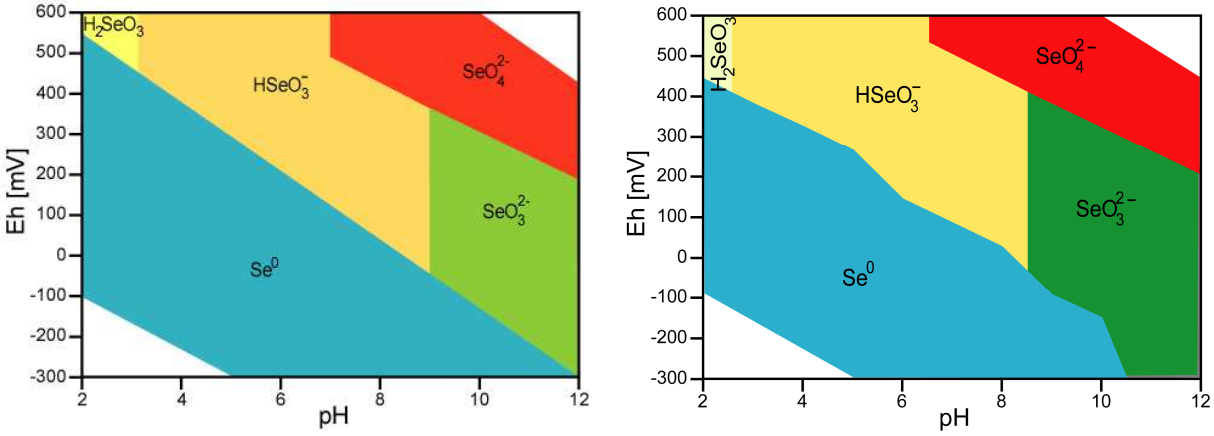

Fig. 5.3: Left: stability diagram for most stable Se mineral phases for a solution containing $[S_{tot}] = 10^{-3}$ M, $[Fe_{tot}] = 5 \cdot 10^{-4}$ M, $[Se_{tot}] = 2.5 \cdot 10^{-4}$ M; Right: stability diagram for $[S_{tot}] = 10^{-3}$ M, $[Fe_{tot}] = 5 \cdot 10^{-4}$ M, $[Se_{tot}] = 10^{-10}$ M. Both solutions were at standard conditions.

5.2 Mineralogical characterization of selenium doted mackinawite and pyrite

Mackinawite

For selenium doted mackinawite synthesized by instantaneous precipitation and nucleation in batch experiments (Ch. 4.1, Tab. 5.1 and 5.2), neither Se^0 nor achavalite (FeSe) or ferroselite ($FeSe_2$) was detected by SEM or XRD (Fig. 5.4). The X-ray diffractogram from batch runs 1 and 2 show the strongest diffraction peaks, which all belong to mackinawite. In the runs 3 – 10 where pure Se doted mackinawite precipitated instead of Se doted pyrite, only the characteristic broad peak at around 5 nm was observed in XRD analyses, which

derives from the c-spacing of the mackinawite layers (Ch. 2.2.1; Rickard and Morse, 2005) or comparably broad peaks with a low intensity. These peaks were located at the 2-Theta-values 17°, 30°, 39°, 50°, 59°, where the intensity of the mackinawite diffraction signal is highest.

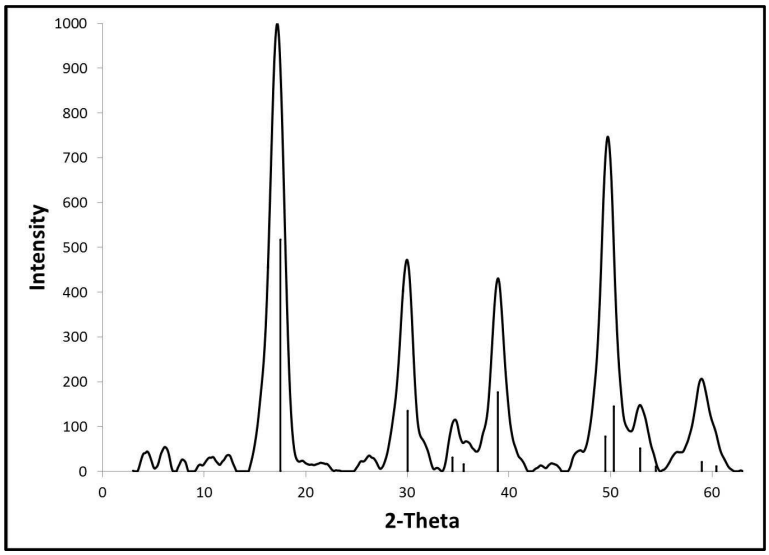

Fig. 5.4: XRD pattern of synthetic selenium doted mackinawite particles with (vertical) natural mackinawite reference peaks.

The BET-investigations measured a specific surface area of mackinawite of 3.2 m^2/g. The ED-XRF results indicated a reasonable stoichiometric Fe-S ratio of 0.95 : 1.05 for synthesized Se^{2-} doted mackinawite (Fe = 48.7 mol%; S = 51.1 mol%; Se = 0.09 mol%).

Synthesized mixtures of iron sulfides by instantaneous precipitation experiments

The synthesis of pure selenium doted pyrite by starting with a solution containing 0.067 M NaHS, 0.033 M $FeCl_3 \cdot 6H_2O$ and up to $1 \cdot 10^{-3}$ M Na_2SeO_3 at pH-values of 3.5 to 5.0 and Eh-values between -200 and -50 mV was unsuccessful. Next to pyrite, other iron sulfides occurred. In such systems, mixtures of pyrite, and/or greigite, and/or marcasite and/or mackinawite precipitated, all containing selenium, which has been detected by the EDX coupled to the SEM. A typical XRD-spectrum of such mixtures shows Figure 5.5. The failure

to synthesize selenium doted pyrite with an initial Fe-S ratio of 1:2 was attributed to kinetic reasons, because pyrite is the most stable species (Fig. 2.13).

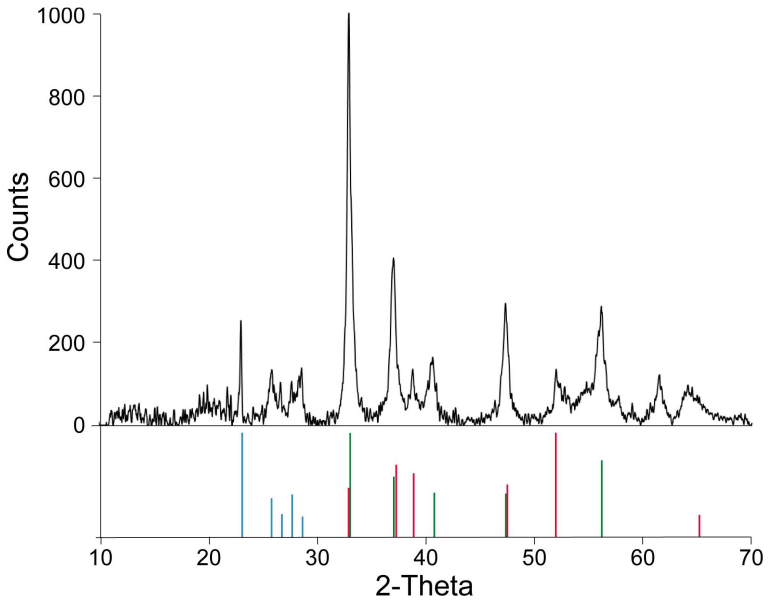

Fig. 5.5: Typical XRD spectra for selenium doted pyrite synthesis with an Fe-S ratio of 1:2. The vertical lines below the XRD-spectra show the intensities relative to the highest intensity of each mineral. The blue line stands for elemental sulfur, the green line for pyrite and the red line represents marcasite. The broad peak with low intensity around 20° of 2-T heta was identified as poorly crystalline mackinawite.

Incorporated selenium in pyrite by instantaneous precipitation experiments

In the initial solutions of the instantaneous precipitation experiments (Ch. 4.1; Tab. 5.3 and 5.4), mackinawite and greigite were supersaturated (with saturation indices of 2 – 7) as well as pyrite (saturation index of >12). Immediately after mixing the initial ingredients for iron sulfide synthesis, a rapid precipitation of black solid material occurred. This initial precursor phase of pyrite was mackinawite. Progressively, mackinawite recrystallized into the more thermodynamically stable pyrite starting after ~1 day.

The precipitated phases of the solutions show in the XRD spectra only pyrite phases which can be identified which are very similar to the XRD spectra of natural pure pyrite samples (Fig. 5.6). Neither achavalite (FeSe), ferroselite ($FeSe_2$) nor elemental selenium (Se^0) was detected by SEM or XRD. The detection limit of the XRD is 1 wt.%. Since no other phase

than pyrite could be observed, a high purity of the synthesis product is assumed. According to previous authors, the purity of pyrite synthesized by the method after Wei and Osseo-Asare (1996) is higher than 99.5 wt.% (Wei and Osseo-Asare, 1997; Liu et al., 2008). The specific surface area, as determined by BET-measurements of these pyrites is 12.1 m^2/g.

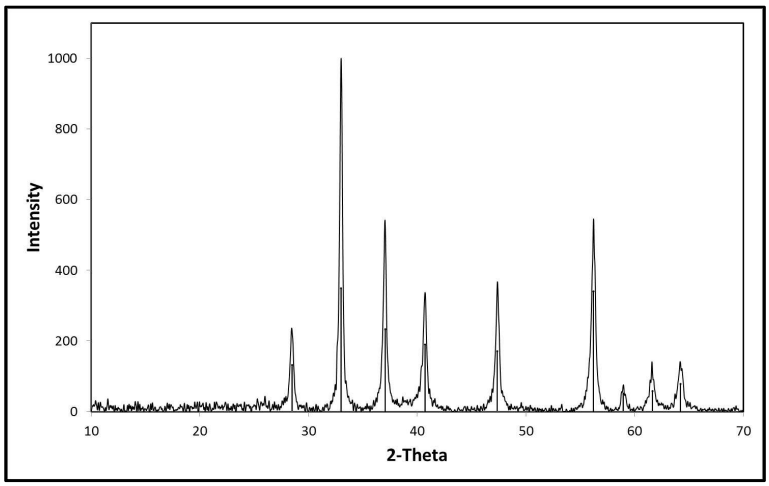

Fig. 5.6: XRD pattern of selenium doted pyrite particles, synthesized in instantaneous precipitation experiments with (vertical) natural pyrite peaks, as reference.

A thin section analysis by SEM shows that pyrite particles have a massive structure inside (Fig. 5.7). A grain to grain comparison of the Se-contents has been measured by the combined EDX-system. The result indicates a homogenous distribution of selenium between the grains. The average selenium content of 1.7 wt.% varied in 21 different grains by ±3.8 %.

A TEM picture shows a thin section of Se doted pyrite particles with Se^{2-} initially present in the solution. This thin section has a thickness of 30 nm (Fig. 5.7), revealing that individual pyrite grains are polycrystalline. These crystallites differ in size and orientation, as indicated by the varying brightness of the reflected light.

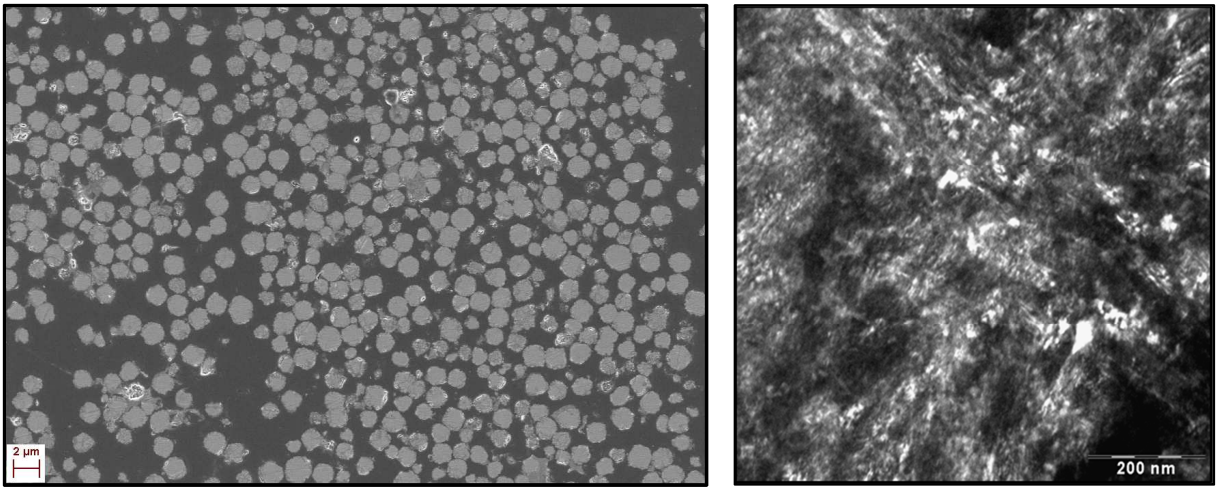

Fig. 5.7: Left: SEM-image of pyrites thin section; Right: TEM images of pyrite grain thin sections with a thickness of 30 nm. The dark filtered TEM image shows the internal structure of the grain. The different grey scales are due to the difference in orientation of the microcrystals.

Additionally, elemental mappings of the selenium concentration in grains by EDX system coupled to FIB were done in order to find out if a solid solution is present or not. A solid solution is defined by its homogeneous crystalline structure. The mapping illustrates that the selenium concentration increases towards the center of the grain (Fig. 5.8).

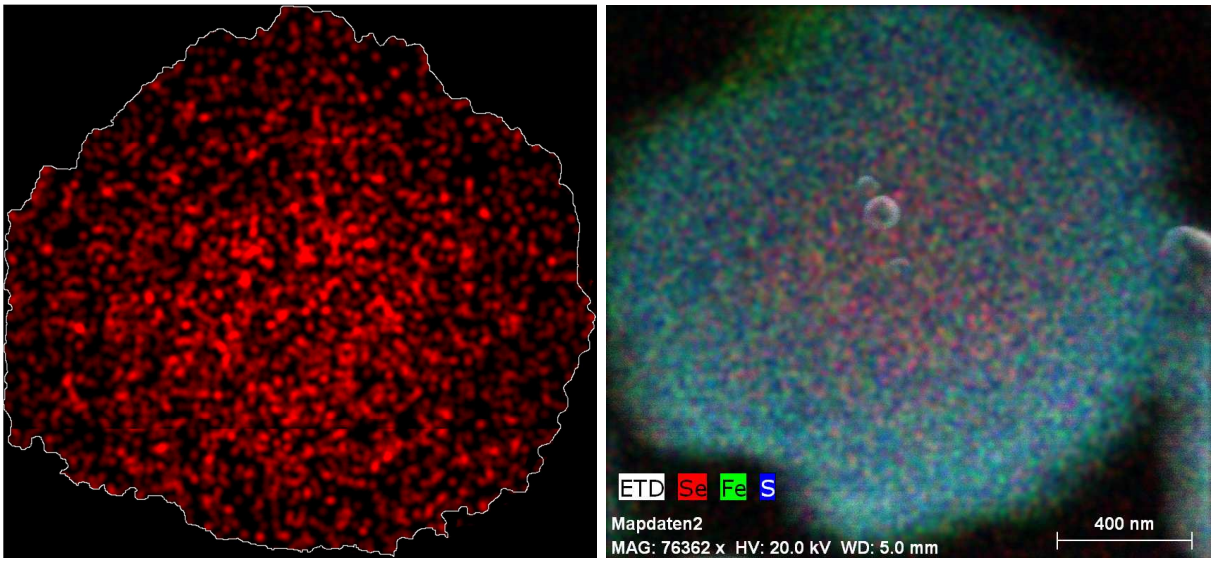

Fig. 5.8: Mapping of the selenium content within a pyrite grain (30 nm thin section). The red dots in the left picture represent a high selenium concentration, which is higher in the middle of the grain. The map on the right side shows the element distribution of iron (green), sulfur (blue), and selenium (red).

This zoning resulted from a decrease of the selenium-to-sulfur ratio in the residual solution after the initial formation of black colored pyrite precursor phases. A release of selenium during recrystallization of mackinawite to pyrite could not be substantiated by SEM or by XRD.

The ED-XRF results (Fig. 5.9) for synthesized selenide doted pyrite indicated a reasonable stoichiometry with a Fe-S ratio of 1:2.02 (Fe: 32.7 mol%; S: 66.1 mol%; Se: 1.2 mol%). Furthermore, the molar concentrations of selenium in pyrite, calculated by the difference between the initial and the residual concentrations, have been compared with the molar concentrations of selenium measured by ED-XRF (Fig. 5.9), with very similar results (Correlation: r = 0.98).

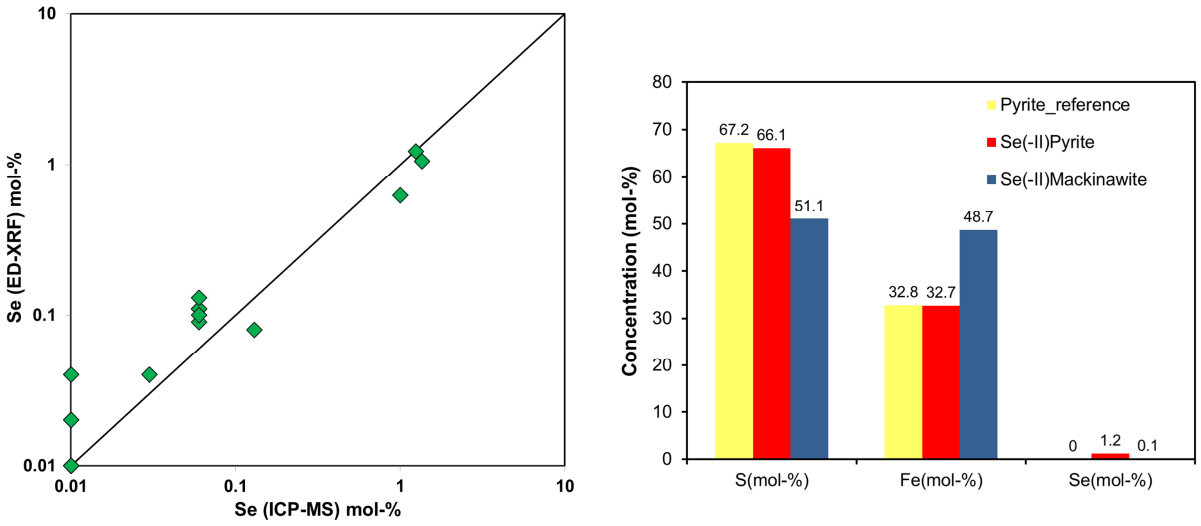

Fig. 5.9: Left: Comparison of ICP-MS and ED-XRF results with regard to selenium contents (log mol%) in precipitated iron sulfides in batch runs. Right: Concentrations of Se, S, Fe in natural pyrite and synthesized Se doted pyrite and mackinawite.

Incorporated selenium in pyrite by crystal growth experiments

Mineralogical identification by XRD of selenium doted pyrite obtained from crystal growth on persisting nuclei in MFR experiments reveals the formation of mainly pyrite coatings on natural, grounded grains (Fig. 5.10; Ch. 4.2; Tab. 5.5 and 5.6) by mixing a solution of

S = 10^{-3} M, Fe = $5 \cdot 10^{-4}$ M, and Se = $2.5 \cdot 10^{-4}$ M at pH 4 for Se^{2-} and for Se^{4+}, respectively. The specific surface area of the precipitates is 0.46 m^2/g.

During the period of an experiment, the average precipitated solid amounts were 0.0385 g (of initial 0.044 g) for sulfur, 0.027 g (of initial 0.038 g) for iron and 0.00446 g (of initial 0.0045 g) for selenium. The precipitated iron and sulfur was 0.0655 g in total, without considering Se. Conversion of this value to the whole solid, which includes natural pyrite nuclei and coprecipitated iron sulfide, the precipitated amount of 0.0655 g is equal to 11.6 % of the total. Since the detection limit is ~1 wt.% for XRD and no other phase than pyrite could be detected, it is assumed that mainly pyrite precipitated. If more or less crystallized mackinawite or any other iron sulfide in an amount of more than 10 % would have been part of the MFR-samples, notably peaks of these phases in the XRD spectra would have occurred.

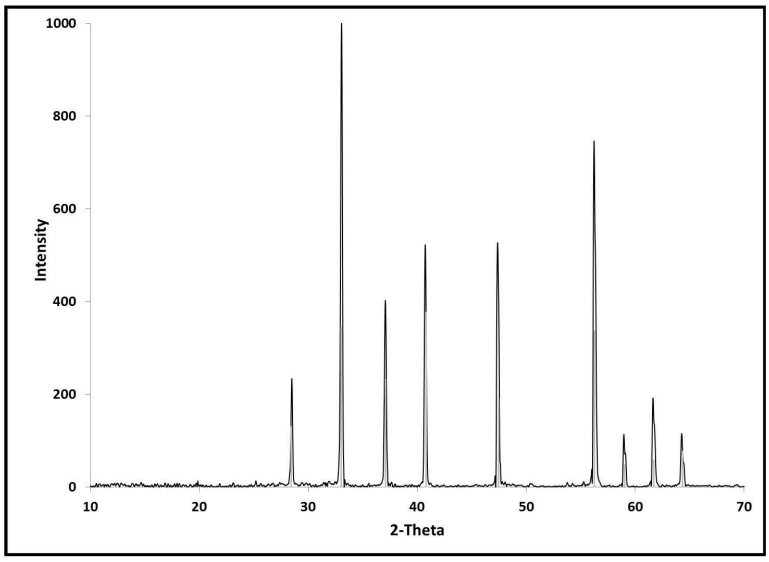

Fig. 5.10: XRD-spectra of Se doted pyrite from crystal growth-experiments.
Peaks of diffraction are consistent with pure pyrite (grey vertical lines).

Due to the low selenium concentrations, it is impossible to detect feasible precipitations of Se^0, achavalite or ferroselite by XRD. Thin sections could not be made successfully out of these Se doted pyrite particles, because the solid was too fragile.

To sum up the mineralogical constraints of the selenium doted samples which precipitated from aqueous solutions, no phase next to pyrite could be detected by SEM or XRD. The continuous addition of the solution into the MFR under permanently stirring in crystal growth experiments lead to a coagulation of the initial nuclei into comparatively large particles, as indicated by the low specific surface area. The Se doted pyrites of the instantaneous precipitation experiments have a limited crystal growth and, therefore, a specific surface area which is ~26 times higher than the pyrite particles synthesized in crystal growth experiments. Selenium is inhomogeneously distributed in the pyrite particles, indicating that no real solid solution was synthesized in the nucleation and instantaneous precipitation experiments.

Incorporation of Se doted pyrite by condensation from gaseous species

The synthesis of pure phases of selenium doted pyrite was successful for the described setup, following the principal reaction path (Ch. 4.3; Eq. 4.3). Further experiments with higher Se contents up to a molar mixture of Fe:S:Se amounting 1:1:1 as well as all syntheses with a temperature gradient of 700° – 600° C only in one d irection for up to 14 days resulted in mixtures of pyrite and pyrrhotite (FeS_{2-x}) or in precipitation of amorphous solids. The XRD pattern shows no additional minerals apart from pyrite (Fig. 5.11). As well, the intensity of the reference spectra (grey lines) is in good agreement with the XRD-spectra of the sample (black line).

A thin section of the single crystal was prepared to measure the homogeneity of the Se content by EDX within a grain (Fig. 5.12). This SEM image shows two selenium doted pyrite grains, connected with each other by a Se-S-compound. This Se-S-compound has precipitated after no Fe was anymore available for further pyrite growing.

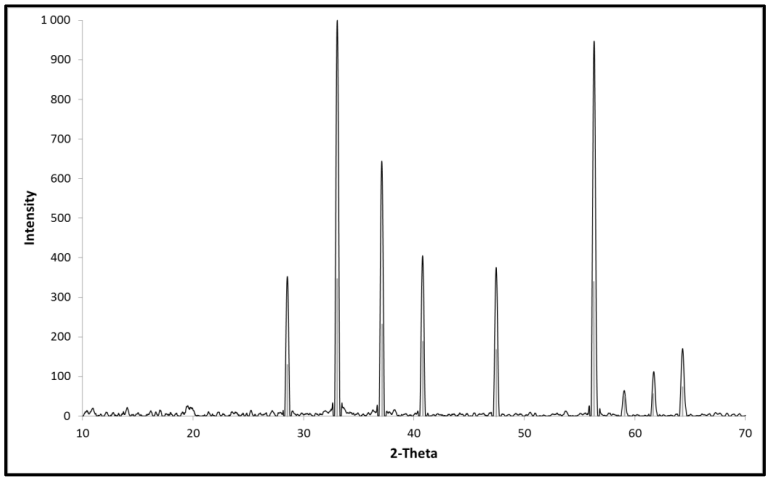

Fig. 5.11: XRD-spectra of selenium doted pyrite from condensation after sublimation experiments. Peaks of diffraction are consistent with the pyrite reference (grey vertical lines).

The selenium concentration within the pyrite solid is very homogeneous, as shown by the measured linescans. The average of all 668 points is 4.42 counts per second with a standard deviation of 0.21. High variations of Se content occurred only at breaks or cracks, which were results of the thin-section production (Fig. 5.12).

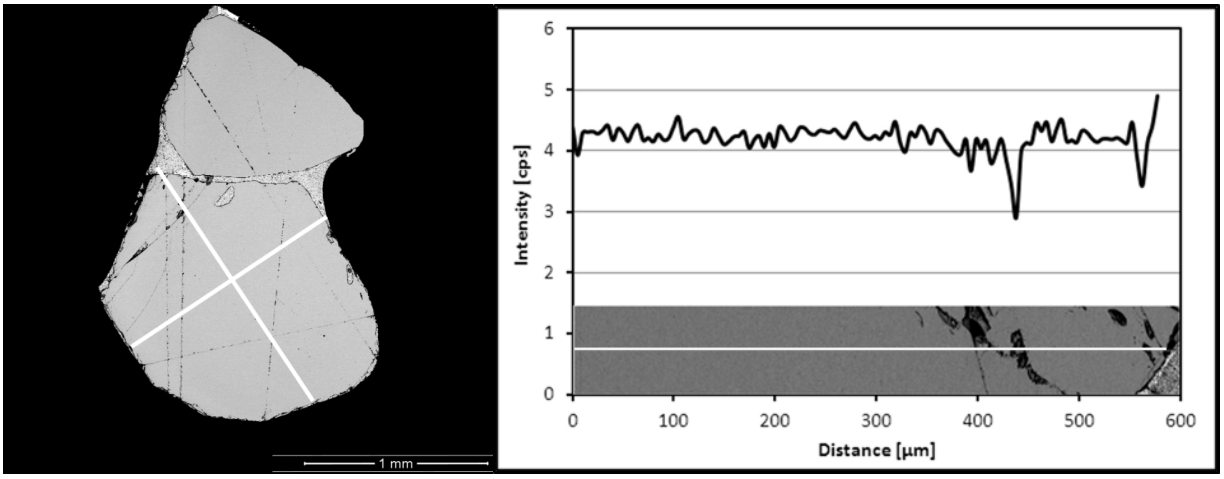

Fig. 5.12: Left: SEM-image showing a selenium doted pyrite thin section and the respective pathways of the linescans (white lines); Right: Analyses of selenium doted pyrite thin section showing the measured Se-intensity (in counts per second) of a part of a thin-section and the respective SEM image. The white line in the image is identical to the measurement route.

The selenium concentration of Se doted pyrites synthesized by condensation from sublimation was 1.1 wt.%, which has been measured by ED-XRF. The initial stoichiometry of the S-Fe-Se-reactants was 0.9 : 0.5 : 0.1. If all elements would have been incorporated in the same ratio as they have been initially added for reaction, the selenium content in pyrite would have been 6.67 mol%. But in fact, the determined molar concentration is about ten times lower with a distribution ratio of 0.09 compared to the initial ratio of the reactants. A possible explanation of the low incorporation could be that selenium did not react with iron. Although selenium is homogeneously distributed, which could be an indicator of a real Fe-S-Se solid solution, accompanied with a substitution of S by Se, the low Se concentrations within the solid is surprising. Hence, XAFS results should clarify the type of structural Se-bonding within pyrite (Ch. 5.5).

5.3 Retention of selenium by incorporation into mackinawite and pyrite

Mackinawite

ICP-MS analyses of the residual selenium contents in solution reveal a high efficiency of selenium incorporation under acidic to circumneutral pH and mainly reduced Eh-conditions, the average selenium removal being 98.3 % ranging between 94.1 and 99.6 % by selenium doted mackinawite (Tab. 5.7). This is close to the calculated precipitation maximum of selenium on the basis of the thermodynamic data. The calculated incorporation of selenium does not show significant differences due to the initial solution composition nor to the hydrochemical conditions. The amount of selenium in mackinawite for the runs 1 and 2 is 0.07 g/L. The total precipitated amount of Se doted mackinawite is 29.7 g/L.

Tab. 5.7: Hydrochemical conditions, initial and residual (res.) concentrations of S, Fe and Se, the resulting removal of Se (in %) for synthesized mackinawite.

Run	pH	Eh	S_initial	S_res.	Fe_initial	Fe_res.	Se_initial	Se_res.	Se_rem.
		[mV]	[mol/L]	[mol/L]	[mol/L]	[mol/L]	[mol/L]	[mol/L]	%
1	7	-200	3.5E-01	1.7E-03	3.4E-01	1.0E-02	9.1E-04	4.1E-06	99.5
2	7	+100	3.5E-01	1.6E-03	3.4E-01	1.3E-02	9.1E-04	3.6E-06	99.6
3	4.5	-300	5.5E-02	5.6E-04	2.7E-02	1.5E-02	9.1E-04	5.7E-06	99.4
4	3.5	-250	6.6E-02	1.0E-03	1.6E-02	2.4E-03	1.0E-03	4.4E-06	99.6
5	6	-200	6.6E-02	1.2E-04	1.7E-02	2.0E-05	1.0E-03	1.4E-05	98.6
6	5.5	-200	5.5E-02	4.1E-04	2.7E-02	9.1E-03	9.1E-05	6.0E-07	99.3
7	5.5	-200	5.5E-02	5.5E-04	2.7E-02	1.5E-02	9.1E-06	3.9E-07	95.7
8	5.5	-200	5.5E-02	4.2E-04	2.7E-02	9.8E-03	9.1E-06	1.4E-07	98.5
9	5.1	-100	6.0E-02	7.1E-04	3.3E-02	1.1E-02	2.7E-05	1.6E-06	94.1
10	5.8	-100	6.6E-02	1.6E-04	3.3E-02	1.4E-03	1.0E-03	1.6E-05	98.4

The removal efficiency of sulfur by precipitation from the solution is very similar to that of selenium with an average of 99.2 %, ranging between 98.8 and 99.8 %. The removal efficiency of iron is highly variable with 76 % on average, ranging between 44.4 – 99.9 %. A possible reason for the high variance of residual iron in solution could be attributed to the lack of sufficient dissolved sulfide species, which may be bonded as S^0. In the solutions prepared for the synthesis of mackinawite with Fe^{2+} as iron source (Run 1 and 2), the iron removal is relatively high with >96 %.

Mixed iron sulfides

Results of ICP-MS measurements of the residual selenium concentration reveal an average selenium removal of 97 % in all selenium doted mixed iron sulfide phases in the runs 11 – 22 (Tab. 5.8). The batch-runs with the numbers 15 and 19 have significantly lower incorporation efficiencies, lowering the average Se-removal for this group. There is no obvious reason (e.g. the mineral composition or the hydrochemical conditions) for this observation and remains therefore unclear. In total, it can be assumed that marcasite as well as greigite could have a remarkable potential for uptaking selenium, similar to mackinawite and pyrite. Greigite and marcasite have not been synthesized due to the lack of necessary instruments (e.g. autoclave).

Tab. 5.8: Hydrochemical conditions, initial and residual (res.) concentrations of S, Fe and Se, the resulting removal of Se (in %) for mixtures of mackinawite, greigite, marcasite and pyrite.

Run	pH	Eh	S_initial	S_res.	Fe_initial	Fe_res.	Se_initial	Se_res.	Se_remov.
		[mV]	[mol/L]	[mol/L]	[mol/L]	[mol/L]	[mol/L]	[mol/L]	%
11	4.5	-200	5.5E-02	5.6E-04	2.7E-02	7.2E-03	9.1E-04	4.2E-06	99.5
12	4.5	-200	5.5E-02	5.1E-04	2.7E-02	7.3E-03	9.1E-05	4.8E-07	99.5
13	4.5	-200	5.5E-02	3.6E-04	2.7E-02	1.0E-02	9.1E-06	1.5E-07	98.4
14	4	-200	5.5E-02	3.4E-04	2.7E-02	1.4E-02	9.1E-06	8.4E-08	99.1
15	5	-150	6.6E-02	1.0E-03	3.3E-02	1.5E-02	5.0E-05	5.6E-06	88.8
16	3.5	-200	6.6E-02	6.7E-03	3.3E-02	1.0E-02	5.0E-05	2.3E-07	99.5
17	5.1	-50	6.6E-02	9.9E-04	3.3E-02	1.1E-02	5.0E-05	3.5E-07	99.3
18	4.7	-100	6.6E-02	7.9E-04	3.3E-02	1.9E-03	5.0E-05	2.0E-07	99.6
19	4	-100	6.6E-02	1.2E-03	3.3E-02	1.8E-02	5.0E-05	4.0E-06	92.0
20	5	-50	6.6E-02	5.8E-03	3.3E-02	8.8E-03	5.0E-05	4.8E-07	99.0
21	4.5	-100	6.6E-02	2.3E-03	3.3E-02	1.4E-02	5.0E-05	3.1E-07	99.4
22	5	-100	6.6E-02	3.3E-03	3.3E-02	1.0E-02	5.0E-05	3.3E-07	99.3

Selenite in pyrite

The different solutions prepared for Se doted pyrite with Se^{4+} initially present (runs 23 – 27 and Q1; Tab. 5.4 and 5.6) precipitated at hydrochemical conditions with pH 4 – 5 and Eh-values at 50 – 100 mV (Tab. 5.9). The average Se-removal in the batch-experiments was 98.6 % with a range of 97.5 – 99.2 %. The average removal efficiency of sulfur was 98.8 % (range: 97.4 – 99.9 %), which is comparable to the selenium removal, while iron is bound in solids with an amount of 93.7 % (range: 87.6 – 99.8 %).

Tab. 5.9: Hydrochemical conditions, initial and residual (res.) concentrations of S, Fe and Se, the resulting removal of selenium (in %) and the type of synthesized pyrite with selenite initially present in solution. Numbers stand for the batch-runs and Q stands for MFR-experiments.

Run	pH	Eh	S_initial	S_res.	Fe_initial	Fe_res.	Se_initial	Se_res.	Se_remov.
		[mV]	[mol/L]	[mol/L]	[mol/L]	[mol/L]	[mol/L]	[mol/L]	%
23	4	100	6.6E-02	1.0E-03	1.7E-02	2.1E-03	5.0E-05	8.6E-07	98.4
24	5	100	6.6E-02	1.7E-03	1.7E-02	3.6E-05	5.0E-05	1.2E-06	97.5
25	4	50	6.6E-02	9.3E-05	1.7E-02	2.1E-03	5.1E-06	4.7E-08	99.1
26	4.5	50	6.6E-02	2.7E-04	1.7E-02	7.8E-04	5.1E-06	5.0E-08	99.0
27	5	50	6.6E-02	7.2E-04	1.7E-02	3.4E-04	5.1E-06	4.2E-08	99.2
Q1	4	100	6.0E-03	3.1E-04	3.0E-03	2.1E-04	2.5E-04	5.1E-06	99.5

Selenide in pyrite

The aqueous solutions prepared for Se doted pyrite with Se^{2-} initially present (runs 28 – 35 and Q2; Tab. 5.3 and 5.5) were fixed at hydrochemical conditions with a pH 3.7 – 5 and at an Eh-value of -100 mV (Tab. 5.10). ICP-MS results of the residual selenium concentration reveal an average selenium removal of 98.4 % with a range of 98.4 – 99.9 % (Tab. 5.10). 99.4% of sulfur precipitated on average (range: 98.7 – 99.9 %) whereas iron was removed from solution with 93.4 % (87.6 – 99.9 %).

Tab. 5.10: Hydrochemical conditions, initial and residual (res.) concentrations of S, Fe and Se, the resulting removal of Se (in %) and the type of synthesized pyrite with selenide initially present in solution. Numbers stand for batch-runs and Q stands for MFR-experiments.

Run	pH	Eh	S_initial	S_res.	Fe_initial	Fe_res.	Se_initial	Se_res.	S_remov.
		[mV]	[mol/L]	[mol/L]	[mol/L]	[mol/L]	[mol/L]	[mol/L]	%
28	3.9	-100	6.6E-02	8.5E-04	1.6E-02	9.1E-04	5.0E-05	5.9E-07	98.7
29	3.7	-100	6.6E-02	6.1E-04	1.7E-02	2.1E-03	5.0E-05	3.9E-07	99.1
30	3.9	-100	6.6E-02	4.0E-04	1.7E-02	2.1E-03	5.0E-05	2.9E-07	99.4
31	4.3	-100	6.6E-02	7.2E-04	1.6E-02	1.8E-04	5.0E-05	6.1E-07	98.9
32	5	-100	6.6E-02	5.3E-05	1.6E-02	3.2E-03	5.0E-05	2.6E-07	99.9
33	4	-100	6.6E-02	5.4E-05	1.7E-02	7.8E-05	1.0E-03	8.3E-06	99.2
34	4	-100	6.6E-02	1.1E-04	1.7E-02	1.1E-04	5.1E-06	1.9E-08	99.6
35	5	-100	6.6E-02	1.1E-04	1.7E-02	1.8E-05	5.1E-06	8.0E-08	98.4
Q2	4	-200	6.0E-03	2.7E-04	3.0E-03	1.9E-04	2.5E-04	3.3E-06	99.7

The amount of precipitated pyrite was between 1.7 and 1.9 g/L while the average amount of precipitated selenium in pyrite was 99 %. The weighted amounts are even slightly higher due to the losses of solids at the glass wall of the vials used for synthesis and decantation. The measured amount of precipitates is close to the thermodynamic calculations, thus calculating a maximum of 2.1 g/L precipitated pyrite and nearly 100 % removal of precipitated selenium (Ch. 5.1).

The uptake of Se^{2-} and Se^{4+} of Se doted pyrite in crystal growth experiments (Q 1 and 2) is higher than 99.5% and demonstrates again the affinity of Se to iron sulfides. The higher efficiency of selenium incorporation in the crystal growth experiments compared to the

instantaneous precipitation experiments is partially due to the experimental setup. Precipitation of selenium doted pyrite precursor phases in batch experiments occurs instantaneously. The particles accumulate at the bottom of the vial without any further contact with the supernatant solution because of the lack of solution circulation.

The average Se-uptake in the 35 batch runs in all experiments was 98 %. Finally, there was no significant difference in the uptake of selenium in relation to the type of precipitated iron sulfide phase, the initial amount of selenium, nor the hydrochemical conditions.

The high efficiency of selenium incorporation presented here is in agreement with the results of Liu et al. (2008), who reported from a sorption study of selenide immobilization by pyrite that more than 97 % of the initial selenide in solution precipitated on the pyrite surface after only five minutes of reaction. Similarly, Naveau et al. (2007) found a significant sorption of Se^{2-} and Se^{4+} on synthetic pyrite especially under acidic conditions, with adsorption efficiencies of more than 95 % for a pH of less than 5.

Kinetics of selenium uptake by pyrite in instantaneous precipitation experiments

Concerning the kinetics in instantaneous precipitation experiments (Ch. 4.1; Tab. 5.3), the results show that >98 % of S, Fe and Se^{2-} were removed from the solution within 1 h (Fig. 5.13). The concentrations of S, Se, and Fe were measured 1, 5, 10, 20, 50 and 100 hours after the start of mixing.

After 1 h, the concentration of iron was almost constant, while the selenium content decreased slowly and was finally in equilibrium after 20 h. The dissolved sulfur shows a minimum concentration shortly after a mixing, followed by an increase in solution. At the minimum of the sulfur concentration, the initially dissolved sulfide is bound in mackinawite and partially precipitated as S^0 due to the oxidation of sulfide accompanied with the reduction of Fe^{3+} to Fe^{2+} (Wei and Osseo-Asare, 1996). The following increase of sulfur after 10 h is most probably due to dissolution of S^0, because the solution is undersaturated with regard to sulfide. The further decrease in the dissolved sulfur concentration is caused by the reaction of sulfide with dissolved iron, coprecipitating on persisting pyrite particles. These results are

consistent with the interpretation of the element mapping by FIB (Ch. 5.2), showing a higher selenium concentration in the center of the pyrite grain due to the deliverance of dissolved sulfur species by dissolution of S^0.

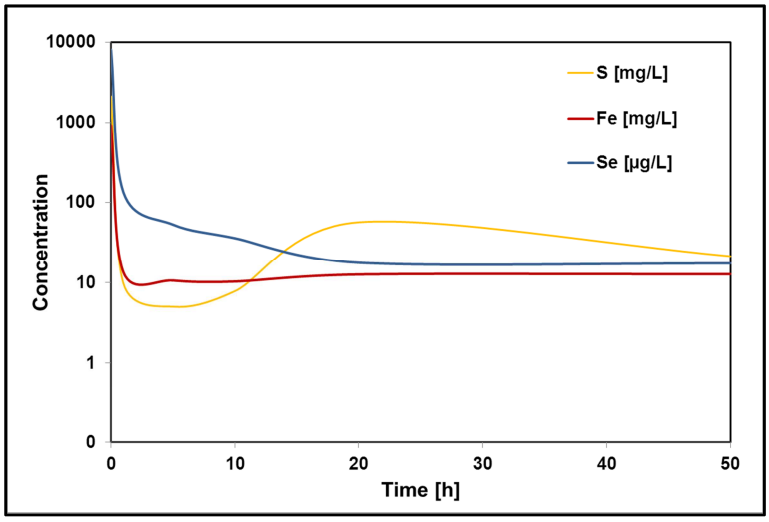

Fig. 5.13: Time-dependent concentration of S, Fe and Se in solution (y-axis in log-scale) at standard conditions and pH 4.5 for the instantaneous precipitation experiments. Initial concentrations: [S] = 0.066 M; [Fe] = 0.0175 M; $[Se^{2-}] = 10^{-4}$ M.

Kinetics of selenium uptake by pyrite in crystal growth experiments

The concentrations of dissolved Fe, S, Se were measured 1, 5, 10, 20, 50 and 120 hours after the start of the crystal growth experiments, containing once Se^{2-} and once Se^{4+}. The time-dependent development of the concentration of each element was very similar for both selenium coprecipitation experiments. The decrease of Se^{2-} concentration is only marginally higher than for Se^{4+}. Equilibrium of Se, S, and Fe in the solution was reached within a mean residence time of 15.8 h in the reactor (Fig. 5.14). The calculated growth of selenium doted pyrite was $1.7 \cdot 10^{-5}$ mol/L·h.

The results of the (rapid) decrease of the selenium concentration within the solution are similar for both, the instantaneous precipitation as described before, and the crystal growth experiment. The only significant difference is the time-dependent concentration of sulfur. This

is due to the lack of precipitated elemental sulfur in the crystal growth experiments, because the solution is undersaturated of S^0.

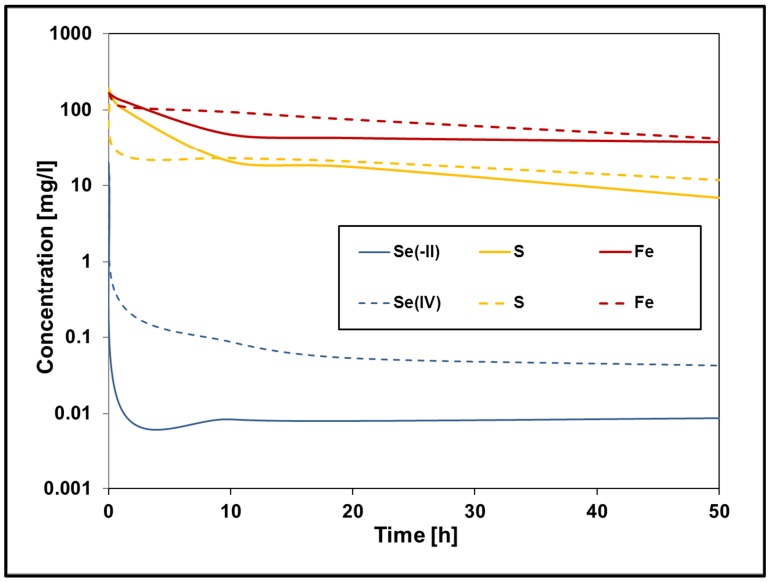

Fig. 5.14: Time-dependent concentration of S, Fe and Se^{2-} or Se^{4+} in solution during crystal growth experiments at standard conditions and pH 4. The continuous line represents Se^{2-} and the dashed line Se^{4+} residual contents. Initial concentrations: [S] = 10^{-3} M, [Fe] = $5 \cdot 10^{-4}$ M, [Se] = $2.5 \cdot 10^{-4}$ M.

5.4 Reference spectra of selenium oxidation states

The XAFS analyses were used to determine the solid-phase species of the selenium doted iron sulfide samples. The shape of the absorption edges of the Se doted samples were compared with known standards to reveal the oxidation state. To check the structural parameters of the selenium standards, the results were compared with publications (Tab. 5.11: Ryser et al, 2005; Charlet et al., 2007; Breynaert et al., 2008; Scheinost et al., 2008).

Tab. 5.11: Selected selenium standards of published XAS investigations (E_0 = absorption edge; CN = coordination number; R = atomic distance to the absorber; n.m.: not mentioned).

Standard	E_0	Shells				Literature
	[eV]	CN	R [Å]	CN	R [Å]	
Monoclinic Se^0	12658	2.2 Se	2.35			Ryser et al., 2005
$FeSe_2$	12657	3 Fe	2.38	1 Se	2.57	
		1 Se	3.05	10 Se	3.29	
Trigonal Se^0	n.m.	2.0 Se	2.39	4.8 Se	3.39	Charlet et al, 2007
		1.0 Se	3.74			
Tetragonal FeSe		3.8 Se	2.38	8.9 Se	3.70	
		2.1 Se	3.96	7.7 Fe	4.43	
Trigonal Se^0	n.m.	2.03 Se	2.37	4.05 Se	3.41	Breynaert et al., 2008
		2.02 Se	3.66	2.12 Se	4.14	
		3.88 Se	4.30	4.05 Se	4.47	
Trigonal Se^0	12656.1	2.2 Se	2.38	4.0 Se	3.39	Scheinost et al., 2008
		2.5 Se	3.73			
Ferroselite	12656.0	2.7 Fe	2.37	3.3 Se	3.30	
		0.6 Se	2.57	2.1 Se	3.55	

The XAFS-spectra of the standard compounds are shown in Figure 5.15. The differences in the intensity of the white line as well as in the overall shape of the normalized XANES spectrum between solid Na_2Se, gray elemental selenium, Na_2SeO_3, achavalite and ferroselite are clearly distinguishable. The k-edge of the Se^{2-} compounds is comparably flat to that of Se^{4+}. The XANES spectra of solid and dissolved Na_2Se and Na_2SeO_3 also show that the white line of the same oxidation state is highly similar, but at about 10 eV after the peak maximum, the curve shape varies because of the different backscattering atoms around the central absorbing selenium atom.

Because of the high amount of noise and low part of signal, the EXAFS spectrum of dissolved Na_2Se was only fitted until a q of 7.5 $Å^{-1}$. Unfortunately, ferroselite oxidized during the EXAFS measurements, making it impossible to distinguish its structure. The differences in the radial structure function (RSF) are due to their neighbors. For example, the first coordination shell in the RSF of Na_2SeO_3 is occupied by the tightly bonded oxygen atom. With respect to elemental selenium, the first atomic neighbor is selenium at a more far atomic distance.

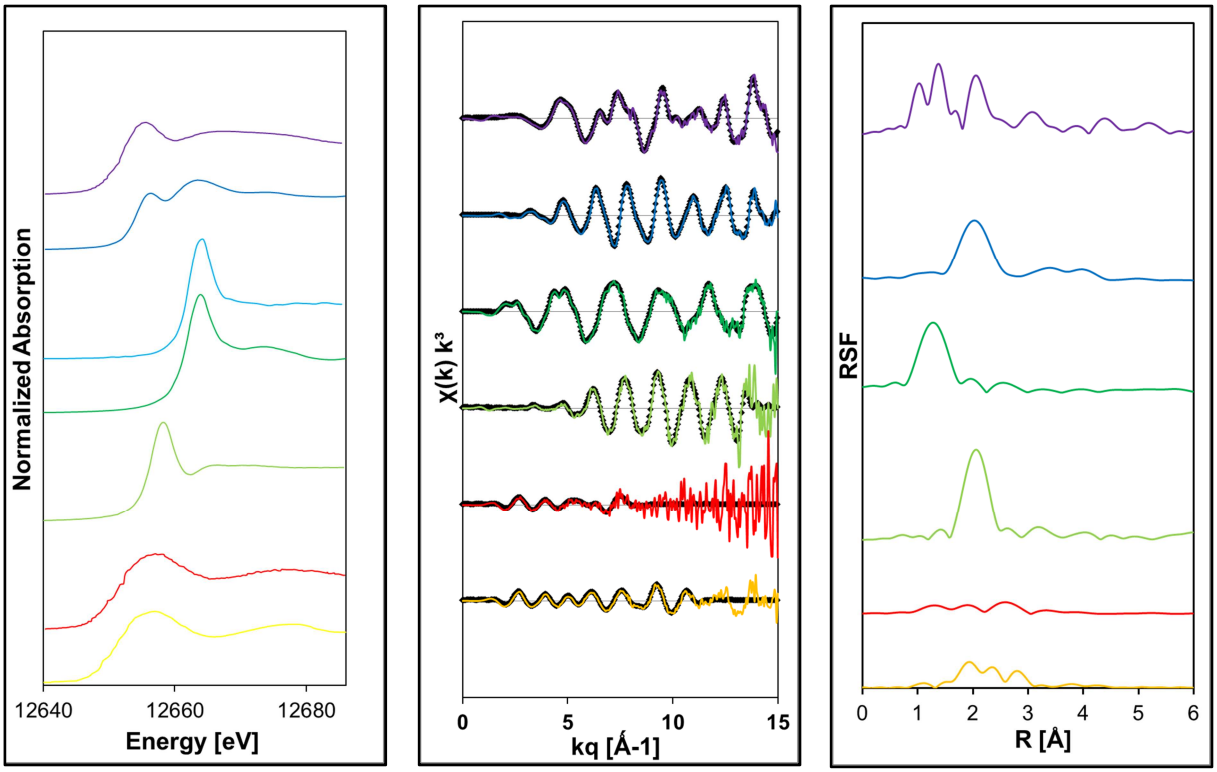

Fig. 5.15: XAFS-spectra of reference compounds containing XANES-spectra (left), kq-space (middle, k: colored line, q: black dots) and EXAFS-spectra (right). The reference compounds are: Na_2Se (yellow), Se^{2-} in solution (red), Se^0 (pale green), Na_2SeO_3 (dark green), Se^{4+} in solution (pale blue), achavalite (dark blue), ferroselite (violet).

The k-edge value of Se^0 is 12658.0 eV. This is ~1 eV higher than the E_0-value of the reduced valence states of selenium. Due to the selenium double-bonding in ferroselite, its oxidation state is –I and the E_0-value is 12656.7 eV. The peak of the white line of Se^{2-} in the form of Na_2Se is at 12656.8 eV, while the E_0-value of achavalite is 12656.5. The k-edge of Se^{4+} in Na_2SeO_3 (E_0: 12663 eV) is ~5 eV higher than that of Se^0. These analytical results are very similar to results cited in literature. Ryser et al. (2005) report an E_0 of 12664 eV for Se^{6+} (Na_2SeO_4). The E_0 of Se^{4+} (Na_2SeO_3) is 12662 eV, the k-edge of elemental selenium is at 12658 eV and for Se^- ($FeSe_2$) at 12657 eV. The selenium absorption edges reported by Scheinost et al. (2008) are generally lower with a value of about -2 eV. Referring to this study, the E_0-value of Se^{4+} (Na_2SeO_3) is 12660.7 eV, elemental selenium has an E_0-value of 12656.1 eV, Se^- (ferroselite) an E_0-value of 12656.0 eV and Se^{2-} (FeSe) an E_0-value of

12655.5 eV. All these values show that there is a clear difference in the k-edge values between the oxidized selenium valence states (Se^{6+}, Se^{4+}) and the reduced species (Se^0, Se^{2-}). A further determination of the exact reduced valence state of Se^{2-}, Se^- and Se^0 only on the basis of the absorption edge value has to be done with care, because the difference in E_0 is only between 0 and 1 eV. Hence, the identification of the Se oxidation state is more reliable by a comparison of the sample with the well distinguishable curve shapes of the selenium standards. The XANES-spectra of Figure 5.15 are in accordance with the published data from literature in Appendix B (Ryser et al, 2005; Charlet et al., 2007; Breynaert et al., 2008; Scheinost et al., 2008).

The fitted structural parameters from XAFS analysis for trigonal Se^0 and achavalite are presented in Table 5.12. The coordination shell of Se^0 is selenium, located at 2.36 Å and containing a coordination number of 1.96. This is in high agreement with the reported results (Tab. 5.11). In three publications (Charlet et al., 2007; Breynaert et al., 2008; Scheinost et al., 2008), the Se coordination shell obtained a coordination number between 2.0 and 2.2 at an atomic distance of 2.37 – 2.39 Å. The own detected selenium backscatterers are at an atomic distance of 3.32 Å and 3.72 Å, similar to the reported data of 3.39 – 3.41 Å for the second and 3.66 – 3.74 Å for the third atomic selenium neighbor.

Tab. 5.12: Fitted structural parameters from XAFS analysis for references. Accuracies of fitted structural parameters are noted in the brackets as uncertainties of the last digit (E_0 = absorption edge; CN = coordination number; R = atomic distance to the absorber; σ^2 = Debye-Waller factor; ΔE_0 = energy shift).

Reference	Coordination shell				Further shells				
	E_0 [eV]	CN	R [Å]	σ^2 [Å²]	CN	R [Å]	σ^2 [Å²]	ΔE_0 [eV]	R-factor
Se^0 - trigonal	**12658**	**1.96 Se (4)**	**2.36 (0)**	**0.0036 (1)**	**0.95 Se (28)**	**3.32 (2)**	**0.0135 (3)**	**9.8 (3)**	**0.008**
					0.32 Se (6)	**3.72 (1)**	**0.0016 (1)**		
Achavalite	**12656.5**	**2.68 Fe (6)**	**2.55 (0)**	**0.0027 (2)**	**1.90 Se (16)**	**3.66 (0)**	**0.0033 (5)**	**5.5 (3)**	**0.005**
					5.56 Fe (64)	**4.45 (1)**	**0.0148 (1)**		

The determined structure of achavalite shows an iron neighbor at 2.55 Å with a coordination number of 2.68. Further backscatters of the selenium absorber are located at 3.66 Å (Se)

and 4.45 Å (Fe). Due to the lack of comparable XAFS-analysis, the structural data for comparison of achavalite were taken from Wyckhoff (1963). There are two iron backscatterers at 2.574 Å and 4.456 Å noted and one selenium neighbor at 3.645. This is in good agreement with the data presented here.

The quality of the fit parameters is good, because the R-factor is below 0.01 and the shift of energy below 10 eV, the Debye-Waller factors are in the desired range of 0.001 – 0.015. Typical for the XAFS parameter (CN, R, σ^2) is the often rising uncertainty with rising distance from the absorber, which can be seen in Table 5.12 especially for the coordination numbers.

5.5 Structure of selenium doted mackinawite and pyrite

Determination of the surface structure of Se doted pyrite and mackinawite

The XP spectra (Fig. 5.16) show a comparison of Se^{2-} doted pyrite with Se^0. The photoelectron elemental lines of Se are superimposed by intense photoelectron elemental lines of the main constituents S and Fe, making it impossible to distinguish their binding energies. Solely, X-ray excited Auger transitions of selenium are detectable with low intensity, which can be used for interpretation.

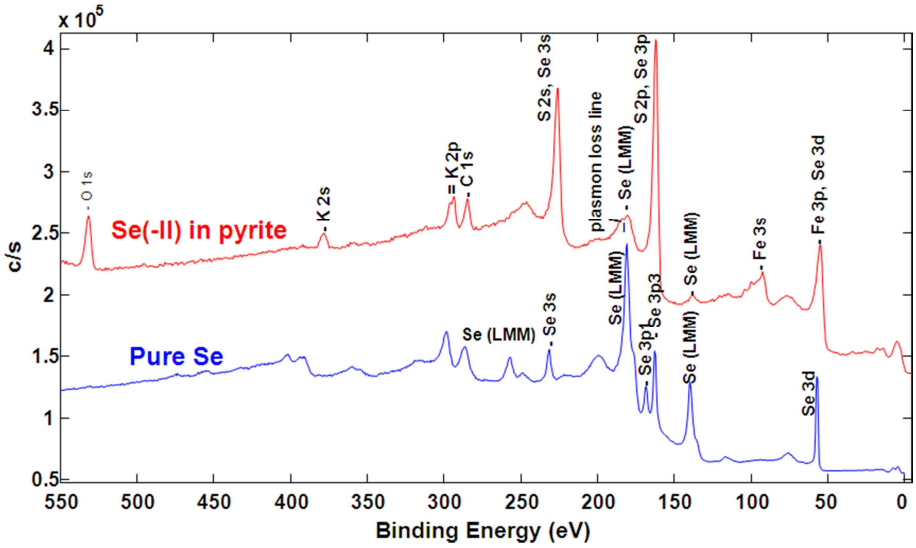

Fig. 5.16: XP spectra of Selenium doted iron sulfides showing the low binding energy range of survey spectra of pure selenium for comparison. In case of Se^{2-} doted pyrite, the photoelectron elemental lines of Se are superposed by the intense photoelectron elemental lines of either S or Fe.

The narrow scans of Se $L_3M_{45}M_{45}$ Auger lines (Fig. 5.17) are superposed by the plasmon loss lines of S 2p with maxima at a binding energy of 183 eV. The kinetic energies of the Se $L_3M_{45}M_{45}$ Auger electrons, between 1305 and 1307 eV, are characteristic for reduced valence states of selenium (Moulder et al., 1992). Finally, XP spectra indicate that the selenium valence states of all experiments were reduced, lying between Se^0 and Se^{2-}. However, the Se^{2-} binding partner could not be identified, but is presumably Fe^{2+}.

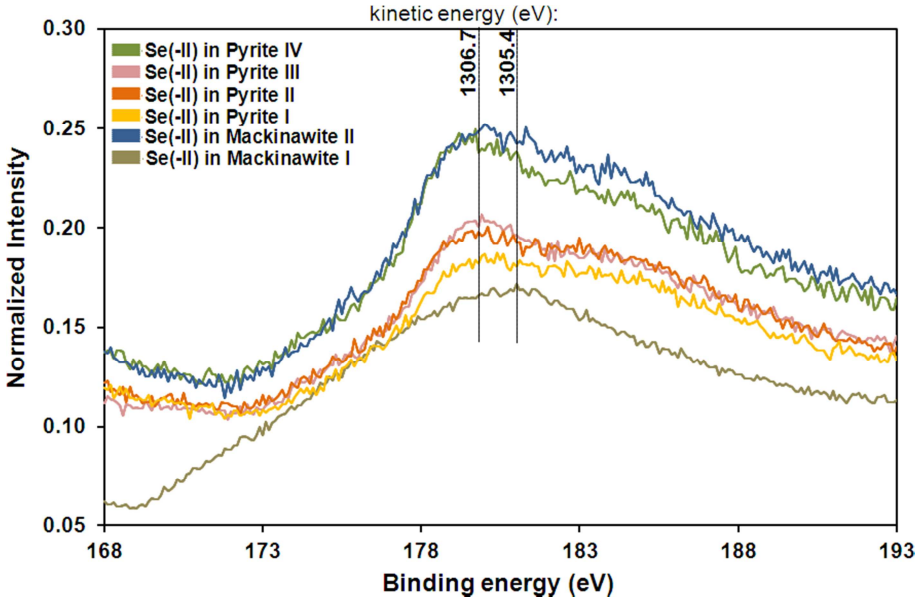

Fig. 5.17: XP-spectra of selenium doted iron sulfides. The narrow scans of Se LMM are normalized with respect to the nearby S 2p spectrum at the lower binding energy side. Between the two, black vertical lines are the reduced valence states of selenium (0,-I,-II). The abbreviation of the index within the figure names the initial valence state of selenium in solution and not the actually oxidation state of Se in the sample.

Mackinawite

The XAFS results of the instantaneous precipitation experiments (Ch. 4.1; Tab. 5.1 and 5.2) with regard to Se incorporation into mackinawite with Se^{4+} initially present in the solution, indicate a complete reduction of Se^{4+} to Se^0 (Fig. 5.18). The XANES spectrum is very similar to the trigonal Se^0 spectrum. For fitting the experimental EXAFS spectrum, several selenium shells were considered. This suggests the incorporation of selenium in an amorphous Se^0-type environment with approximately six selenium neighbors in the coordination shell at a

distance of 2.31 Å (Tab. 5.13). The limited number of detected selenium atomic neighbors indicates a small cluster size.

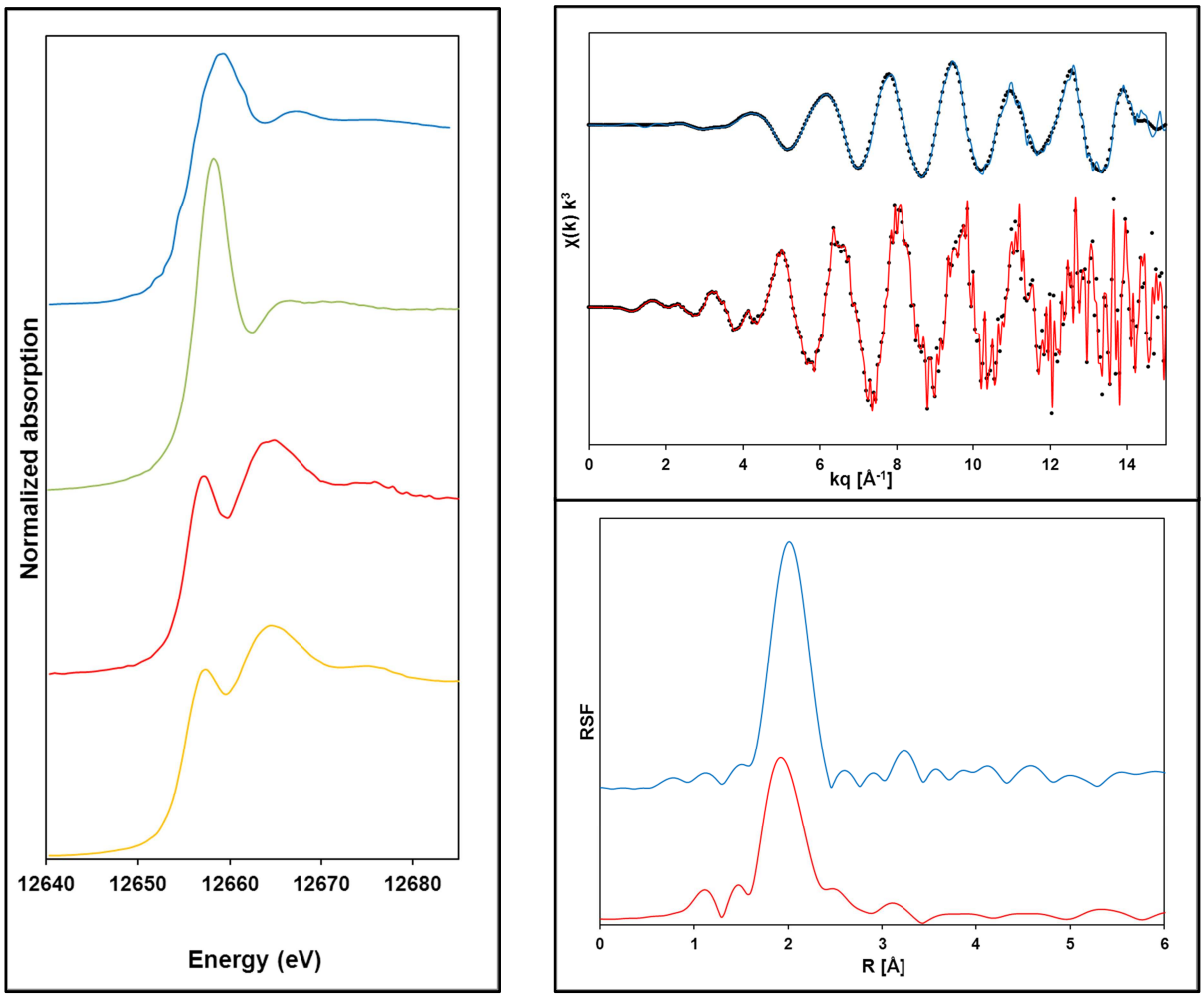

Fig. 5.18: XAFS-spectra of selenium doted mackinawite containing XANES-spectra (left), kq-space (middle, k: colored lines, q: black symbol) and R-space (right). Achavalite (yellow); Se incorporation in mackinawite with initial dissolved Se^{2-} (red); elemental selenium (green); Se incorporation in mackinawite with initial dissolved Se^{4+} (blue).

The XANES spectrum of Se doted mackinawite using dissolved Se^{2-} (E_0: 12656.8 eV) is very similar to that of achavalite (E_0: 12656.5 eV; for comparison of achavalite XANES-spectra: Charlet et al., 2007; Scheinost et al. 2008; both in Appendix B), implying a valence state of -II (Fig 5.18). The first Fe shell is located at a distance of 2.37 Å, followed by two sulfur neighbors at 3.5 Å and 3.68 Å and one iron neighbor at 4.25 Å, suggesting a replacement of

sulfur by selenium in a mackinawite-like environment (Fig. 5.19) while the changes in crystal structure can be compared with mackinawite structure (Fig. 2.5).

Tab. 5.13: Fitted structural parameters from XAFS coprecipitation experiments with selenium doted mackinawite showing the initially used dissolved Se species. Accuracies of fitted structural parameters are noted in the brackets as uncertainties of the last digit (E_0 = absorption edge; CN = coordination number; R = atomic distance to the absorber; σ^2 = Debye-Waller factor; ΔE_0 = energy shift).

Sample	Coordination shell				Further shells				
	E_0 [eV]	CN	R [Å]	σ^2 [Å²]	CN	R [Å]	σ^2 [Å²]	ΔE_0 [eV]	R-factor
Se^{2-} - Mack.	12656.8	1.26 Fe (13)	2.37 (0)	0.0017 (4)	1.68 S (51)	3.50 (7)	0.0045 (11)	-2.1 (12)	0.016
					1.17 S (73)	3.68 (6)	0.0129 (10)		
					0.90 Fe (61)	4.25 (5)	0.0094 (50)		
Se^{4+} - Mack.	12657.5	6.08 Se (16)	2.31 (0)	0.0098 (2)	0.90 Se (21)	2.57 (2)	0.0102 (18)	13.7 (0)	0.004

The values and uncertainties of the structural parameters R and σ^2 for fitting the Se doted mackinawite using dissolved Se^{2-} are appropriate (Tab. 5.13). The uncertainties of the coordination number after the coordination shell are relatively high, which may be due to the relative low amount of incorporated selenium (0.09 mol%). The fitting parameters of Se doted mackinawite with initially Se^{4+} present in solution are generally good, as it is expressed by the very low value of 0.004 for the residual of fit. Only the shift of energy parameter ΔE_0 is slightly high. This value is used to align the theoretical calculated spectrum to the energy grid of the measured spectrum.

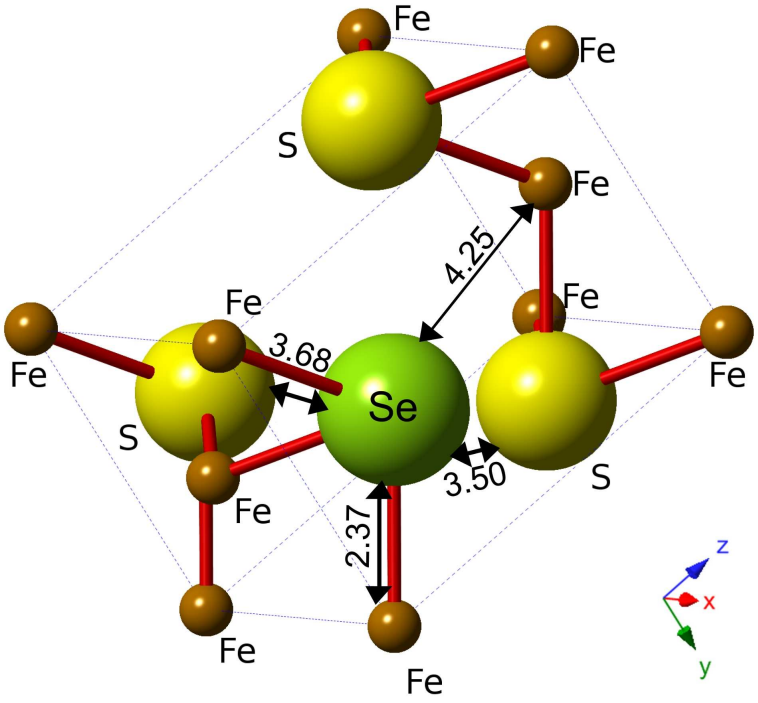

Fig. 5.19: The crystal model illustrates the EXAFS-results, showing selenium doted mackinawite with initially dissolved Se^{2-} in solution. Se^{2-} is substituting S^{2-} in the crystal lattice, resulting in small shifts towards xyz-axis, Distances are given in Å.

Reaction pathway of selenium incorporation in mackinawite

The conclusion of the XAFS results with the proposed phases and species of the thermodynamical calculations may indicate the probable reaction pathway leading to the incorporation of selenium in a certain oxidation state. With regard to the incorporation of Se into mackinawite using dissolved Se^{2-}, the species Fe^{2+}, $Fe(HS)_2$, HS^-, H_2S, HSe^- are predominantly present in solution (Tab. 5.1). Dissolved $Fe(HS)_2$ is a complex which is built during the intermediate reaction steps for mackinawite formation via HS^- (Ch. 2.3.4). Hence, it is likely that Fe^{2+} reacts with HS^- and H_2S to form mackinawite (Eq. 2.4 and 2.5). The XAFS investigations lead to the conclusion that a substitution of S^{2-} by Se^{2-} occurred. Therefore, since HSe^- is the dominant selenide species in solution, the proposed reaction leading to the incorporation of Se^{2-} is (Eq. 5.3):

$$Fe^{2+}_{(aq)} + HSe^-_{(aq)} \leftrightarrows FeSe_{(s)} + H^+ \qquad (5.3).$$

The precipitated phases of the thermodynamical calculations are different to the analytical results. The calculations predict that mainly pyrite, Se^0 and to a lower amount mackinawite precipitate from the solution in equilibrium, though the solution was also oversaturated with respect to all considered iron-selenium phases. The question is, why are the results between thermodynamical calculations and XAFS analysis not equal?

The reason why mackinawite instead of pyrite does precipitate from the solution is related to kinetics (Rickard and Luther, 2007). Mackinawite is metastable under standard conditions and would dissolve and re-precipitate as pyrite after a certain time-period which could take months to years (Ch. 2.3.4). The detected substitution of S^{2-} by Se^{2-} instead of the precipitation of Se^0 is probably also due to kinetic reasons. In the laboratory experiments, the precipitation of mackinawite occurs instantaneously after mixing. In fact, the most stable species of selenium under these hydrochemical conditions is Se^0. Only the rapid formation of mackinawite of these highly supersaturated solution leads to the incorporation of selenide, accompanied with the structural substitution of sulfur by selenium.

With respect to the Se doted mackinawite with initially dissolved Se^{4+} in the solution, the calculated dominating dissolved initial species were HS^-, H_2S, Fe^{2+}, $Fe(HS)_2$, $HSeO_3^-$ and SeO_3^{2-} (Tab. 5.2). The predicted phases with the solution being in equilibrium are mackinawite, pyrite and Se^0. As mentioned in the paragraph before, the lack of pyrite is probably due to kinetic reasons. The difference to the batch experiment with selenide is the direct reduction of selenite in the solution, which occurs probably concomitantly with the oxidation of sulfide. The reaction can be described by the equation 5.4:

$$HSeO_3^-{}_{(aq)} + H_2S_{(aq)} + 2e^- \leftrightarrows Se_{(s)} + S_{(s)} + H_3O^+ + O_2^{4-} \qquad (5.4).$$

This observation is in agreement with Bruggeman et al. (2005) and Breynaert et al. (2009), who detected a Se^{4+} reduction to Se^0 on the pyrite surface.

Structure of Se doted pyrite with initially dissolved Se^{4+}

Both, instantaneous precipitation experiments with regard to Se incorporation into pyrite using initially dissolved Se^{4+} (Ch. 4.1; Tab. 5.4) as well as crystal growth experiments with respect to the examination of Se coprecipitation into pyrite with dissolved Se^{4+} (Ch. 4.2; Tab. 5.6) indicate a complete reduction of Se^{4+} to Se^0 (Fig. 5.20). Their XANES spectra are very similar to the trigonal Se^0 spectra and to those of Se^0 published in the literature (Appendix B). For fitting the experimental EXAFS spectra, several selenium shells were considered. This suggests the incorporation of selenium in an amorphous Se^0-type environment with a first neighbor in the coordination shell at ~2.3 Å with a coordination number between 2 and 3 (Tab. 5.14). A further Se neighbor was distinguished at a distance ~3.55 Å. The limited number of detected Se atomic neighbors indicates a small cluster size. The structural parameters shown in Table 5.16 are overall reasonable.

Tab. 5.14: Fitted structural parameters from XAFS incorporation experiments of Se doted pyrite with Se^{4+} initially present in solution. Accuracies of fitted structural parameters are noted in the brackets as uncertainties of the last digit (E_0 = absorption edge; CN = coordination number; R = atomic distance to the absorber; σ^2 = Debye-Waller factor; ΔE_0 = energy shift).

Sample	Coordination shell				Further shells				
	E_0 [eV]	CN	R [Å]	σ^2 [Å²]	CN	R [Å]	σ^2 [Å²]	ΔE_0 [eV]	R-factor
Initial Precipitat.	12658.2	3.00 Se (28)	2.29 (1)	0.0073 (6)	1.83 Se (3)	3.63 (9)	0.0067 (19)	-7.2 (7)	0.010
Crystal growth	12658.4	2.16 Se (19)	2.32 (1)	0.0057 (5)	1.50 Se (30)	3.50 (4)	0.0128 (7)	4.5 (14)	0.018

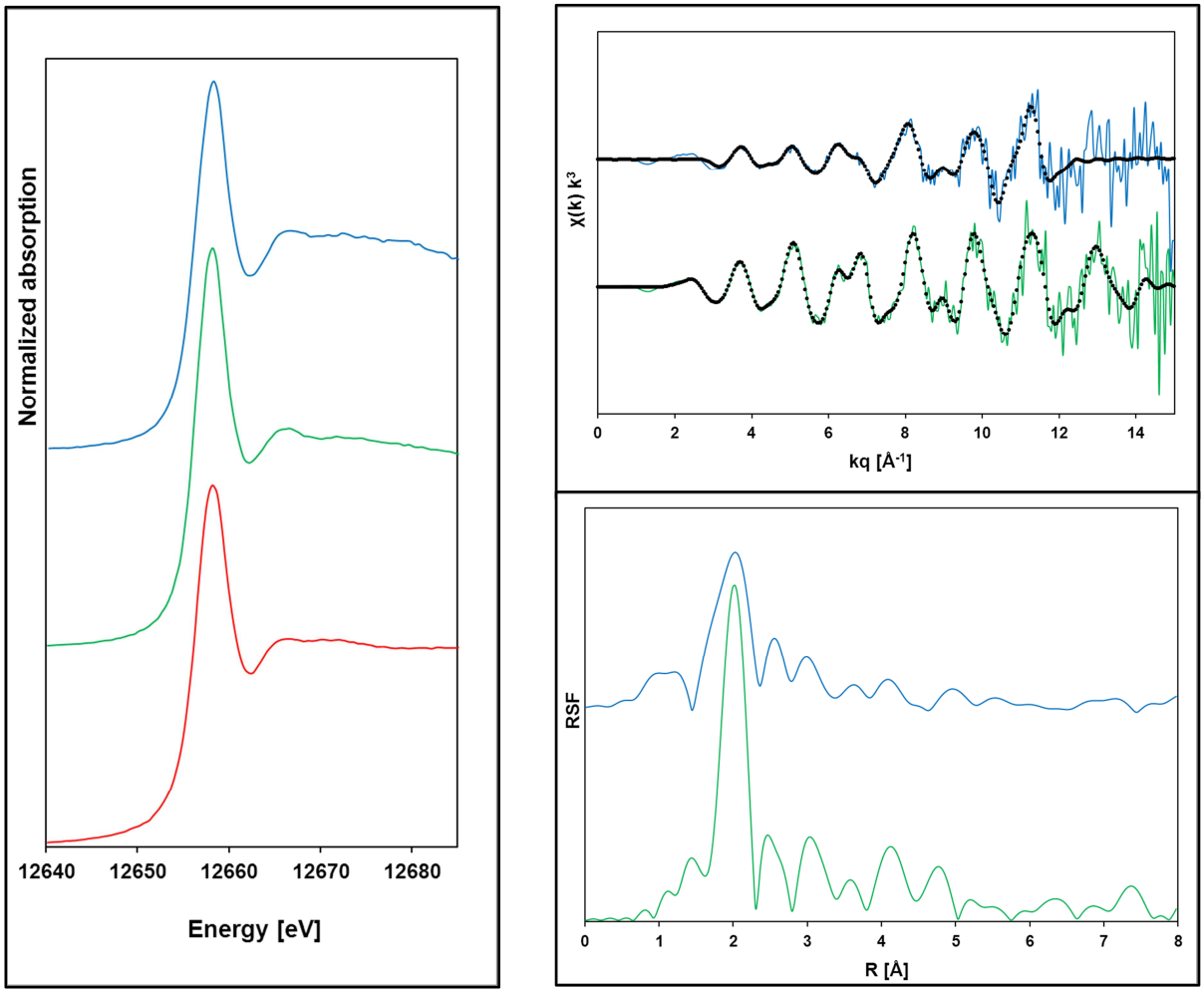

Fig. 5.20: XAFS-spectra of selenium doted pyrite with initial dissolved Se^{4+} containing XANES-spectra (left), kq-space (up right, k: colored lines, q: black symbol) and R-space (down right). Elemental selenium reference spectra (red); Se incorporation in pyrite with initially dissolved Se^{4+} by instantaneous precipitation experiments (green); Se incorporation in pyrite of initially dissolved Se^{4+} by crystal growth experiments (blue).

Reaction pathway of Se incorporation into pyrite with initially dissolved selenite

The synopsis of spectroscopic investigations and the thermodynamical calculations concerning the reaction pathway of Se doted pyrite using Se^{4+} shows coinciding results. The XAFS investigations of the precipitates of batch and MFR-experiments have in common that a reduction of Se^{4+} to Se^{0} occurred during the incorporation. The calculated most important species occurring in solution in the batch-doting experiments are $Fe(HS)_2$, Fe^{2+}, H_2S, $HSeO3^-$ and H_2SeO_3 (Tab. 5.4). Since the polysulfides are much less concentrated than H_2S, it is

assumed that the pyrite precipitation follows mainly the Berzelius pathway (Ch. 2.3.4). Although the solution is oversaturated with respect to pyrite, mackinawite, S^0, Se^0, ferroselite, achavalite and FeSSe, only pyrite and Se^0 precipitate. The predominant dissolved species in the solution for crystal growth-doting experiments are H_2S, Fe^{2+} and $HSeO_3^-$ (Tab. 5.6). Again, the predicted precipitations of the minerals are pyrite and Se^0. To sum up, the XAFS-results are consistent with those achieved from thermodynamic calculations. In accordance to equation 5.3, a reduction of Se^{4+} to Se^0 is likely to take place concurrent with the oxidation of dissolved sulfide species.

Structure of Se doted pyrite with initially dissolved Se^{2-}

The Se doted pyrite using dissolved Se^{2-} (E_0: 12657.1 eV) XANES curve progression in the instantaneous precipitation experiment (Ch. 4.1; Tab. 5.3) is similar to those of ferroselite (E_0: 12656.8 eV; for comparison: Scheinost et al., 2008 in Appendix B), showing a valence state of –I (Fig. 5.21). The distance of 2.21 Å between selenium and sulfur (CN ~1) in the first shell corresponds to the short S-S distance (2.16 Å) in pyrite. The iron neighbor at 2.35 Å as well as following iron and sulfur shells indicate a substitution of S by Se in selenide doted pyrite, yielding in a FeS_xSe_y compound which may be described best by a slightly distorted pyrite structure (Fig. 5.22). The structural parameters as well as their uncertainties suggest a good fit of the EXAFS spectrum.

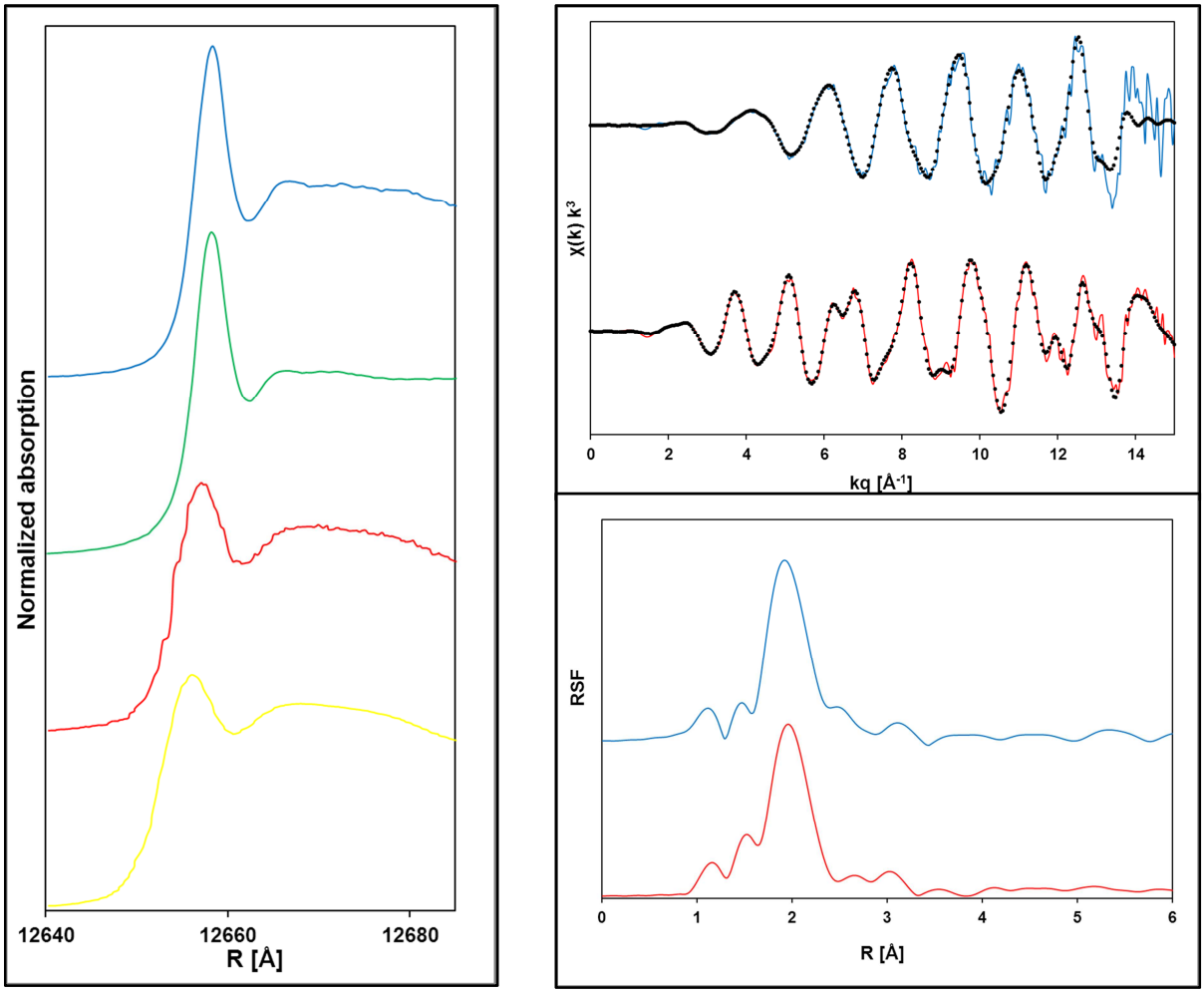

Fig. 5.21: XAFS-spectra of samples of Se incorporation in pyrite with initially dissolved Se^{2-} containing XANES-spectra (left), kq-space (up right, k: colored lines, q: black symbols) and R-space (down right). Se^{2-} reference spectra (yellow); Se incorporation in pyrite with initially dissolved Se^{2-} by instantaneous precipitation experiments (red); Se^{0} reference (green); Se incorporation in pyrite with initially dissolved Se^{2-} by crystal growth experiments (blue).

The differences in the crystal structure of the selenium doted pyrite compared to natural pyrite can be compared (Fig. 2.5). As discussed earlier, the formation of pyrite under standard conditions follows a dissolution-precipitation pathway, with mackinawite as mainly participating precursor phase (Ch. 2.3.4). In this regard, it is important to note that the initially dissolved selenide is first of all incorporated as Se^{2-} into mackinawite, followed by the dissolution of mackinawite and the release of Se. Finally, selenium was incorporated as Se^{-} into pyrite. If mackinawite dissolves, the FeS transition intermediate $Fe(HS)_2$ forms as

necessary precursor for the pyrite formation in the Berzelius reaction. Hence, it is likely that selenide does not oxidize as predicted in the thermodynamic calculations (Ch. 5.1), because it is bound as $Fe(HSe)_2$ cluster, preventing selenide from oxidation.

XANES spectra of Se incorporated into pyrite using dissolved Se^{2-} in crystal growth experiments (Ch. 4.2; Tab. 5.5) show a predominant oxidation of Se^{2-} to Se^0, and the k-edge of 12658.3 eV as well as the curve progression corresponds to Se^0 reference. Different Se shells with Se in the first shell at a distance of 2.29 Å (CN ~2) imply the presence of Se^0. A sulfur neighbor at the short distance of ~2.2 Å was not identified. The small number of detected atomic selenium neighbors suggests a small cluster size (Tab. 5.15).

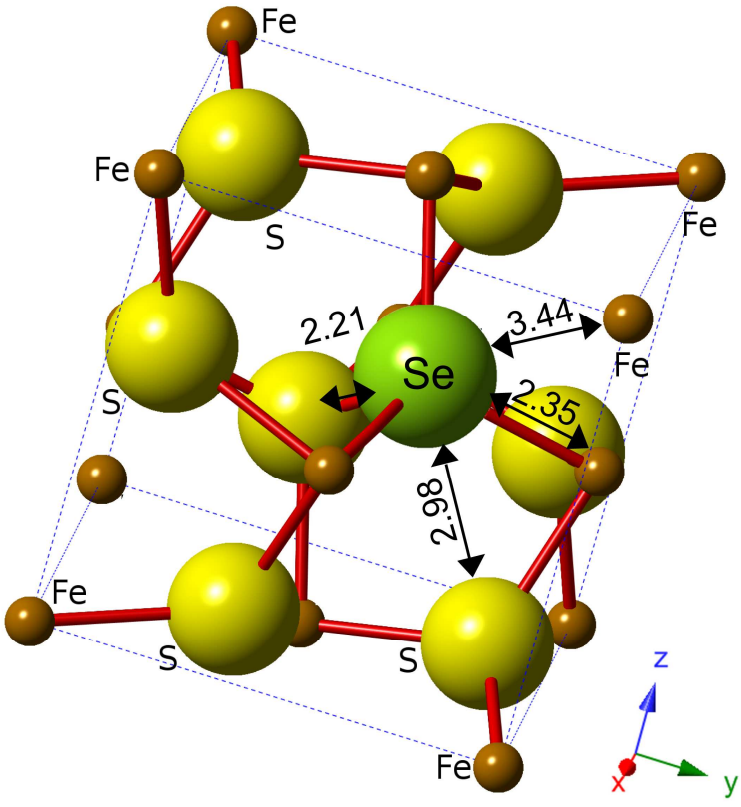

Fig. 5.22: The crystal model illustrates the EXAFS-results of the instantaneous precipitation experiments, showing Se doted pyrite with initially dissolved Se^{2-} in solution. Se^- is substituting S^- in the crystal lattice, resulting in small shifts towards xyz-axis, Distances are given in Å.

The changing valence states of Se^{2-} to Se^0 in crystal growth experiments are in good agreement with sorption studies showing that Se^{2-} is oxidized to Se^0 under acidic conditions (Liu et al., 2008). XAFS results are also consistent with the modeled predominant field valence state of incorporated selenium into pyrite.

Tab. 5.15: Fitted structural parameters from XAFS incorporation experiments of Se doted pyrite with Se^{2-} initially present in solution. Accuracies of fitted structural parameters are noted in the brackets as uncertainties of the last digit (E_0 = absorption edge; CN = coordination number; R = atomic distance to the absorber; σ^2 = Debye-Waller factor; ΔE_0 = energy shift).

Sample	Coordination shell				Further shells				
	E_0 [eV]	CN	R [Å]	σ^2 [Å²]	CN	R [Å]	σ^2 [Å²]	ΔE_0 [eV]	R-factor
Initial Precipitat.	**12657.1**	**0.97 S (14)**	**2.21 (1)**	**0.0080 (20)**	**1.25 Fe (6)**	**2.35 (0)**	**0.0016 (3)**	**2.8 (8)**	**0.010**
					0.36 S (15)	**2.98 (2)**	**0.0099 (61)**		
					0.66 Fe (26)	**3.44 (3)**	**0.0054 (34)**		
					0.90 S (50)	**3.87 (5)**	**0.0118 (45)**		
Crystal growth	**12658.3**	**1.99 Se (13)**	**2.29 (1)**	**0.0015 (2)**	**1.19 Se (32)**	**3.55 (3)**	**0.0070 (16)**	**6.6 (12)**	**0.015**

Reaction pathway of Se incorporation into pyrite with initially dissolved selenide

The XAFS results of the Se doted pyrite experiments using aqueous Se^{2-} are inconsistent. In the highly supersaturated solutions accompanied with an instantaneous precipitation, the incorporated selenium does substitute sulfur and forms a FeS_xSe_y-compound. The reaction leading to the precipitation of such a solid solution could be described as in equation 5.5:

$$Fe^{2+}_{(aq)} + HS^-_{(aq)} + HSe^-_{(aq)} \rightarrow FeSSe_{(s)} + H_{2(g)} \quad (5.5).$$

The thermodynamic calculations show that the dissolved species initially present in the solution before the reaction are H_2S, $Fe(HS)_2$, Fe^{2+}, HSe^-, and H_2Se (Tab. 5.3). Again, mainly monosulfidic species apart from the $Fe(HS)_2$ cluster are present in the solution. Hence, it is probable that the Berzelius pathway is dominating for the formation of pyrite. The solution is oversaturated with regard to pyrite, mackinawite, Se^0, ferroselite, achavalite and the solid solution phase FeSSe. The calculated phases precipitating from solution are pyrite ($1.73 \cdot 10^{-2}$ M) and Se^0 ($1 \cdot 10^{-3}$ M).

On the contrary, the spectroscopic investigations of the Se doted pyrite with initially Se^{2-} present in the solution in crystal growth experiments point out, that Se^0 becomes incorporated into the pyrite structure. This is in agreement with the thermodynamic results for both, the instantaneous precipitation as well as for the crystal growth experiments. Calculating the equilibrium of the solution, the results show that only pyrite and elemental selenium precipitate (Tab. 5.5). Though the solution is oversaturated with regard to elemental selenium, ferroselite and the FeSSe solid solution, the calculations predict that the whole initial amount of dissolved Se^{2-} precipitates as Se^0 and not as iron selenide compound (e.g. ferroselite, FeSSe).

The XAFS results show that both types of the structural incorporation of Se^{2-} into pyrite are generally possible. It is likely that the kinetic of pyrite precipitation is the controlling factor if Se^{2-} is incorporated as Se^- or as Se^0, because the precipitation of mackinawite as pyrite precursor phase takes place instantaneously after mixing of the separated S, Se, Fe solutions. The kinetic itself is controlled by the concentrations of the initial reactants and the extent of supersaturation with regard to the respective mineral phases. A summary of the aqueous selenium dotation experiments together with the results of the thermodynamic calculations is shown in Tab. 5.16.

Tab. 5.16: Summary of the aqueous Se doted iron sulfide experiments and the thermodynamical calculations showing the initial Se valence state in solution, the type of experiment and the determined incorporated Se valence state.

Synthesized mineral and initial valence state in solution	Instantaneous precipitation	Crystal growth	Thermodynamical calculations
Mackinawite and Se^{2-}	Incorporation of Se^{2-} Substitution of S by Se	Not determined	Precipitation of Se^0, Pyrite, Mackinawite
Mackinawite and Se^{4+}	Incorporation of Se^0 Reduction of Se^{4+}	Not determined	Precipitation of Se^0, Pyrite, Mackinawite
Pyrite and Se^{2-}	Incorporation of Se^{2-} Substitution of S by Se	Incorporation of Se^0 Oxidation of Se^{2-}	Precipitation of Se^0, Pyrite
Pyrite and Se^{4+}	Incorporation of Se^0 Reduction of Se^{4+}	Incorporation of Se^0 Reduction of Se^{4+}	Precipitation of Se^0, Pyrite

On the basis of the results, the conceptual model of initially dissolved Se^{4+} present in the solution under standard anoxic and acidic conditions expects Se^0 to become predominantly incorporated into pyrite and mackinawite. With regard to the incorporation by using Se^{2-} in solution, generally both, the substitution of S by Se in pyrite and mackinawite as well as the oxidation of Se^{2-} to Se^0 are possible. The type of Se oxidation state depends on the kinetics. Finally, the structural fixture of Se into iron sulfides by substitution of S and the precipitation of highly insoluble Se^0 (~10^{-9} M) fixed in iron sulfides within multi-barriers of a HLW repository are promising, because this would significantly decrease the Se mobility.

Selenium doted pyrite condensed from gaseous phase

The XANES reference spectra (trigonal Se^0, Na_2Se) as fingerprint were compared with the XANES spectra of the sample (Ch. 4.3) to determine its selenium valence state (Fig. 5.23). The k-edge value of Se^0 as a reference for energy calibration (E_0: ~12658 eV) is ~1 eV higher than the reduced valence state Se^{2-} in the form of Na_2Se (E_0: 12656.8 eV). The XANES spectra of selenium incorporated into pyrite is similar to the valence state of elemental Se^0. The curve shape is very similar to the Se^0-XANES spectra and the k-edge is 12657.6 eV (Tab. 5.17), indicating that incorporated selenium is zero-valent.

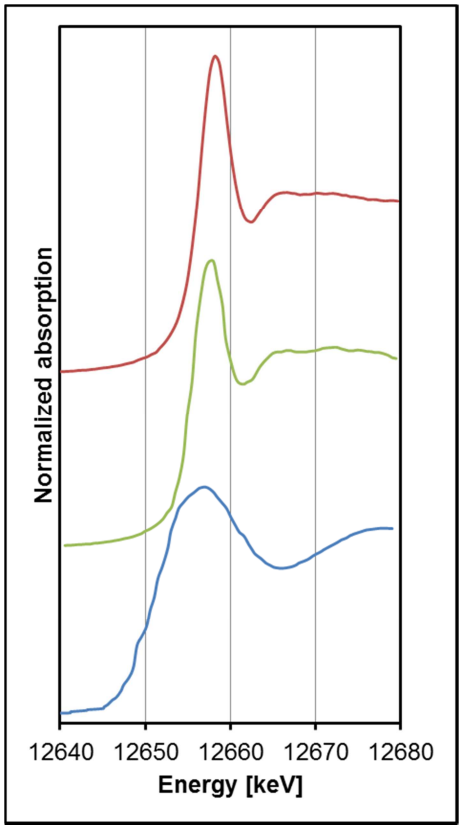

Fig. 5.23: XANES spectra of 1.) Na_2Se (blue), 2.) Se doted pyrite, synthesized by CVT (green), 3.) Se^0 (red).

Tab. 5.17: Fitted structural parameters of the condensation from gaseous phase experiment of selenium doted pyrite. Accuracies of fitted structural parameters are noted in the brackets as uncertainties of the last digit (E_0 = absorption edge; CN = coordination number; R = atomic distance to the absorber; σ^2 = Debye-Waller factor; ΔE_0 = energy shift).

Sample	Coordination shell				Further shells				
	E_0 [eV]	CN	R [Å]	σ^2 [Å²]	CN	R [Å]	σ^2 [Å²]	ΔE_0 [eV]	R-factor
Se^0 pyrite	12657.6	2.1 Se (2)	2.38 (0)	0.0085 (3)	3.0 S (2)	2.96 (0)	0.0038 (6)	-1.8 (3)	0.011
					1.8 Se (1)	3.42 (0)	0.0078 (3)		

The Se^0 incorporation into pyrite by condensation from gaseous phase is also shown by EXAFS investigations (Fig. 5.24). Several selenium shells were considered for fitting experimental data and this result suggests the incorporation of Se in a crystalline Se^0-type environment with selenium neighbor in coordination shells at 2.38 Å and 3.42 Å (Tab. 5.17).

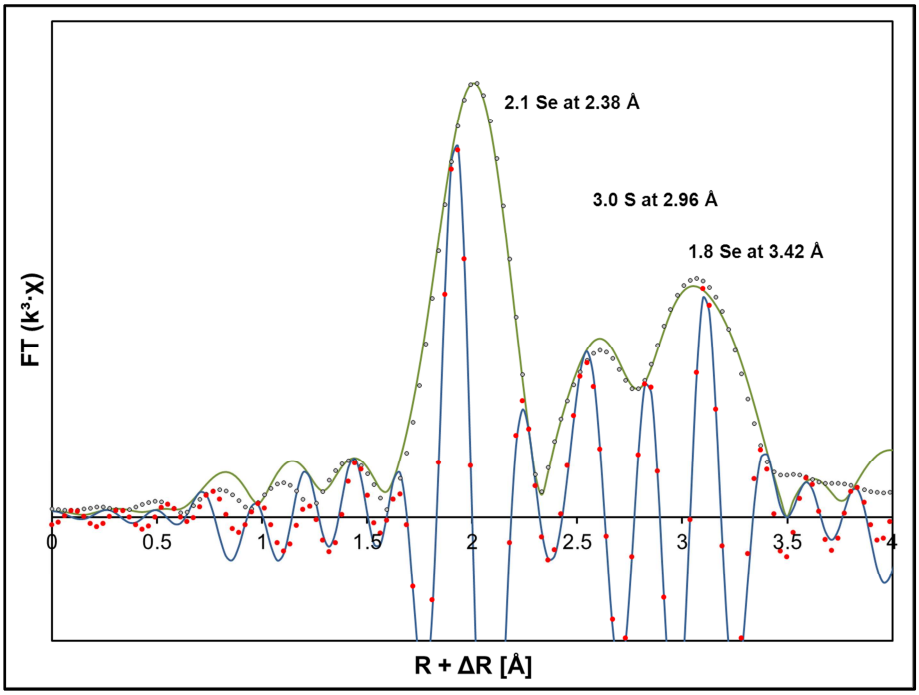

Fig. 5.24: EXAFS spectra of selenium doted pyrite showing the noted atomic neighbors of selenium together with the coordination number and atomic distance in Å. The figure shows four spectra (two for [Chi(R)] and two for Re[Chi(R)]), whereas the lines are representative for the sample, the dots for the fit. Accuracy of fitted structural parameters: Coordination number ± 25%, radial distance ± 0.01 Å, Debye-Waller-factor ± 0.00005 $Å^2$.

The detected sulfur neighbor at 2.96 Å belongs to the small amount of the SeS-compound, which forms after pyrite single crystal formation is finished due to the lack of further iron supply (Ch. 5.2). Neither Fe neighbors could be detected, nor the first S neighbor at 2.14 Å, which is the spatial distance for the double bonding of sulfur in pyrite. The structural parameters of the sample are good. The shift of energy is very low, as well as the uncertainties.

Altogether, XAFS analysis indicates that no remarkable substitution of S by Se in pyrite occurs during synthesis. Therefore, it is proposed that following reaction (Eq. 5.6) takes place, leading to the condensation of Se^0 in pyrite:

$$FeBr_{2(g)} + H_{2(g)} + X_2\ (X = S, Se)_{(g)} \rightarrow FeS_{2(s)} + Se^0_{(s)} + 2\ HBr_{(g)} \qquad (5.6).$$

The reason for Se^0 being incorporated instead of Se^- or Se^{2-} may be the high boiling point of Se^0 at 685°C. It is well possible that gaseous selenium does condensate before it reacts with iron at the cooler side of the quartz vessel. Hence, it may be difficult to synthesize selenium doted pyrites with selenium substituting sulfur in the crystal lattice, because pyrite decomposes above 743°C. Alternatively, further research regarding this topic would be of interest if a lower gradient is chosen, maybe at 740° – 690°C. Due to the formation kinetics (Ch. 4.3) of pyrite synthesis by condensation after sublimation, this should take much longer.

Chapter 6

Summary and Conclusion

The removal of the highly radio-toxicologically relevant element selenium by incorporation into mackinawite as important precursor and pyrite as most common near-surface iron sulfide was examined in this study. Two different experimental setups in total were developed to point out how and in which oxidation state Se^{4+} and Se^{2-} become incorporated into pyrite and mackinawite under defined anoxic and acidic conditions at 25°C and 1 bar pressure in a glovebox (1) from aqueous solution in batch-experiments by spontaneous precipitation, simulating mineral nucleation, (2) in a mixed-flow reactor simulating groundwater flow and crystal growth. Thermodynamic calculations were carried out to support the experimental results and offer a comprehensive insight into the initially dissolved species present in solution and show the predominant phases of the Fe-S-Se system over the considered pH-Eh-range. Additionally, (3) a high-temperature synthesis of selenium doted pyrite by condensation from the gaseous phase was achieved by chemical vapor transport.

In conclusion, the spontaneous precipitation and crystal growth experiments have in common that no measurable other phase precipitated during the syntheses of pure Se doted pyrite or

mackinawite. The selenium within these grains is heterogeneously distributed with a higher concentration in the center of the solid. The probable reason for this is the decreasing selenium to sulfur ratio with time. The reason for this observation is the continuous dissolution of S^0 which precipitated initially shortly after mixing due to the oxidation of S^{2-} by the reaction with (and reduction of) Fe^{3+}.

Thus, selenium is effectively immobilized in an anoxic environment as long as iron sulfides are present. The uptake of selenium by pyrite and mackinawite is remarkably high with an average of 98% of the initial Se concentration of 10^{-3} to 10^{-6} mol/L. This demonstrates the high affinity of selenium with different valence states to iron sulfides. There was no significant difference in the uptake of selenium with respect to the initial solution composition nor to the hydrochemical composition, which was adjusted to acidic conditions up to neutral conditions at pH-values of 3.5 – 7 and Eh-values between -200 – 100 mV.

The structural investigations of incorporated selenium in mackinawite and pyrite with selenite initially present in the solution showed the same results in form of a reduction of Se^{4+} to Se^0 for the instantaneous precipitation and crystal growth-experiments. This is in accordance with the thermodynamical calculations which predicted the precipitation of pyrite and elemental selenium. The most likely reason for the Se^{4+}-reduction is their reaction with oxidizing dissolved sulfur species, mainly H_2S and HS^-.

The identification of the crystal structure of Se doted mackinawite using dissolved Se^{2-} for the instantaneous precipitation experiment shows a substitution of S^{2-} by Se^{2-} in a mackinawite-like environment. On the contrary, the thermodynamic calculations predict the precipitation of elemental selenium under these conditions. Since Se^0 is the most stable phase, kinetically reasons are assumed to lead the observed structural substitution.

There are clear differences between the instantaneous precipitation and crystal growth experiments which were carried out in aqueous solution with regard to the crystal structure of incorporated selenide. After an instantaneous precipitation of mackinawite as pyrite precursor phase in instantaneous precipitation experiments, a substitution of S^- by Se^- in selenide doted pyrite was detected, leading to a slightly disturbed pyrite crystal structure. On

the contrary, for lower Fe-S-Se-concentrations and in case of a slower precipitation of selenium doted pyrite in mixed-flow reactor experiments, Se^{2-} retention by incorporation is mainly coupled with a change in the oxidation state and selenium is incorporated as Se^0 into pyrite without structural bonding. Thermodynamic calculations show that Se^0 is expected to be the most stable selenium phase. The results indicate that the substitution of sulfur by selenium in pyrite is kinetically controlled. For acidic and anoxic conditions, this is only possible for highly supersaturated solutions, accompanied with a direct precipitation of the initial metastable mackinawite phase directly after mixing of the separated Fe, S, and Se solutions. It is noteworthy that selenium does not oxidize to Se^0 during the dissolution of mackinawite and the re-precipitation to pyrite, because, in analogy to the natural pyrite formation, it is likely that selenide is bound as aqueous $Fe(HSe)_2$ cluster during the recrystallization process.

The overall predominant species and phases have been determined by calculated stability diagrams for the solution which has been used in crystal growth experiments, showing the total overlap of pyrite and Se^0 stability fields. But even if elemental selenium is incorporated into pyrite, it is promising with respect to the retention of selenium since Se^0 is highly stable because of its low solubility product.

Finally, the synthesis by condensation from the gaseous phase led to pure selenium doted pyrite single crystals. Selenium is homogeneously distributed within the grains which have a mean diameter of 5 mm. With respect to the valence state of incorporated selenium, just zero-valent selenium could be detected without further structural bonding to the pyrite crystal structure. This may be the reason for the low amount of incorporated selenium with a distribution ratio of 0.09 compared to the initial ratio of the reactants. Obviously, only gaseous sulfur and not gaseous selenium reacts with iron. It is likely that the high boiling point of Se^0 (685°C) leads to a condensation of selenium before a reaction with iron can occur.

The conclusion of this study is that pyrite, which is widespread in anoxic aquatic sediments and part of the host rocks of some high-level waste repositories and its precursor

mackinawite, are probably important minerals regarding the decontamination of selenium. The capacity for the incorporation of selenium is extraordinarily high. As well, selenium in its different oxidation states shows a high affinity to iron sulfides. Finally, this can lead to the reduction of the Se-mobility of ^{79}Se from a HLW-disposal site into the biosphere.

The ^{79}Se radioisotope is predominantly available as Se^{4+} within the vitrified glasses which capture the HLW. The structural analyses point out that during the precipitation of pyrite and mackinawite selenite reacts with sulfide which leads to the reduction into the highly insoluble Se^0. Additionally, this lowers the Se-mobility drastically.

The determination of the crystal structure has shown that Se^{2-} can be bound as Se^0 or as a FeS_xSe_y-compound, and that a substitution of S by Se is generally possible, depending on kinetics. In either case, the dissolved selenide does precipitate, which lowers the Se-mobility too. Further investigations should be done to analyze, if there are differences regarding the stabilities of Se^0 being incorporated into pyrite as crystal defect or as FeS_xSe_y accompanied with a structural bonding of Se into the pyrite-like structure.

With respect to the hydrochemical conditions of pyrite formation, elemental selenium is the thermodynamical most stable species. This shows that the scientific common point of view with respect to the similarity of the chemical behavior of sulfur and selenium is an oversimplification, because it depends highly on the oxidation state. There are differences, for example of the stability fields of S^0 and Se^0. The stability of elemental sulfur is restricted to a comparatively small field under acidic and oxic conditions, while the stability field of elemental selenium is much broader and does cover acidic up to alkaline as well as oxic and anoxic conditions.

Chapter 7

Acknowledgement

First of all, I am very grateful for the last four years and I would like to thank the whole staff of the Institute of Mineralogy and Geochemistry (IMG) at the Karlsruhe Institute of Technology (KIT). Because of the amiable atmosphere there I enjoyed my time since the first day.

I especially want to thank my PhD supervisor Professor Thomas Neumann for the productive teamwork as well as for giving me the opportunity to work self-consistent on my scientific work. I am glad for the support with respect to the publications and my presentations for conferences and meetings. Furthermore, I want to acknowledge him for encouraging me when my syntheses were struggling without successes for many months and I am grateful for the experience he made possible to me.

I sincerely thank PD Dr. Thorsten Stumpf of the Institute of Nuclear Waste Disposal (INE) of the Karlsruhe Institute of Technology who was so kindly to agree to be second reviewer of this thesis. Also thanks for giving me the opportunity to measure twice samples at the XPS.

Special thanks go to Elisabeth Eiche for thoroughly cross-reading of my thesis and also huge thanks for measuring my CVT-sample at the SUL-beamline.

Special thanks go also to Claudia Mössner and Cornelia Haug for the measurements at the ICP-MS and ICP-OES, respectively and to Utz Kramar for the support at the ED-XRF.

A special acknowledge goes to Ralf Köppe of the Institute of Anorganic Chemistry (KIT) for his great support during the chemical vapor transport experiments. It was a great experience to learn the CVT-technique I did not want to have missed.

I acknowledge the provision of beamtime by ANKA at KIT and I would like to thank Kathy Dardenne, Tonja Vítovà, and Jörg Rothe for assistance in using the INE beamline. I am also grateful to David Batchelor for his comprehensive help while working at the XAS beamline. Furthermore, I want to thank Peter Weidler of IFG (KIT) for kindly providing me the BET measurements.

I want to acknowledge Mohammad Fotouhi Ardakani, Erich Müller, Peter Pfundstein and especially Volker Zibat of the Laboratory of Electron Microscopy at KIT for the useful comments and the providing of SEM, TEM, and FIB measurements.

Special thanks go to Nicolas Finck of INE (KIT), who introduced me into the interpretation of XAFS-spectra. It was always a pleasure for me to discuss our scientific work.

Also thanks to Dieter Schild of INE (KIT), for the measurements at the XPS.

It was a huge pleasure for me and I am very grateful that I got to know following nice people who stay(ed) at the IMG: Harald Neidhart, Peter Illner, Jan Stelling, Jennifer Blume, Nina Jasmin Schleicher, Maren Hochschild, Alexandra Nothstein, Xiaohui Tang, Hilal Farooq, Agniezska Bankowska, Andreas Holbach and Monika Stelling.

This work was supported by the Helmholtz Association funding the “Virtual Institute of Advanced RadioGeochemistry”. I want to thank for the financial support and the participants of the Virtual Institute for their support and the interesting discussions.

References

Abraitis, P., Pattrick, R., Vaughan, D.: Variations in the compositional, textural and electrical properties of natural pyrite: a review. *Int. J. of Min. Process*. **74**, 41 (2004).

Agüero, A., Pinedo, P., Simon, I., Cancio, D., Moraleda, M., Trueba, C., Perez-Sanchez, D.: Application of the Spanish methodological approach for biosphere assessment to a generic high-level waste disposal site. *Sci. Total Environ.* **403**, 34 (2008).

ANKA: ANKA Instrumentation Book. Wesolowski, P. (Ed.). ANKA Angströmquelle Karlsruhe, ISS, Institute for Synchrotron Radiation, 223 pp. (2010).

Arakaki, T, Morse, J.: Coprecipitation and adsorption of Mn(II) with mackinawite (FeS) under conditions similar to those found in anoxic sediments. *Geochim. Cosmochim. Acta* **57**, 9 (1993).

Ashworth, D.J., Moore, J. Shaw, G.: Effects of soil type, moisture content, redox potential and methyl bromide fumigation on K_d values of radio-selenium in soil. *J. Environ. Radioact.* **99**, 1136 (2008).

Ball, J. & Nordstrom, D.K.: User´s manual for WATEQ4F, with revised thermodynamic data base and test cases for calculating speciation of major, trace, and redox elements in natural waters. U.S. Geological Survey, open-file report (2001).

Behrens, P.: X-ray Absorption Spectroscopy in Chemistry. Part I: EXAFS. *Trends Anal. Chem.* **11**, 218 (1992).

Benning, L.G., Wilkin, R.T., Barnes, H.L.: Reaction pathways in the Fe-S system below 100℃. *Chem. Geol.* **167**, 25 (2000).

Berner, R.A.: Sedimentary pyrite formation: An update. *Geochim. Cosmochim. Acta* **48**, 605 (1984).

BGR: Endlagerung radioaktiver Abfälle in Deutschland. Untersuchung und Bewertung von Regionen mit potenziell geeigneten Wirtsgesteinsformationen. Bundesamt für Geowissenschaften und Rohstoffe. 17 pp. (2007). Electronic ressource: http://www.bgr.bund.de/DE/Themen/Endlagerung/Downloads/BGR_wirtsgest_dtl.html

Bienvenu, P., Cassette, P., Andreoletti, G., Be, M.M., Comte, J., Lepy, M.C.: A new determination of Se-79 half-life. *Appl. Radiat. Isot.* **65**, 355 (2007).

Bildstein, O., Trotignon, L., Perronnet, M., Jullien, M.: Modelling iron-clay interactions in deep geological disposal conditions. *Phys. Chem. Earth* **31**, 618 (2006).

Bingham, P., Connelly, A., Cassingham, N., Hyatt, N.: Oxidation state and local environment of selenium in alkali borosilicate glasses for radioactive waste immobilization. *J. Non-Cryst. Sol.* **357**, 2726 (2011).

Binnewies, M.: Massenspektrometrische Untersuchungen der Systeme $FeCl_2/AlCl_3$ und $FeCl_2/FeCl_3$. *Z. Anorg. Allg. Chem.* **437**, 19 (1977).

Binnewies, M., Milke, E.: Thermochemical Data of Elements and Compounds. 2nd Ed, Wiley, VCH, Weinheim, 928 pp. (2002).

Binnewies, M., Glaum, R., Schmidt, M., Schmidt, P.: Chemische Transportreaktionen. De Gruyter, Berlin, 654 pp. (2011).

Blenk, O., Bucher, E., Willeke, G.: P-type conduction in pyrite single-crystals prepared by chemical vapor transport. *Appl. Phys. Lett.* **62**, 2093 (1993).

Bouchard, R. The preparation of single crystals of FeS_2, CoS_2, and NiS_2 pyrites by chlorine transport. *J. Cryst. Growth* **2**, 40 (1968).

Bourdoiseau, J, Jeannin, M., Sabot, R., Rémazeilles, C, Refait, P.: Characterization of mackinawite by Raman spectroscopy: Effects of crystallization, drying and oxidation. *Corr. Sci.* **50**, 3247 (2008).

Breynaert, E., Bruggeman, C., Maes, A.: XANES-EXAFS analysis of se solid-phase reaction products formed upon contacting Se(IV) with FeS_2 and FeS. *Environ. Sci. & Tech.* **42**, 3595 (2008).

Bruggeman, C., Maes, A., Vancluysen, J., Vandemussele, P.: Selenite reduction in Boom clay: Effect of FeS_2, clay minerals and dissolved organic matter. *Env. Pol.* **137**, 209 (2005).

Bruno, J., Bosbach, D., Kulik, D., Navrotsky, A.: Chemical thermodynamics of solid solutions of interest in nuclear waste management. Chemical Thermodynamics Series No. 10, OECD/NEA, 244 pp. (2007).

Butler, I.B., Rickard, D.: Framboidal pyrite formation via the oxidation of iron (II) monosulfide by hydrogen sulphide. *Geochim Cosmochim. Acta* **64**, 2665 (2000).

Charlet, L., Scheinost, A.C., Tournassat, C., Greneche, J.M., Gehin, A., Fernandez-Martinez, A., Coudert, S., Tisserand, D., Brendle, J.: Electron transfer at the mineral/water interface: Selenium reduction by ferrous iron sorbed on clay. *Geochim Cosmochim. Acta* **71**, 5731 (2007).

Corkum, A., Martin, C.: The mechanical behaviour of weak mudstone (Opalinus Clay) at low stresses. *Inter. J. of Rock Mech. and Min. Sci.* **44**, 196 (2007).

De Canniére, P., Maes, A., Williams, S., Bruggeman, C., Beauwens, T., Maes, N., Cowper, M.: Behaviour of selenium in Boom Clay. External Report of the Belgian Nuclear Research Centre. Electronic resource: http://publications.sckcen.be/dspace/ (2010).

De Craen, M., Van Geet, M., Wang, L., Put, M.: High sulphate concentrations in squeezed Boom Clay pore water: evidence of oxidation of clay cores. *Phys. Chem. Earth* **29**, 91 (2004).

Demoisson, F., Mullet, M., Humbert, B.: Pyrite oxidation in acidic medium: overall reaction pathway. *Surf. Interface Anal.* **40**, 343 (2008).

Diener, A., Neumann, T.: Synthesis and incorporation of selenide in pyrite and mackinawite. *Radiochim. Acta* **99**, 791-798 (2011).

Diener, A., Neumann, T., Kramar, U., Schild, D.: Structure of selenium incorporated in pyrite and mackinawite as determined by XAFS analyses. *J. Contam. Hydr.* **133**, 30 (2012).

Diener, A., Köppe, R.: Synthesis of selenium doted pyrite single crystals prepared by chemical vapor transport. J. Cryst. Growth, in press (2012).

Drobner, E., Huber, H., Wächtershäuser, G., Rose, D., Stetter, K.: Pyrite formation linked with hydrogen evolution under anaerobic evolution. *Nature* **346**, 742 (1990).

Dove, M.: Structure and dynamics – an atomic view of materials. Oxford University Press, Oxford, 334 pp. (2003).

Engberg, R., Westcot, D.W., Delamore, M., Holz, D.: Federal and state perspectives on regulation and remediation of irrigation-induced selenium problems. In: Frankenberger Jr., W.T., Engberg, R.A. (Eds.), *Environmental chemistry of selenium.* Marcel-Dekker Inc., New York, 1-25 (1998).

Etzel, K.: Biological and abiotic dissolution of natural, cut and synthetic pyrite surfaces. PhD-Thesis. Christian-Albrechts-University Kiel (2008).

Farrand, M.: Framboidal pyrites precipitated synthetically. *Mineral. Deposita* **5**, 237 (1970).

Faure, G.: Principles and applications of geochemistry. 2nd Ed, Prentice Hall, 625 pp. (1998).

Fiechter, S., Mai, J., Ennaoui, A., Szacki, W.: Chemical vapour transport of pyrite (FeS_2) with halogen (Cl, Br, I). *J. Cryst. Growth* **78**, 438 (1986).

Fleet, M.: Phase equilibria at high temperatures. In: Vaughan, D. (Ed.): Sulfide mineralogy and geochemistry. *Rev. Min. & Geochem.* **61**, 365 (2006).

Gaidon, J.L., Martincalle, S., Boudeulle, M.: Pyrite from concretion pipes in mesozoic shales - mineralogical and chemical evidence of hydrothermal origin. *Mar. Geol.* **84,** 239 (1988).

Gaucher, E., Robelin, C., Matray, J.M., Negral, G., Gros, Y., Heitz, J.F., Vinsot, A., Rebours, H., Cassagnabere, A., Bouchet, A.: ANDRA underground research laboratory: interpretation of the mineralogical and geochemical data acquired in the Callovian-Oxfordian formation by investigative drilling. *Phys. and Chem. of the Earth* **29**, 55 (2004).

Geckeis, H., Rabung, T.: Actinide geochemistry: From the molecular level to the real system. *J. Contam. Hydr.* **102**, 187 (2008).

Giggenbach, W.: Optical spectra and equilibrium distribution of polysulfide ions in equilibrium solution at 20°. *Inorg. Chem.* **11**, 1201 (1972).

Grambow, B.: Mobile fission and activation products in nuclear waste disposal. *J. Contam. Hydr.* **102**, 180 (2008).

Griffin, W.L., Ashley, P.M., Ryan, C., Sie, S., Suter, G.: Pyrite Geochemistry in the north arm epithermal Ag-Au deposit, Queensland, Australia: A proton-microprobe study. *Can. Min.* **29**, 185 (1991).

Hamilton, S.J.: Review of selenium toxicity in the aquatic food chain. *Sci. Total Environ.* **326**, 1 (2004).

He, Q., Yao, K.: Microbial reduction of selenium oxyanions by Anaeromyxobacter dehalogenans. *Biores. Tech.* **101**, 3760 (2010).

Heberling, F.: Structural incorporation of Neptunyl(V) into Calcite. PhD-thesis, Karlsruher Institut für Technologie (2010).

Hillebrand, U.: Stöchiometrie. 2nd Ed., Springer, Berlin, Heidelberg, 409 pp. (2009).

Hotje, U, Rose, C., Binnewies, M.: Beschreibung des Chemischen Transports im System ZnS/ZnSe. *Z. Anorg. Allg. Chem.* **631**, 2501 (2005).

Howard, J.H.: Geochemistry of selenium: formation of ferroselite and selenium behavior in the vicinity of oxidizing sulfide and uranium deposits. *Geochim. Cosmochim. Acta* **41**, 1665 (1977).

Jiang, S., He, M., Diao, L., Li, C., Gou, J., Wu, S.: Re-measurement of the half-life of 79Se. *Phys. Res.* **489**, 195 (2002).

Jörg, G., Bühnemann, R., Hollas, S., Kivel, N., Kossert, K., Van Winckel, S., von Gostomski, C.: Preparation of radiochemically pure 79Se and highly precise determination of its half-life. *Appl. Rad. Isotop.* **68**, 2339 (2010).

Joseph, C., Schmeide, K., Sachs, S., Brendler, V., Geipel, G., Bernhard, G.: Sorption of uranium(VI) onto Opalinus Clay in the absence and presence of humic acid in Opalinus Clay pore water. *Chem. Geol.* **284**, 240 (2011).

Kelly, S.: Basics of EXAFS data analysis. Electronic resource (2009) available under: http://www.xafs.org/Tutorials?action=AttachFile&do=view&target=Basics_of_XAFS_analysis_2009.pdf

Kishchak, I.: Supplementation of selenium in the diets of domestic animals. In: Frankenberger Jr., W.T., Engberg, R.A. (Eds.), *Environmental chemistry of selenium.* Marcel-Dekker Inc., New York, 143-151 (1998).

Kim, J., Gompper, K., Geckeis, H.: Forschung zur Langzeitsicherheit der Endlagerung hochaktiver Abfälle. In: Forschungszentrum Karlsruhe GmbH, Stabsabteilung Öffentlichkeitsarbeit (Ed.): Radioaktivität und Kernenergie. 2nd edition, 117 – 130 pp. (2001).

Lacour, M., Zunder, T., Restle, A., Schwarzer, G.: No evidence for an impact of selenium supplementation on environment associated health disorders – a systematic review. *Int. J. Hyg. Environ. Health* **207**, 1 (2004).

Lehner, S., Savage, K.: The effect of As, Co, and Ni impurities on pyrite oxidation kinetics: Batch and flow-through reactor experiments with synthetic pyrite. *Geochim. Cosmochim. Acta* **72**, 1788 (2008).

Lennie, A., Redfern, S., Schofield, P., Vaughan, D.: Synthesis and Riedveld crystal structure refinement of mackinawite, tetragonal FeS. *Min. Mag.* **59**, 677 (1995).

Lennie, A., Redfern, S., Champness, P., Stoddart, C., Schofield, P., Vaughan, D.; Transformation of mackinawite to greigite: An in-situ X-ray powder diffraction and transmission electron microscope study. *Amer. Min.* **82**, 302 (1997).

Lenz, M. & Lens, P.: The essential toxin: The changing perception of selenium in environmental sciences. *Sci. Total Environ.* **407**, 3620 (2009).

Li, S., Xiao, T., Zheng, B.: Medical geology of arsenic, selenium and thallium in China. *Sci.Total Env.* **421**, 31 (2011).

Lingane, J.: Controlled potential electroanalysis. *Anal. Chim Acta* **2**, 584 (1948).

Liu, X., Fattahi, M., Montavon, G., Grambow, B.: Selenide retention onto pyrite under reducing conditions. *Radiochim. Acta* **96**, 473 (2008).

Luther III., G.W.: Pyrite synthesis via polysulfide compounds. *Geochim Cosmochim. Acta* **55**, 2839 (1991).

Makovicky, E.: Crystal structures of sulfides and other chalcogenides. In: Vaughan, D. (Ed.): Sulfide mineralogy and geochemistry. *Rev. Min. & Geochem.* **61**, 7 (2006).

Malekifarsani, A., Skachek, M.A.: Effect of precipitation, sorption and stable of isotope on maximum release rates of radionuclides from engineered barrier system (EBS) in deep repository. *J. Environm. Radioact.* **100**, 807 (2009).

Mallants, D., Marivoet, J., Sillen, X.: Performance assessment of the disposal of vitrified high-level waste in a clay layer. *J. Nucl. Mat.* **298**, 125 (2001).

Manceau, A., Matthew, A.M., Nobumichi, T.: Quantitative Speciation of Heavy Metals in Soils and Sediments by Synchrotron X-ray Techniques. *Rev. Mineral. Geochem.* 49, 341 (2002).

Masscheleyn, P.H., Delaune, R.D., Patrick Jr., W.H.: Transformations of selenium as affected by sediment oxidation-reduction potential and pH. *Environ. Sci. Technol.* **24**, 91 (1990).

Mayland, H., James, L., Panter, K., Sonderegger, J.: Selenium in seleniferous environments. *SSSA Special Publication* **23**, 15 (1989).

Merkel, B., Planer-Friedrich, B.: Grundwasserchemie. Praxisorientierter Leitfaden zur numerischen Modellierung von Beschaffenheit, Kontamination und Sanierung aquatischer Systeme. 2. Auflage, Springer Verlag, Berlin Heidelberg (2008).

Morse, J. W. & Cornwell, J. C.: Analysis and distribution of iron sulfide minerals in recent anoxic marine-sediments. *Mar. Chem.* **22**, 55 (1987).

Morse, J.W., Arakaki, T.: Adsorption and coprecipitation of divalent metals with mackinawite (FeS). *Geochim. Cosmochim. Acta* **57**, 3635 (1993).

Morse, J.W.: Interactions of trace-metals with authigenic sulfide minerals - implications for their bioavailability. *Mar. Chem.* **46**, 1 (1994).

Morse, J.W., Wang, Q.: Pyrite formation under conditions approximating those in anoxic sediments: II. Influence of precursor iron minerals and organic matter. *Mar.Chem.* **57**, 187 (1997).

Morse, J.W., Luther, G.W.: Chemical influences on trace metal-sulfide interactions in anoxic sediments. *Geochim. Cosmochim. Acta* **63**, 3373 (1999).

Moulder, J.F., Stickle, W.F., Sobol, P.E., Bomben, K.D.: Handbook of X-Ray Photoelectron Spectroscopy, Perkin-Elmer Corporation, Physical Electronics Division, Eden Prairie, Minnesota (1992).

Myneni, S.C., Tokunaga, T.K., Brown, G.E.: Abiotic selenium redox transformations in the presence of Fe(II,III) oxides. *Sci. Mag*. 278, 1106 (1997).

Navarro-Alarcon, M. & Cabrera-Vique, C.: Selenium in food and the human body: A review. *Sci. Total Environ.* **400**, 115 (2008).

Naveau, A., Monteil-Rivera, F., Guillon, E., Dumonceau, J.: Interactions of aqueous selenium(-II) and (IV) with metallic sulfide surfaces. *Environ. Sci. & Techn.* **41**, 5376 (2007).

Newville, M.: IFEFFIT: Interactive EXAFS analysis and FEFF fitting. *J. Synchrotron Rad.* **8**., 322 (2001).

Newville, M.: Fundamentals of XAFS. Electronic resource (2004) available under: http://xafs.org/Tutorials?action=AttachFile&do=view&target=Newville_xas_fundamentals.pdf

Oelkers, E.H., Bénézeth, P., Pokrovski, G.S.: Thermodynamic databases for water-rock interaction. In: Oelkers, E. and Schott, J. (Eds.): Thermodynamic and kinetics of water-rock interaction. *Rev. Min. Geochem.* **70**, 6 (2009).

Ohfuji H., Rickard, D.: Experimental syntheses of framboids – a review. *Earth-Sci. Rev.* **71**, 147 (2005).

Olin, Å., Noläng, B., Öhman, L.-O., Osadchii, E. & Rosén, E.: *Chemical Thermodynamics of Selenium*, 1st ed., Elsevier, Amsterdam 2005, 894 (2005).

Orberger, B., Pasava, J., Gallien, J., Daudin, L., Trocellier, P.: Se, As, Mo, Ag, Cd, In, Sb, Pt, Au, Tl, Re traces in biogenic and abiogenic sulfides from Black Shales (Selwyn Basin, Yukon territories, Canada): A nuclear microprobe study. *NIM B* **210**, 441 (2003).

O´Toole, D., Raisbeck, M.: Magic numbers, elusive lesions: comparative pathology and toxicology of selenosis in waterfowl and mammalian species. In: Frankenberger Jr., W.T., Engberg, R.A. (Eds.), *Environmental chemistry of selenium.* Marcel-Dekker Inc., New York, 355-395 (1998).

Parkhurst, D.L. and Appelo, C.A.J.: User's guide to PHREEQC. A computer program for speciation, batch-reaction, one-dimensional transport, and inverse geochemical calculations. U.S. Geological Survey Water-Resources Investigations Report **99**, 312 pp. (1999).

Plieth, W.: Electrochemistry for materials science. 1st Ed., Elsevier, Amsterdam, 410 pp. (2008).

Presser, T, Swain, W.: Geochemical evidence for Se mobilization by the weathering of pyritic shale, San Joaquin Valley, California, U.S.A. *Appl. Geochem*. **5**, 703 (1990).

Prieto, M.: Thermodynamics in solid solution-aqueous solution systems. In: Oelkers, E. and Schott, J. (Eds.): Thermodynamic and kinetics of water-rock interaction. *Rev. Min. Geochem.* **70**, 6 (2009).

Ravel, B.: ATHENA User's Guide. Document version 1.5 for athena version 0.8.56. http://cars9.uchicago.edu/~ravel/software/doc/Athena/html/athena.pdf (2009).

Reed, M., Palandri, J.: Sulfide mineral precipitation from hydrothermal fluids. In: Vaughan, D. (Ed.): Sulfide mineralogy and geochemistry. *Rev. Min. & Geochem.* **61**, 7 (2006).

Rickard, D.: Kinetics and mechanism of pyrite formation at low temperatures. *Amer. J. Sci.* **275**, 636 (1975).

Rickard, D., Morse, J.: Acid volatile sulfide (AVS). *Mar. Chem.* **97**, 141 (2005).

Rickard, D., Luther III., G.: Metal sulfide complexes and clusters. In: Vaughan, D. (Ed.): Sulfide mineralogy and geochemistry. *Rev. Min. & Geochem*. **61**, 7 (2006).

Rickard, D., Luther III., G.: Chemistry of iron sulfides. *Chem. Rev.* **107**, 514 (2007).

Rieder, M., Crelling, J., Sustai, O., Drabek, M., Weiss, Z., Klementova, M.: Arsenic in iron disulfides in a brown coal from the North Bohemian Basin. *Int. J. Coal Geol.* **71**, 115 (2007).

Roberts, W., Walker, A., Buchanan, A.: Chemistry of pyrite formation in aqueous solution and its relation to the depositional environments. *Miner. Deposita* **4**, 18 (1969).

Rothe, J., Léon, A.: X-ray absorption fine structure (XAFS) spectroscopy. In: Léon, A. (Ed.): Hydrogen technology – mobile and portable applications. Springer, Berlin, 602-622 (2008).

Rouxel, O., Fouquet, Y., Ludden, J.N.: Subsurface processes at the Lucky Strike hydrothermal field, Mid-Atlantic Ridge: Evidence from sulfur, selenium, and iron isotopes. *Geochim. Cosmochim. Acta* **68**, 2295 (2004).

Ryser, A.L., Strawn, D.G., Marcus, M.A., Johnson-Maynard, J.L., Gunter, M.E., Moller, G.: Micro-spectroscopic investigation of selenium-bearing minerals from the Western US Phosphate Resource Area. *Geochem. Transact.* **6**, 1 (2005).

Scheinost, A.C., Kirsch, R., Banerjee, D., Fernandez-Martinez, A., Zaenker, H., Funke, H., Charlet, L.: X-ray absorption and photoelectron spectroscopy investigation of selenite reduction by Fe-II-bearing minerals. *J. Contam. Hydr.* **102**, 228 (2008a).

Scheinost, A.C., Charlet, L.: Selenite reduction by mackinawite, magnetite and siderite: XAS characterization of nanosized redox products. *Environ. Sci. Technol.* **42**, 1984 (2008b).

Schoonen, M.A.A., Barnes, H.L.: Reactions forming pyrite and marcasite from solution: II. Via FeS precurser below 100℃. *Geochim. Cosmochim. Acta* **55**, 1505 (1991).

Schrauzer, G.N.: Selenium. In: Elements and their compounds in the environment. 2nd Ed., Wiley-VCH, Weinheim, pp.1365-1406 (2004).

Seah, M.P., Gilmore, I.S., G. Beamson: XPS: Binding energy calibration of electron spectrometers 5 - a reassessment of the reference energies. *Surf. Interface Anal.* **26**, 642 (1998).

Séby, F., Potin-Gautier, M., Giffaut, E., Donard, O.F.X.: Assessing the speciation and the biogeochemical processes affecting the mobility of selenium from a geological repository of radioactive wastes to the biosphere. *Analusis* **26**, 193 (1998).

Séby, F., Potin-Gautier, M., Giffaut, E., Borge, G., Donard, O.: A critical review of thermodynamic data for selenium species at 25℃. *Chem. Geol.* **171**, 173 (2001).

Shaw, G., Ashworth, D.: Selenium: Radionuclides, in: *Encyclopedia of Inorganic Chemistry*, John Wiley & Sons, London (2010).

Takasu, A., Naito, M., Umeki, H., Masuda, S.: Application of supplementary safety indicators for H12 performance assessment. *Sci. Basis Nucl. Waste Manag.* **663**, 907 (2000).

Terry, N., Zayed, A.: Phytoremediation of selenium. In: Frankenberger Jr., W.T., Engberg, R.A. (Eds.), *Environmental chemistry of selenium.* Marcel-Dekker Inc., New York, 633 (1998).

Tinggi, U.: Selenium: its role as antioxidant in human health. *Env. Health Prev. Med.* **13**, 102 (2008).

Tokunaga, T.K., Sutton, S.R., Bajt, S., Nuessle, P., Shea-McCarthy, G.: Selenium diffusion and reduction at the water-sediment boundary: Micro-XANES spectroscopy of reactive transport. *Environm. Sci. & Techn.* **32**, 1092 (1998).

Tomm, Y., Schieck, R., Ellmer, K., Fiechter, S.: Growth-mechanism and electronic-properties of doped pyrite (FeS_2) crystals. *J. Cryst. Growth* **146**, 271 (1995).

Umeki, H.: Key aspects of the H12 safety case. *Sci. Basis Nucl. Waste Manag.* **663**, 701 (2000).

Velinsky, D.J., Cutter, G.A.: Determination of elemental selenium and pyrite-selenium in sediments. *Anal. Chim. Acta* **235**, 419 (1990).

Wang, Q.W., Morse, J.W: Pyrite formation under conditions approximating those in anoxic sediments. 1. Pathway and morphology. *Mar.Chem.* **52**, 99 (1996).

Wei, D.W., Osseo-Asare, K.: Particulate pyrite formation by the Fe3+/HS- reaction in aqueous solutions: effect of solution composition. *Colloids and Surfaces A: physicochemical and engineering aspects* **118**, 51 (1996).

Wei, D.W., Osseo-Asare, K.: Aqueous synthesis of finely divided pyrite particles. *Colloids and Surfaces A: physicochemical and engineering aspects* **121**, 27 (1997).

WHO: Guidelines for drinking-water quality. World Health Organisation, Geneva, 515 pp (2004).

WHO: Selenium in Drinking-water. Background document for development of WHO guidelines for drinking-water Quality. World Health Organisation, 22 pp. (2011). Electronic resource: http://www.who.int/water_sanitation_health/dwq/chemicals/selenium.pdf.

Willeke, G., Blenk, O., Kloc, C., Bucher, E.: Preparation and electrical transport of pyrite (FeS_2) single crystals. *J. Alloys Compounds* **178**, 181 (1992).

Wincott, P., Vaughan, D.: Spectroscopic studies of sulfides. In: Vaughan, D. (Ed.): Sulfide mineralogy and geochemistry. *Rev. Min. & Geochem.* **61**, 7 (2006).

Wolthers, M.: Geochemistry and environmental mineralogy of the iron–sulphur–arsenic system. PhD-Thesis, Universiteit Utrecht (2003).

Wu, L.: Review of 15 years of research on ecotoxicology and remediation of land contaminated by agricultural drainage sediment rich in selenium. *Ecotoxicol. Environ. Saf.* **57**, 257 (2004).

Wyckhoff, R.: Crystal structures 1. Interscience publishers, 2nd Ed., New York, 85-237 (1963).

Xiong, Y.L.: Predicted equilibrium constants for solid and aqueous selenium species to 300 degrees C: applications to selenium-rich mineral deposits. *Ore Geol. Rev.* **23,** 259 (2003).

Yakovleva, V., Belogub, E., Novoselov, K.: Supergene iron sulpho-selenides from the Zapadno-Ozernoe copper-zinc massive sulphide deposit, South Urals, Russia: a new solid-solution series between pyrite FeS_2 and dzharkenite $FeSe_2$**.** *Min. Mag.* **67**, 355 (2003).

Yllera de Llano, A., Bidoglio, G., Avogadro, A., Gibson, P.N., Rivas Romero, P.: Redox reactions and transport of selenium through fractured granite. *J. Contam. Hydrol.* 21, 129 (1996).

Zhang, Y.Q., Zahir, Z.A., Frankenberger, W.T.: Factors affecting reduction of selenate to elemental selenium in agricultural drainage water by Enterobacter taylorae. *J. Agricult. Food Chem.* **51**, 7073 (2003).

Zhu, J.M., Zuo, W., Liang, X.B., Li, S. & Zheng, B.: Occurrence of native selenium in Yutangba and its environmental implications. *Appl. Geochem.* **19**, 461 (2004).

Zingaro, R., Dufner, D., Murphy, A., Moody, C.: Reduction of oxoselenium anions by iron(II) hydroxide. *Env. Intern.* **23**, 299 (1997).

Appendix

A) Thermodynamic equilibrium constants

Tab.: Dissolved sulfur phases.

SO_4^{-2}	$SO_4^{-2} \leftrightarrows SO_4^{-2}$	($\log_{10} K = 0.0$)
HSO_4^-	$H^+ + SO_4^{2-} \leftrightarrows HSO_4^-$	($\log_{10} K = 1.988$)
$H_2S_{(aq)}$	$SO_4^{2-} + 10H^+ + 8e^- \leftrightarrows H_2S + 4H_2O$	($\log_{10} K = 40.644$)
$H_2S_{(g)}$	$H_2S \leftrightarrows H_2S$	($\log_{10} K = -0.997$)
HS^-	$H_2S \leftrightarrows HS^- + H^+$	($\log_{10} K = -6.994$)
S^{2-}	$HS^- \leftrightarrows S^{2-} + H^+$	($\log_{10} K = -12.918$)
S_2^{2-}	$HS^- \leftrightarrows S_2^{2-} + H^+$	($\log_{10} K = -14.528$)
S_3^{2-}	$HS^- \leftrightarrows S_3^{2-} + H^+$	($\log_{10} K = -13.282$)
S_4^{2-}	$HS^- \leftrightarrows S_4^{2-} + H^+$	($\log_{10} K = -9.829$)
S_5^{2-}	$HS^- \leftrightarrows S_5^{2-} + H^+$	($\log_{10} K = -9.595$)
S_6^{2-}	$HS^- \leftrightarrows S_6^{2-} + H^+$	($\log_{10} K = -9.881$)

Tab.: Dissolved iron phases.

Fe^{2+}	$Fe^{2+} \leftrightarrows Fe^{2+}$	($\log_{10} K = 0.0$)
Fe^{3+}	$Fe^{2+} \leftrightarrows Fe^{3+} + e^-$	($\log_{10} K = -13.020$)
$FeOH^{2+}$	$Fe^{+3} + H_2O \leftrightarrows FeOH^{2+} + H^+$	($\log_{10} K = -2.19$)
$FeOH^+$	$Fe^{+2} + H_2O \leftrightarrows FeOH^+ + H^+$	($\log_{10} K = -9.5$)
$Fe(OH)_3^-$	$Fe^{+2} + 3H_2O \leftrightarrows Fe(OH)_3^- + 3H^+$	($\log_{10} K = -31.0$)
$Fe(OH)_2^+$	$Fe^{+3} + 2H_2O \leftrightarrows Fe(OH)_2^+ + 2H^+$	($\log_{10} K = -5.67$)
$Fe(OH)_3$	$Fe^{+3} + 3H_2O \leftrightarrows Fe(OH)_3 + 3H^+$	($\log_{10} K = -12.56$)
$Fe(OH)_4$-	$Fe^{+3} + 4H_2O \leftrightarrows Fe(OH)_4^- + 4H^+$	($\log_{10} K = -21.6$)
$Fe_2(OH)_2^{4+}$	$2Fe^{+3} + 2H_2O \leftrightarrows Fe_2(OH)_2^{4+} + 2H^+$	($\log_{10} K = -2.95$)
$Fe_3(OH)_4^{5+}$	$3Fe^{+3} + 4H_2O \leftrightarrows Fe_3(OH)_4^{5+} + 4H^+$	($\log_{10} K = -6.3$)

Tab.: Dissolved iron-sulfur phases.

$FeSO_4$	$Fe^{2+} + SO_4^{2-} \leftrightarrows FeSO_4$	($\log_{10} K = 2.25$)

$Fe(SO_4)_2^-$	$Fe^{3+} + 2SO_4^{2-} \leftrightarrows Fe(SO_4)_2^-$	($\log_{10} K = 5.38$)
$Fe(HS)_2$	$Fe^{2+} + 2HS^- \leftrightarrows Fe(HS)_2$	($\log_{10} K = 8.95$)
$Fe(HS)_3^-$	$Fe^{2+} + 3HS^- \leftrightarrows Fe(HS)_3^-$	($\log_{10} K = 10.987$)

Tab.: Dissolved selenium phases.

HSe^-	$SeO_3^{2-} + 7H^+ + 6e^- \leftrightarrows HSe^- + 3H_2O$	($\log_{10} K = 42.514$)
H_2Se	$HSe^- + H^+ \leftrightarrows H_2Se$	($\log_{10} K = 3.8$)
SeO_4^{2-}	$SeO_4^{2-} \leftrightarrows SeO_4^{2-}$	($\log_{10} K = 0.0$)
SeO_3^{2-}	$SeO_4^{2-} + 2H^+ + 2e^- \leftrightarrows SeO_3^{2-} + H_2O$	($\log_{10} K = 30.256$)
H_2SeO_3	$SeO_3^{2-} + 2H^+ \leftrightarrows H_2SeO_3$	($\log_{10} K = 11.25$)
$HSeO_3^-$	$SeO_3^{2-} + H^+ \leftrightarrows HSeO_3^-$	($\log_{10} K = 8.5$)
$HSeO_4^-$	$SeO_4^{2-} + H^+ \leftrightarrows HSeO_4^-$	($\log_{10} K = 1.66$)

Tab.: Stable phases.

Magnetite	$Fe_3O_4 + 8H^+ \leftrightarrows 2Fe^{3+} + Fe^{2+} + 4H_2O$	($\log_{10} K_{SP} = 3.737$)
Hematite	$Fe_2O_3 + 6H^+ \leftrightarrows 2Fe^{3+} + 3H_2O$	($\log_{10} K_{SP} = -4.008$)
Maghemite	$Fe_2O_3 + 6H^+ \leftrightarrows 2Fe^{3+} + 3H_2O$	($\log_{10} K_{SP} = 6.386$)
Goethite	$FeOOH + 3H^+ \leftrightarrows Fe^{3+} + 2H_2O$	($\log_{10} K_{SP} = -1.0$)
$Fe(OH)_3(a)$	$Fe(OH)_3 + 3H^+ \leftrightarrows Fe^{+3} + 3H_2O$	($\log_{10} K_{SP} = 4.891$)
$Fe_3(OH)_8$	$Fe_3(OH)_8 + 8H^+ \leftrightarrows 2Fe^{3+} + Fe^{2+} + 8H_2O$	($\log_{10} K_{SP} = 20.222$)
Sulfur	$S + 2e^- \leftrightarrows S^{2-}$	($\log_{10} K_{SP} = -15.026$)
Selenium	$Se + H^+ + 2e^- \leftrightarrows HSe^-$	($\log_{10} K_{SP} = -17.322$)
FeS(ppt)	$FeS + H^+ \leftrightarrows Fe^{2+} + HS^-$	($\log_{10} K_{SP} = -3.915$)
Mackinawite	$FeS + H^+ \leftrightarrows Fe^{2+} + HS^-$	($\log_{10} K_{SP} = -4.648$)
Greigite	$Fe_3S_4 + 4H^+ \leftrightarrows 2Fe^{3+} + Fe^{2+} + 4HS^-$	($\log_{10} K_{SP} = -45.035$)
Pyrite	$FeS_2 + 2H^+ + 2e^- \leftrightarrows Fe^{2+} + 2HS^-$	($\log_{10} K_{SP} = -18.479$)
SeO_2	$SeO_2 + H_2O \leftrightarrows SeO_3^{2-} + 2H^+$	($\log_{10} K_{SP} = -8.380$)
Ferroselite	$FeSe_2 + 2H^+ + 2e^- \leftrightarrows Fe^{2+} + 2HSe^-$	($\log_{10} K_{SP} = -18.580$)
$Fe_2(SeO_3)_3$	$Fe_2(SeO_3)_3 \leftrightarrows 2Fe^{3+} + 3SeO_3^{2-}$	($\log_{10} K_{SP} = -35.430$)

B) Selected published XAFS data for comparison

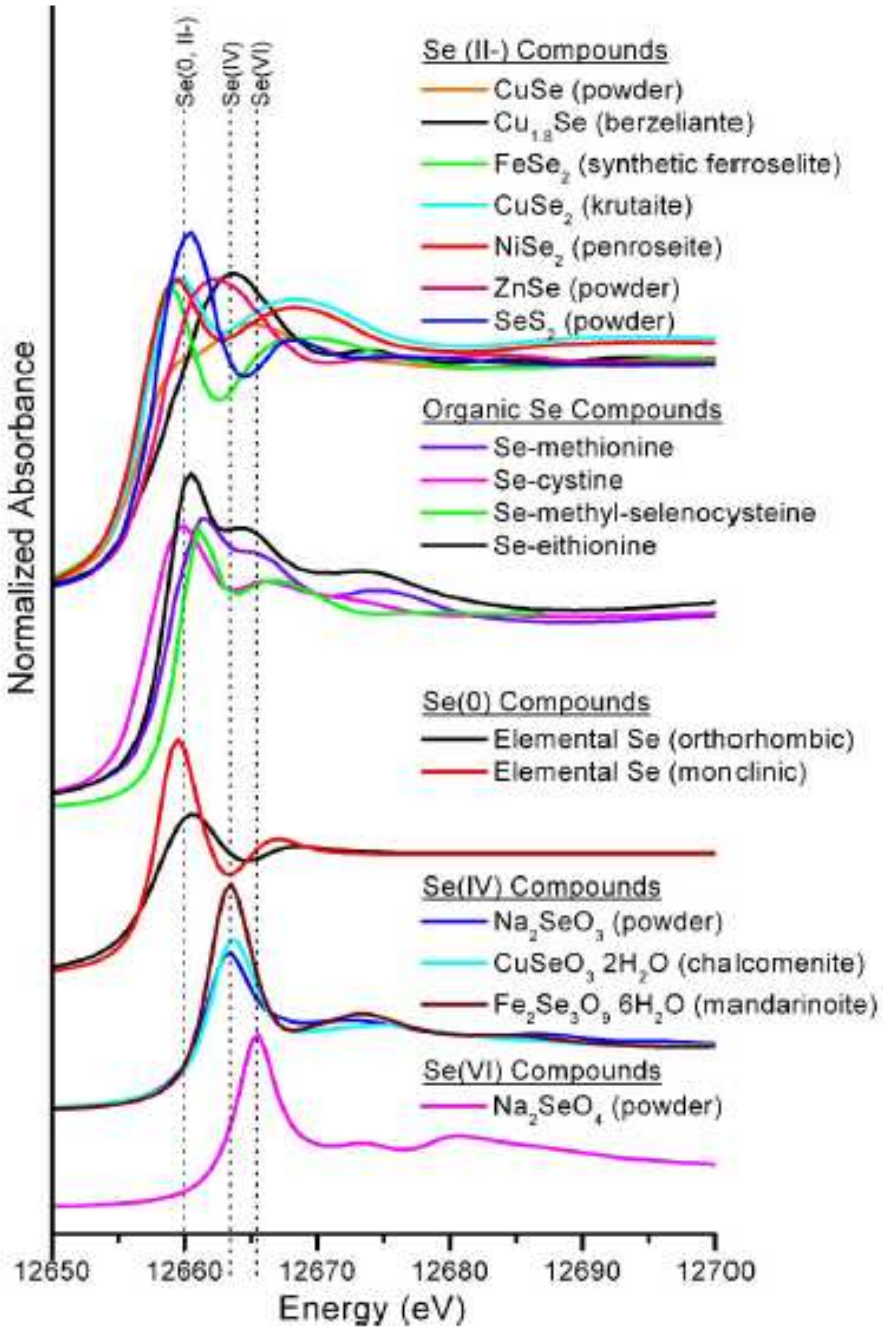

Selenium XANES spectra for reference standards (Ryser et al., 2005).

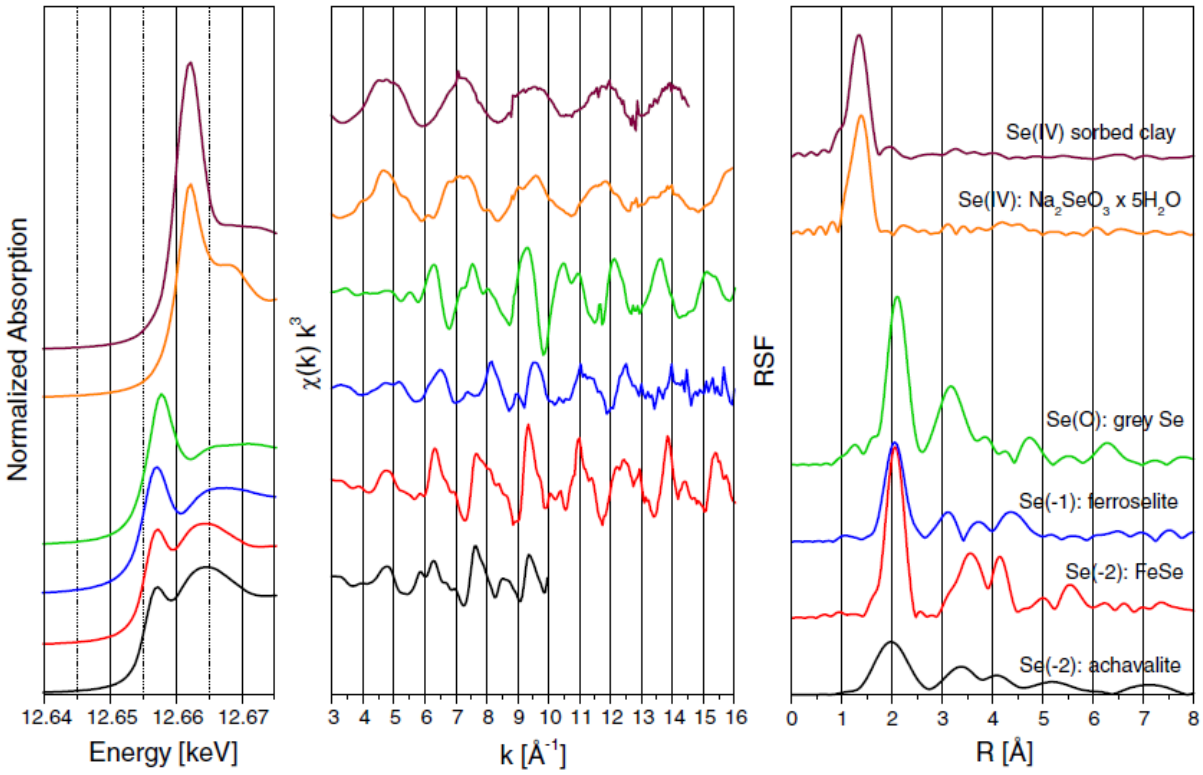

Selenium K-edge XAS spectra of Se(IV) sorbed to synthetic montmorillonite at pH 6.0 in the absence of Fe^{2+}, in comparison to selected references with Se oxidation states of IV, 0, -I and -II (left, XANES; middle, EXAFS; right, Fourier transform of EXAFS) (Charlet et al., 2007).

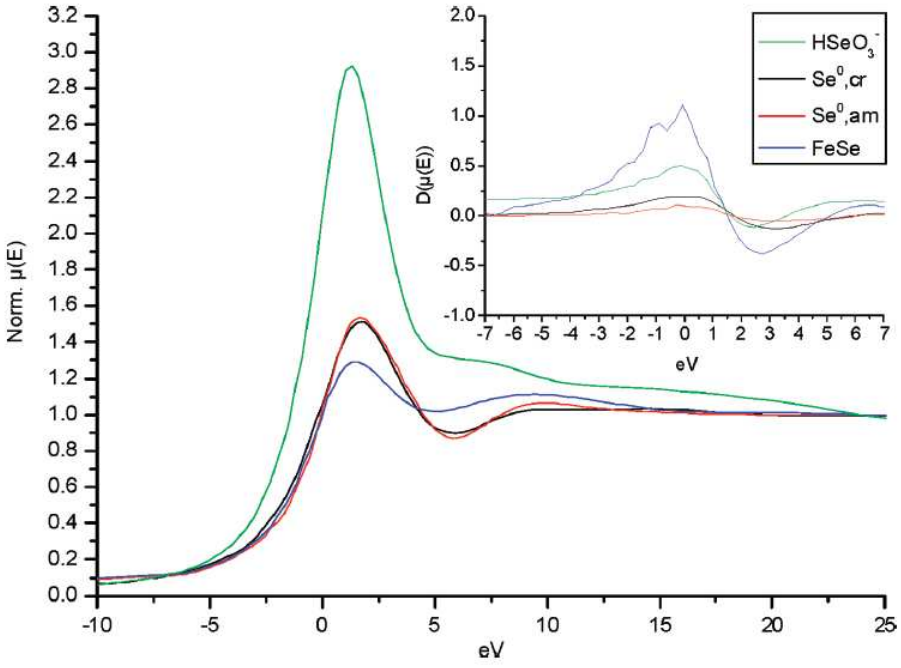

Normalized XANES spectra of different Se standards ($HSeO_3^-$, green; Se^0 amorphous, red; Se^0 crystalline, black; FeSe, blue) (Breynaert et al., 2008).

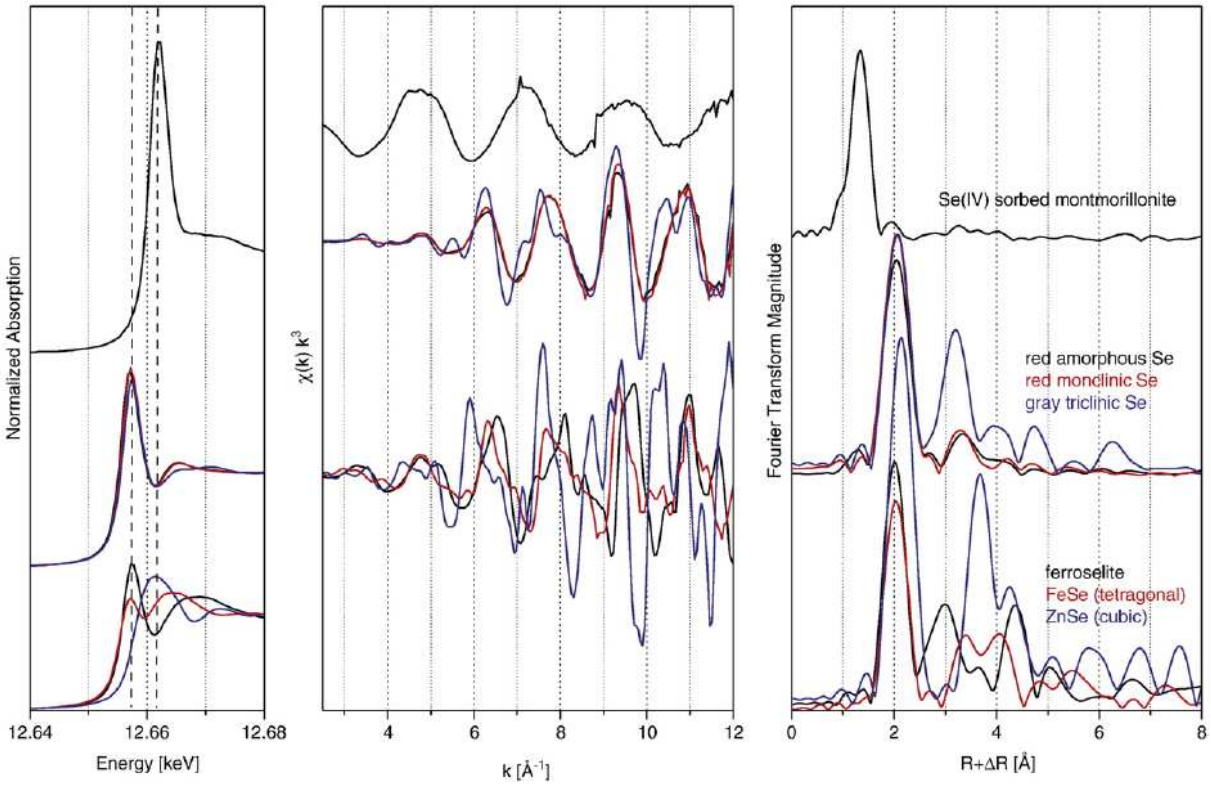

Se K-edge XAFS spectra of references. XANES (left), EXAFS (center) and Fourier transform (right) (Scheinost et al. 2008).